5 Magnetic resonance imaging

5.1 Basic principles

In common with all other imaging processes in medical diagnostics, magnetic resonance tomography makes use of the interaction of anatomical structures within the human body with a radiation field. This interaction, however, should not be so weak that no radiation re-emerges from the object to be measured, nor so strong that the biological tissue is damaged. In the case of electromagnetic waves, the shortwave region (<0.05 nm) has been used in medical diagnostics ever since the discovery of x-rays in 1895; the longwave region (>0.3 nm) has only come to be employed since 1973, in the field of magnetic resonance tomography. The limits placed on spatial resolution (image sharpness) by the wavelength are circumvented by superimposing two fields. With the aid of a radio-frequency field in the MHz range and a locally variable static magnetic field, the sharp resonance absorption of magnetic nuclei in biological tissue is used in order to obtain the spatial distribution of the nuclear magnetization.

In particular, hydrogen atoms, which occur naturally in large numbers, allow medically meaningful images to be formed with a spatial resolution comparable to that of x-ray computed tomography and which show previously unseen contrasts between tissues. In addition, it is even possible to detect magnetic nuclei, such as ^{13}C, ^{19}F, ^{23}Na, ^{31}P, in spite of their low concentration in biological tissue; nevertheless, the value of the information thus gained does not approach that obtained through proton resonance.

Below we briefly describe the basic physical principles underlying magnetic resonance (MR) and the various methods of obtaining spatial resolution, as well as discussing some aspects of proton magnetization images and spectroscopy. A detailed description and discussion can be found in the relevant literature.

5.1.1 Macroscopic magnetization

All atomic nuclei with an odd number of protons or neutrons – i.e. roughly two-thirds of all stable atomic nuclei – possess an intrinsic angular momentum $\hbar\vec{I}$ or a (dimensionless) spin $\vec{I}$. This is always coupled with a magnetic dipole

moment, which is proportional to the angular momentum:

$$\vec{\mu} = \gamma \hbar \vec{I}. \tag{5.1}$$

$\hbar$ Planck's constant ($h/2\pi = 1.055 \cdot 10^{-34}$ Ws^2)
γ Gyromagnetic ratio
(for the proton, for example, $\gamma/2\pi = 42.577$ MHz/T)

In an externally applied magnetic field of flux density $\vec{B}$, this dipole moment has the potential energy

$$H = -\vec{\mu}\vec{B}. \tag{5.2}$$

It is known from quantum mechanics that particles cannot continuously change their angular momentum and their energy, but that these can only assume discrete values. These values emerge as expectation and eigenvalues of operators which replace the classical physical quantities. In this sense equations (5.1) and (5.2) are to be understood as operator equations.

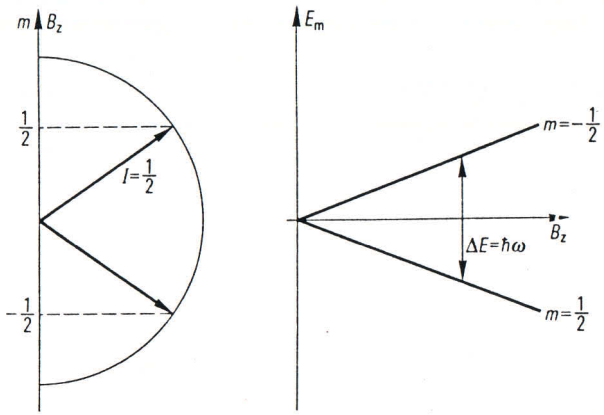

Fig. 5.1
(a) Possible orientations of a nuclear spin $I = 1/2$ in a magnetic field (the magnitude of the spin vector is $\sqrt{I(I+1)}$), and (b) energies of a nuclear spin $I = 1/2$ as a function of the magnetic field. For a quantum transition the difference in energy has to be added or removed in the form of light quanta of energy $\hbar\omega$

The magnitude of the nuclear spin (spin quantum number I) is the eigenvalue of the operator $\boldsymbol{I}^2$

$$\langle \boldsymbol{I}^2 \rangle = I(I+1) \tag{5.3}$$

(e.g. for the proton $I=1/2$ and for ^{23}Na $I=3/2$) and the component parallel to the magnetic field m is the eigenvalue of the operator $\boldsymbol{I}_z$

$$\langle \boldsymbol{I}_z \rangle = m(-I \leq m \leq I). \tag{5.4}$$

In a magnetic field B_z a nucleus with the quantum number I may therefore assume $2I+1$ discrete energy states (Fig. 5.1 a):

$$\langle \boldsymbol{H} \rangle = E_m = -\gamma \hbar B_z m. \tag{5.5}$$

A change in such a level always entails the absorption or emission of a photon (Fig. 5.1 b):

$$\hbar\omega = E_{m-1} - E_m = \gamma \hbar B_z. \tag{5.6}$$

Such processes were observed as hyperfine structure very early in optical spectroscopy of fluorescent gases and correctly interpreted by Pauli [5.4] in 1924.

In matter, atomic nuclei do not occur singly but only as an ensemble; for example 1 mm^3 of water contains $6.7 \cdot 10^{19}$ protons. In an external magnetic field, occupation of the energy states described by equation (5.5) proceeds in accordance with Boltzmann statistics:

$$N_{m-1}/N_m = \mathrm{e}^{-\gamma \hbar B_z/kT}. \tag{5.7}$$

k is the Boltzmann constant ($k = 1.38 \cdot 10^{-23}$ Ws/K).

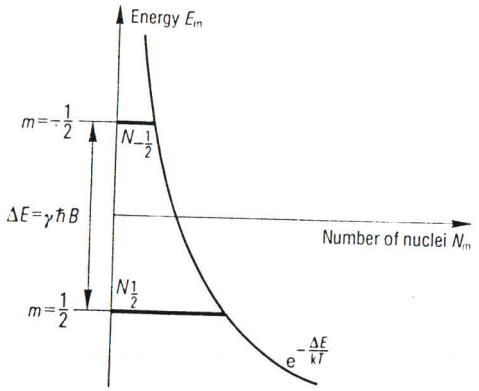

Fig. 5.2
Occupation of the energy states of a spin ensemble for $I=1/2$ according to the Boltzmann distribution

A surplus of nuclear magnetic moments aligned parallel to the magnetic field (for the same reason that the air pressure in the Earth's gravitational field decreases with increasing height) therefore results. Usually the magnetic interaction energy $\gamma \hbar B_z$ is much smaller than the thermal energy kT (for protons in a magnetic field of flux density 1 T (Tesla), the magnetic energy at room temperature is approximately a factor $8 \cdot 10^5$ smaller than the thermal energy). The exponential function in equation (5.7) can therefore be linearized. This leads to a macroscopic angular momentum with an associated magnetic moment, given by equation (5.1).

$$m_N = NI(I+1)\gamma^2 \hbar^2 B_z/3kT. \tag{5.8}$$

N is the number of nuclear spins

Instead of the macroscopic magnetic moment, the ratio of magnetic moment to sample volume, i.e. the nuclear magnetization, $M = \mathrm{d}m_N/\mathrm{d}v$, is often specified.

5.1.2 The Bloch equations

The phenomenon of nuclear magnetic resonance can be treated both in the framework of classical mechanics and in that of quantum mechanics. Since the mathematical formalism is simpler in classical mechanics, this will be the description chosen here, although an occasional recourse to the microscopic picture (as sketched in Section 5.1.1) will be unavoidable. The juxtaposition of the two representations – the quantum mechanical, in which according to Fig. 5.1 a spin can only assume discrete angles with respect to the external magnetic field, and the classical, in which – as will be shown in the following exposition – the macroscopic magnetization of equation (5.8) precesses around an external field with an arbitrary angle – occasionally leads to difficulties in comprehension. Thus, the reader should bear in mind the Bohr correspondence principle, which says that in the case of large quantum numbers (in this case, of many particles), the results of quantum mechanics become indistinguishable from the classical results.

In the case of thermal equilibrium, the magnetic moment (from equation (5.8)) of a probe with nuclear spins aligns itself parallel to the external magnetic field. If this equilibrium is disturbed, for example by suddenly changing the direction of the external magnetic field, then a torque $\vec{m} \times \vec{B}$ acts on the magnetic moment of the sample. Following the law of conservation of angular momentum, this torque causes a change in time of the angular momentum $1/\gamma \, \mathrm{d}\vec{m}/\mathrm{d}t$ of the probe, where

$$\frac{1}{\gamma} \mathrm{d}\vec{m}/\mathrm{d}t = \vec{\omega}_\mathrm{L} m/\gamma = \vec{m} \times \vec{B}. \tag{5.9}$$

This results in the precession of the nuclear magnetization around the direction of the magnetic field with the Larmor frequency

$$\omega_L = \gamma B, \tag{5.10}$$

analogously to the precession of an obliquely oriented top around the normal (Fig. 5.3). This precession (nuclear magnetic resonance) can be detected easily by measuring the induced alternating voltage in a coil surrounding the sample. It is the classical analog of the quantum transition expressed by equation (5.6).

For hydrogen nuclei, which are the most frequently occurring in nature, one obtains at 1 T a resonance frequency of 42.577 MHz. Table 1 shows resonance frequencies of other nuclei found in biological tissue and their relative sensitivity to detection at the same measuring frequency, taking into account their natural abundances.

Experience shows that after a finite period of time the thermal equilibrium which had previously been disturbed is reestablished. This process is described following Bloch (5.5) by phenomenologically adding relaxation terms to equation (5.9). It is assumed here that the components of the nuclear magnetization parallel and perpendicular to the magnetic field tend to their respective equilibrium states (M_0 and 0 respectively) at a rate proportional to the respective deviation from equilibrium:

$$\begin{aligned} dM_z/dt &= \gamma(\vec{M} \times \vec{B})_z + (M_0 - M_z)/T_1, \\ dM_{x,y}/dt &= \gamma(\vec{M} \times \vec{B})_{x,y} - M_{x,y}/T_2. \end{aligned} \tag{5.11}$$

M_0 denotes the equilibrium magnetic moment according to equation (5.8), T_1 the time constant (longitudinal relaxation time) with which the magnetization along the direction of the basic field is restored, and T_2 the time constant with which the transverse component decays (transverse relaxation time). The longitudinal relaxation is associated with the emission of energy to the surroundings (the crystal lattice in which the atomic nuclei are embedded) — thus it

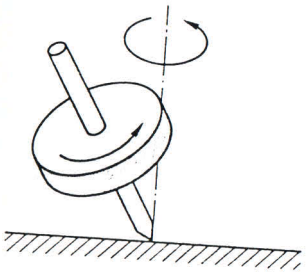

Fig. 5.3
Precession of a top in a gravitational field

Table 5.1
MR detection capabilities for various elements in biological tissue. The final column gives the relative edge length of the cube which would result in a constant signal

Element Isotope	MR frequency in MHz (at 1 T)	Average detection sensitivity in tissue at constant frequency	Resolution
^{1}H	42.58	100	1
^{2}H	6.53	0.006	25
^{13}C	10.71	0.025	16
^{14}N	3.08	0.31	7
^{17}O	5.77	0.049	13
^{19}F	40.06	0.006	25
^{23}Na	11.26	0.1	10
^{31}P	17.24	0.14	9
^{35}Cl	4.17	0.0084	23
^{39}K	1.99	0.011	21

is often referred to as spin-lattice relaxation (the probe therefore heats up; this effect is hardly measurable, however). The disappearance of the transverse magnetization is due to the mutual interaction of the nuclear spins, and is thus often referred to as spin-spin relaxation. Since in the case of transverse relaxation the longitudinal component of the magnetic moment, which determines the energy of the spin ensemble (equation 5.2), remains the same, the spin system does not lose any energy in the process and only the relationship of the phases of the individual spins to one another is lost. T_1 is an energy effect and T_2 an entropy effect.

5.1.3 Relaxation

The relaxation times express the mobility of the molecules in which the nuclei under consideration are located. Each nucleus is surrounded by other magnetic moments which are in constant thermal motion (Brownian molecular motion) and produce a continuously changing magnetic perturbation field. Spectral components which correspond to the precession frequency of the nuclear magnetization induce the longitudinal relaxation; the transverse relaxation, on the other hand, is determined by the frequency of collisions between the molecules as a whole.

The time behavior of the molecular motion is described quantitatively by the autocorrelation function $K(t)$. This is a measure of how long a molecule can 'remember' colliding with another molecule. If on the average two collisions

are separated by the correlation time τ_c, then given stochastic molecular motion one can assume an exponential decay for the autocorrelation function:

$$K(t) = K(0)\, e^{-\frac{|t|}{\tau_c}}. \tag{5.12}$$

In between two collisions the magnetic field b with components b_x, b_y, b_z, which acts from the nucleus (or possibly from the electron spin) of the one molecule on the nucleus of the other molecule, changes statistically by an amount $\pm b$. According to equation (5.10) the nucleus precesses with an additional phase $\delta\varphi = \pm\gamma b_z \tau_c$ around the z-component of this perturbation field. After n collisions, the result is therefore an average squared dephasing angle

$$\langle\varphi^2\rangle = n\delta\varphi^2 = n\gamma^2 b_z^2 \tau_c^2. \tag{5.13}$$

(for the average dephasing angle, of course, $\langle\varphi\rangle = 0$).

The time needed to dephase by one angular unit is the transverse relaxation time,

$$T_2 = \frac{n\tau_c}{\langle\varphi^2\rangle} = \frac{1}{\gamma^2 b_z^2 \tau_c}. \tag{5.14}$$

The reciprocal of the longitudinal relaxation time $1/T_1$ is a measure of the probability of transitions between two neighboring energy levels which a magnetic nucleus may assume in an external magnetic field following equation (5.5). This transition probability is proportional to the square of the average transition energy of the nuclear magnetic moment $\vec{\mu}$ with the stochastically fluctuating perturbation field $\vec{b}$ of the neighboring molecules

$$|\langle m+1|\vec{\mu}\vec{b}|m\rangle|^2 = \hbar^2\gamma^2(b_x^2 + b_y^2)\, I(I+1) \tag{5.15}$$

and to the probability $J(\omega)$ that the perturbation field has precisely the resonance frequency ω. The latter is given by the Fourier transform of the autocorrelation function, expressed in equation (5.12)

$$J(\omega) = \int K(t)\, e^{i\omega t}\, dt = \frac{2K(0)\,\tau_c}{1+\omega^2\tau_c^2}. \tag{5.16}$$

The reciprocal of the longitudinal relaxation time $1/T_1$ then follows by taking the product of equations (5.15) and (5.16), taking into account the normalization of $K(0)$, to give

$$1/T_1 = \frac{\gamma^2(b_x^2 + b_y^2)\,\tau_c}{1+\omega^2\tau_c^2}\, I(I+1). \tag{5.17}$$

Although the arguments for the derivation of T_1 and T_2 are only plausibility arguments, the results are essentially correct. For liquids, the correlation time is given by the ratio of viscosity to temperature. Biological tissue behaves in a similar manner to a viscous liquid.

Fig. 5.4 shows the relaxation time functions T_1 and T_2 measured by Bloembergen [5.6] for glycerine as a function of the ratio of viscosity to temperature. For T_2 there is a monotonic decrease according to equation 5.14 and for T_1 also a decrease according to equation 5.17, provided that the collision frequency is higher than the Larmor frequency ($\omega\tau_c \ll 1$, rapid molecular motion) and an increase when it is lower than the Larmor frequency ($\omega\tau_c \ll 1$). If $\tau_c \approx T_2$, i.e. $\tau_c \geq 1/\gamma b_z$, the transverse relaxation is no longer influenced by collisions; T_2 is then independent of the autocorrelation time.

For nuclei with a nuclear spin $I > 1/2$, the electrostatic interaction of the nuclear quadrupole moment with the electric field gradient, formed at the site of the nucleus because of the molecular structure, leads to additional relaxation. The short relaxation times of such nuclei often make the experimental observation of nuclear resonance more difficult.

Table 5.2 gives the order of magnitude for the relaxation times of protons in biological tissue [5.7]. The frequency dependence of T_1 may be described approximately by

$$T_1 \sim \omega^{0,3}. \tag{5.18}$$

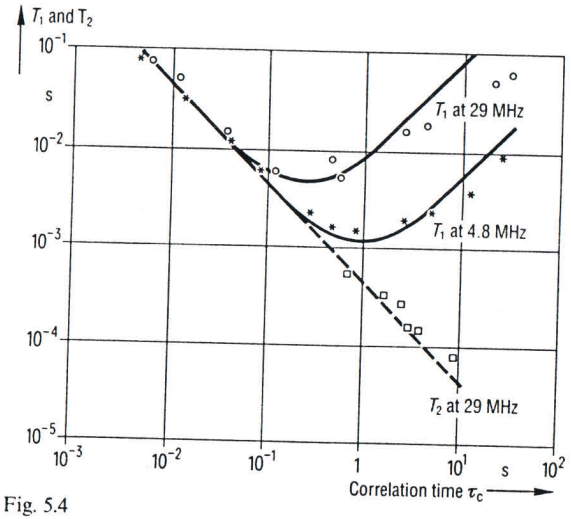

Fig. 5.4
Relaxation times T_1 and T_2 for the magnetic resonance of protons in glycerine as a function of the ratio of viscosity η to temperature ϑ [5.6]. η/ϑ is proportional to the autocorrelation time, τ_c

Table 5.2 Typical relaxation times T_1 (at 1 T) and T_2 [5.7].

Tissue	T_1 in s	T_2 in ms	Tissue	T_1 in s	T_2 in ms
Muscle	0.73 ± 0.13	47 ± 13	Spleen	0.68 ± 0.19	62 ± 27
Heart	0.75 ± 0.12	57 ± 16	Fat	0.24 ± 0.07	84 ± 36
Liver	0.42 ± 0.09	43 ± 14	Gray matter	0.81 ± 0.14	101 ± 13
Kidney	0.59 ± 0.16	58 ± 24	White matter	0.68 ± 0.12	92 ± 22

The transverse relaxation is independent of the Larmor frequency, in agreement with equation (5.14), but often several time constants are observed simultaneously.

It is the great range of values which the relaxation times assume in biological tissue which makes them so useful in medical diagnostics. When the spatial distribution is displayed, large contrasts are produced and diseased areas can be localized at once as a result of conspicuous differences in relaxation times. It is hoped that, in the future, T_1 and T_2 can be used to differentiate between tissues. Furthermore, functional studies can be carried out by adding paramagnetic contrast substances in order to shorten the relaxation times.

5.1.4 The magnetic resonance experiment

In the case of pulsed magnetic resonance, the equilibrium of the magnetization for a sample in a magnetic field is disturbed by a radio frequency (RF) pulse which matches the frequency of the Larmor precession. The linearly polarized radio-frequency field in the coil surrounding the sample can be thought of as the sum of two oppositely rotating circularly polarized fields, one of which has the same direction of rotation as the Larmor precession. Thus, in a reference frame which rotates at the nuclear precession frequency (rotating frame), a constant magnetic flux density B_1 acts, which in accordance with equation (5.9) causes the magnetization to precess about the axis of the B_1 field. In the laboratory system, the magnetization describes a combined precession movement around the basic static magnetic field B_z and the co-rotating field vector of the radio-frequency field B_1, which corresponds to a spiral path on the surface of a sphere (Fig. 5.5). The contrarotating radio-frequency field acts in the rotating reference frame as a perturbation having twice the Larmor frequency, with an effect which averages out.

Under the assumption that for the duration t of the radio-frequency pulse relaxation effects do not yet play a role, then the angle α which arises due to the influence of this pulse between the magnetization and the static magnetic field is

$$\alpha = \gamma B_1 t. \tag{5.19}$$

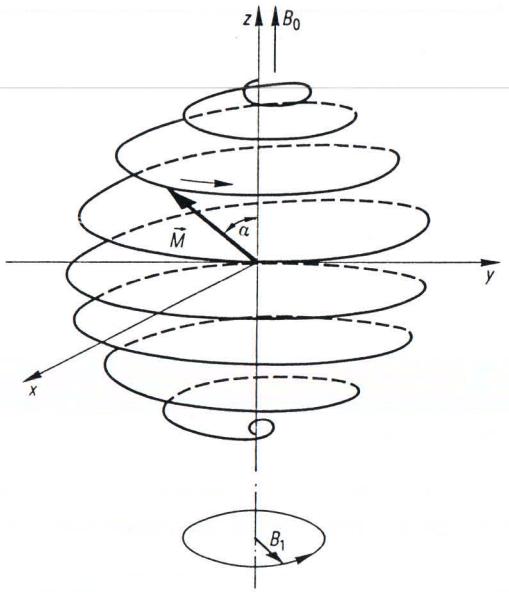

Fig. 5.5
Motion of the nuclear magnetization vector $\vec{M}$ under the influence of the static magnetic field B_0 and the circularly-polarized high frequency field B_1 with the Larmor frequency γB_0. The initial position of $\vec{M}$ is parallel to B_0; after time t, M is oriented an angle $\alpha = \gamma B_1 t$ to the direction of the static field

If the radio frequency pulse is switched off after the magnetization has reached a position perpendicular to the constant magnetic field ($\alpha = 90°$, hence a 90° pulse), it precesses with the maximum possible angle about the static field. Solving the Bloch equation (5.11) for the precessing transverse magnetization gives

$$M_{xy}(t) = M_0 \, e^{\left(-i\gamma B_z t - \frac{t}{T_2}\right)} \tag{5.20}$$

and for the longitudinal magnetization

$$M_z(t) = M_0 (1 - e^{-\frac{t}{T_1}}). \tag{5.21}$$

The precessing transverse magnetization can be detected easily via the signal induced in the radio-frequency coil (free induction decay, FID). The complex Fourier transform of this signal gives the magnetic resonance line – the dependence of the transverse magnetization on the frequency (Fig. 5.6). The real part of the Fourier transform describes the so-called absorption line

$$M_x(\omega) = \frac{M_0}{\pi} \frac{T_2}{1 + (\omega - \omega_0)^2 T_2^2}, \tag{5.22}$$

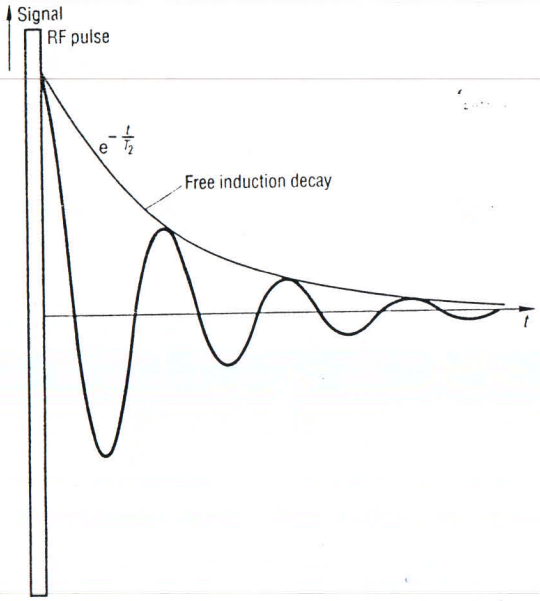

Fig. 5.6
(a) Induction signal following a 90° pulse about the y-axis of the rotating frame:
In order to be able to evaluate the phase of the transverse magnetization as well as its absolute value, the induction signal is mixed with an alternating voltage signal of similar frequency, giving a signal with the difference frequency (phase-sensitive demodulation)

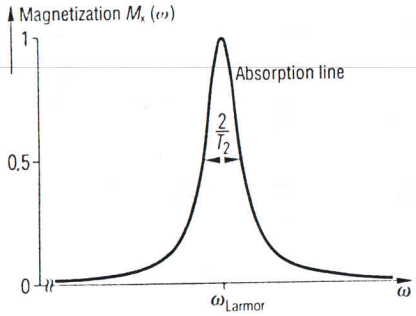

(b) Absorption signal:
The real part of the Fourier transform of the time signal in (a) represents the frequency dependence of the x-component of the precessing magnetization vector

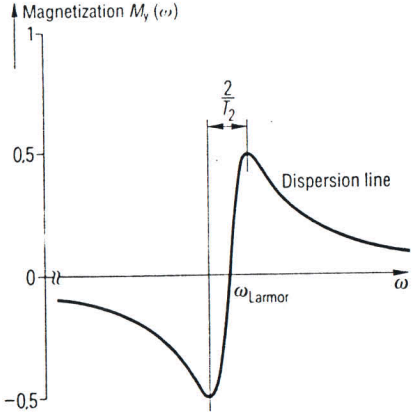

(c) Dispersion signal:
The imaginary part of the Fourier transform of the time signal in (a) represents the frequency dependence of the y-component of the precessing magnetization vector

and the imaginary part the dispersion line

$$M_y(\omega)=\frac{M_0}{\pi}\frac{T_2^2(\omega-\omega_0)}{1+(\omega-\omega_0)^2T_2^2}. \tag{5.23}$$

The half-width of the absorption and the distance between the inflection points of the dispersion line are given by the transverse relaxation time T_2:

$$\Delta\omega=2/T_2. \tag{5.24}$$

Protons in distilled water exhibit a line width of less than 1 Hz. Absorption and dispersion may also be measured directly by recording the effective resistance and inductivity of the coil surrounding the sample as a function of the frequency or of the field strength of the static magnetic field, e.g. by means of a bridge (continuous wave, CW). Because of the relatively long time required for taking measurements in comparison with the pulse method, continuous wave methods have, however, declined in importance.

The measurement of the transverse relaxation time T_2 through the duration of the free induction decay or through the line width only functions with very homogeneous magnetic fields. In practice the magnetic field usually varies from place to place, resulting in differing precession frequencies for the magnetization. Because of destructive interference, one therefore observes a shortened free induction decay (FID) or a (inhomogeneous) broadening of the line width. The form of the resulting resonance line essentially depends on the nature of the field distribution for the magnetic field ΔB_z; giving the effective transverse relaxation time

$$1/T_2^*=1/T_2+\gamma\Delta B_z \tag{5.25}$$

only describes the influence of field inhomogeneities in a general way since, of course, normally the signal decay is no longer exponential.

5.1.5 Pulse method for determining T_2

The destructive interference of precessing nuclei in inhomogeneous magnetic fields is reversible: if, after the free induction signal has decayed, a second radio-frequency pulse is applied which flips the component of magnetization perpendicular to the B_1 direction (in the rotating frame) by 180° (180° pulse, Fig. 5.7) the previously diverging magnetization converges again [5.8]. The Hahn spin-echo is observed with a reduced amplitude because of the transverse relaxation which has occurred in the meantime (Fig. 5.8).

Transverse relaxation is, however, not the only mechanism which determines the amplitude of the spin-echo. In the case of liquids in particular, molecules

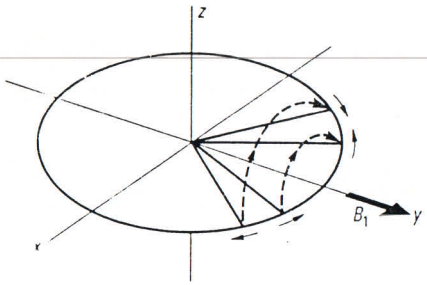

Fig. 5.7
A 180° pulse inverts the precession of two spins in relation to each other. View in the rotating frame

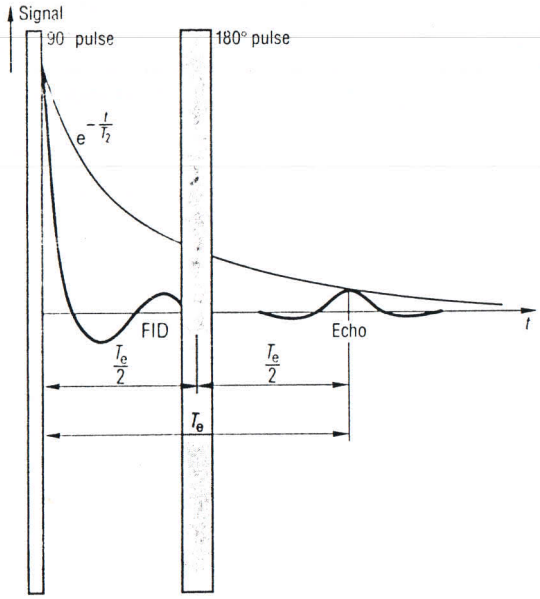

Fig. 5.8
The free induction decay signal (FID) which rapidly decays following a 90° pulse as a result of field inhomogeneities can be induced to occur again by means of a 180° pulse (with a reduced amplitude due to the transverse relaxation)

diffuse (according to the self-diffusion coefficient D) during the echo time T_e between the 90° pulse and observation of the echo from one position in the inhomogeneous static magnetic field to another; in accordance with the field difference (expressed by the magnetic field gradient G), the nuclei precess there with a different Larmor frequency and thus no longer contribute fully to the echo amplitude. This is given by the expression

$$M(T_e) = M_0 \, e^{-\frac{T_e}{T_2} - \frac{D\gamma^2 G^2 T_e^3}{12}} . \tag{5.26}$$

To determine T_2 and the self-diffusion coefficient D, the spin echo experiment is repeated with various echo times T_e and the ratio of logarithm of echo amplitude to echo time T_e plotted as a function of the echo time T_e^2. A straight line is obtained, which at $T_e = 0$ assumes the value $1/T_2$ and has a slope equal to the product $D \cdot G^2$ of the self-diffusion coefficient and field gradient squared.

A method of determining T_2 over a very much shorter measuring period was described by Carr and Purcell [5.9]: after applying a 90° pulse, a series of 180° pulses is made to follow after a time gap $T_e/2$. The 180° pulses are separated from each other by a time gap T_e (Fig. 5.9). Spin echoes then appear between the 180° pulses, the amplitude of the kth spin echo being given by

$$M(k) = M_0 \, e^{-k\frac{T_e}{T_2} - \frac{D\gamma^2 G^2 T_e^3 k}{12}} . \tag{5.27}$$

If the echo time T_e is chosen to be very short, then the influence of diffusion in the Carr-Purcell sequence can be kept small.

In practice the exact 180° condition on the refocussing pulses required for the Carr-Purcell experiment cannot be met; the unavoidable inhomogeneity of the radio-frequency coil surrounding the sample already prevents this. In

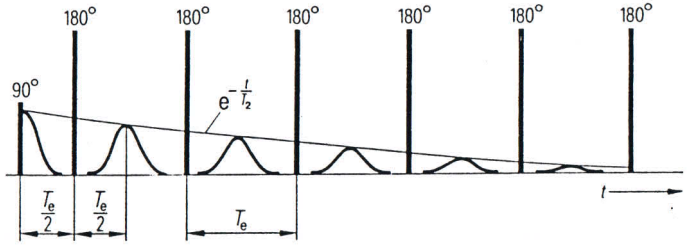

Fig. 5.9
Multiple echo (Carr-Purcell) sequence for the simple determination of the transverse relaxation time T_2

order to avoid cumulative deviations from equation (5.27) resulting from this, one can either alternate the phase of every second 180° pulse by 180° (Carr modification), or one can shift the phase of all the 180° pulses by 90° with respect to the 90° pulse (Gill-Meiboom modification [5.10]). All even echoes then show the correct amplitude, whereas the odd echoes are somewhat reduced, but not cumulatively.

5.1.6 Pulse method for determining T_1

The amplitude of a spin echo produced by a 180° radio-frequency pulse is determined through T_2; an RF pulse sequence consisting of three 90° pulses (Fig. 5.10) also generates a spin echo, the stimulated echo [5.8], the amplitude of which is characterized by T_1. After the second 90° pulse, the primary echo, characterized by T_2, appears, but with (compared to a 180° echo) half the amplitude. The other half of the signal is transformed into longitudinal magnetization and undergoes longitudinal relaxation during the time gap t between the second and third RF pulses. The third RF pulse transforms this longitudinal magnetization back into transverse magnetization. After a time $T_e/2$ following the third RF pulse, the stimulated echo appears with amplitude

$$M(t+T_e)=1/2\,M_0\,e^{-\frac{t}{T_1}-\frac{T_e}{T_2}-\frac{1}{8}D_f^2G^2(2/3\,T_e^3-2T_e^2t)}. \tag{5.28}$$

By systematically altering the time interval t between the second and third RF pulse it is then possible to determine T_1; however, as mentioned before, a priori the stimulated echo can only give a signal corresponding to half the total magnetization.

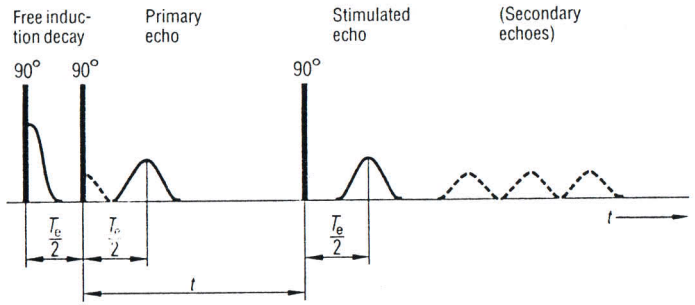

Fig. 5.10
Sequence of three 90° pulses for generating the stimulated echo. If there is a deviation from the 90° condition extra secondary echoes appear

If the 90° condition is not met exactly, three further (secondary) echoes appear, which can be explained as normal (i.e. determined by T_2) echoes and which are generated by the third RF pulse and the free induction decay after the first and second RF pulses, as well as by the first echo.

Another method of determining the longitudinal relaxation time consists in first inverting the magnetization by means of a 180° pulse and then probing the longitudinal magnetization resulting after time t

$$M_z(t)=M_0(1-2\,e^{-\frac{t}{T_1}}) \tag{5.29}$$

by means of the free induction decay (FID) produced by a 90° pulse (Fig. 5.11, inversion recovery). By repeating this sequence with various inversion times t, T_1 can be calculated. If, in particular, we look for the value t_0 at which $M_z(t)$ passes through zero, we find

$$T_1=t_0/\ln 2. \tag{5.30}$$

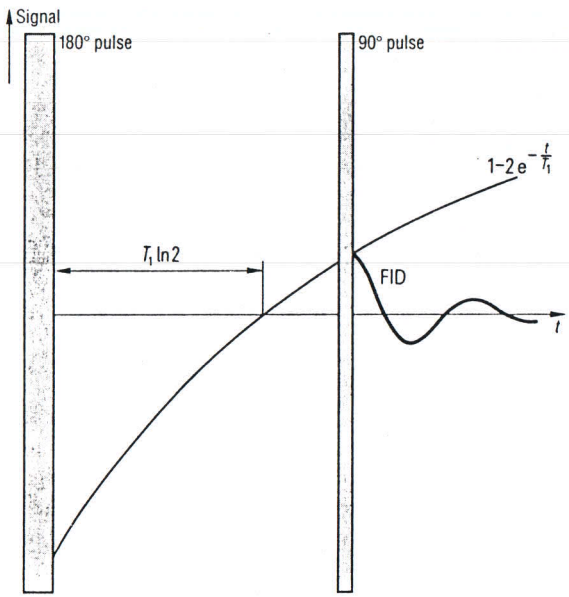

Fig. 5.11
Inversion recovery sequence for determining the longitudinal relaxation time T_1. By means of a 180° pulse, the magnetization is directed antiparallel to the constant magnetic field; (tending to decay back to the equilibrium state with the time constant T_1). The instantaneous value of the longitudinal component can be measured by flipping it by means of a 90° pulse into the transverse plane and evaluating the nuclear induction signal

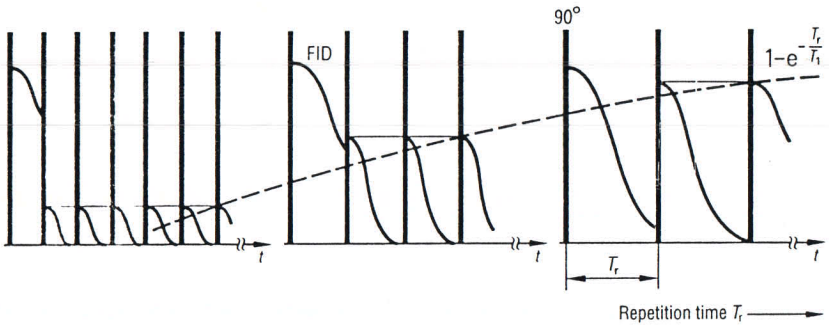

Fig. 5.12
Saturation recovery sequence for determining the longitudinal relaxation time T_1. The amplitude of the free induction decays for several 90° pulses following each other with the repetition time T_r depends exponentially on the ratio T_r/T_1. The magnetization settles into equilibrium after the second 90° pulse

Another method of determining T_1 involves generating free induction decays by means of 90° pulses which are repeated with repetition time T_r (Fig. 5.12). The initial amplitude of these FIDs is then given by

$$M(t_0) = M_0(1 - e^{-\frac{T_r}{T_1}}). \tag{5.31}$$

For short repetition times the signal vanishes, i.e. the spin system 'saturates' (saturation recovery). To calculate T_1, the magnetic resonance signal is recorded as a function of the repetition time.

5.1.7 Magnetic resonance spectroscopy

It has already been mentioned that the gyromagnetic ratio is a fixed constant for each nuclear species. In experiments where the atomic nuclei under investigation are embedded in different molecules, however, for the same magnetic field slightly different resonance frequencies are observed. This is caused by the molecular electrons responsible for the chemical bonds. These screen the external magnetic field, with the result that the atomic nucleus 'sees' different fields depending on the nature of the bond (chemical shift).

$$B_k = B_0 - \delta_k B_0. \tag{5.32}$$

In a molecular complex there are often several resonance lines, which may be attributed to individual groups of molecules. In quantitative terms the chemical shift δ_k is usually given in ppm (parts per million) relative to a reference line.

Besides the chemical shift, one also often observes a fine splitting of the magnetic resonance lines (Fig. 5.13). This is caused by the magnetic interaction (spin-spin coupling) between the nuclei, which does not act through space but again indirectly via the electrons of the chemical bonds. Such spectra are analyzed by using the energy function (Hamiltonian operator) with interaction energy J_{kl} between the different spins $\vec{I}_k$

$$H = -\sum_k B_z(1-\delta_k) I_{zk} + \sum_{k,l} J_{kl} \vec{I}_k \vec{I}_l, \tag{5.33}$$

whose eigenvalues and eigenfunctions are constrained to describe the measured spectrum in accordance with the molecular model adopted. In physical chemistry, elucidation of the molecular structure is often made possible in this way. In medicine it is hoped to be able to detect typical metabolites noninvasively in-vivo via their spectra.

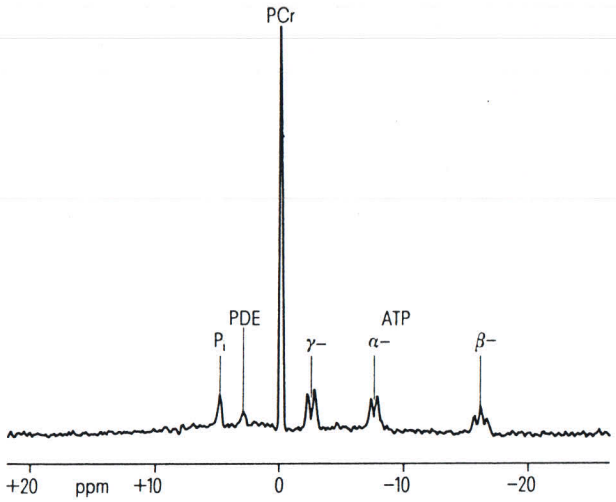

Fig. 5.13
^{31}P-spectrum of a human thigh muscle recorded with a surface coil at 2 T. On the basis of their different chemical shifts, the metabolites adenosine triphosphate (ATP), phosphocreatine (PCr), inorganic phosphate (P_i) and phosphodiester (PDE) can be distinguished. The three ATP lines correspond to the three locations of the phosphorous atom in the molecule; the lines are split further because of the interaction of the nuclei with other nearby nuclei

5.1.8 Signal-to-noise ratio

Nuclear magnetic resonance in-vivo is only meaningful if the parameters of interest, such as number of nuclei, relaxation times, diffusion constant, chemical shift, spin-spin coupling, etc., can be measured in a way which permits spatial resolution, i.e. in a small subvolume V (Voxel) of the patient to be examined (Fig. 5.14). Before going into the various methods of spatial resolution, however, the fundamental limit which restricts such measurements will be defined.

This limit has its origin in the fact that the thermal motion of the electrons in the coil for detecting the magnetic resonance and the Brownian molecular motion in the object to be measured (the human body) produce a noise voltage [5.11], which competes with the magnetic resonance signal. Following Nyquist, this is given by:

$$U_N = \sqrt{(2/\pi)\, k\, T_N\, R \Delta\omega}. \tag{5.34}$$

T_N is the noise temperature
R is the resistance of the detection coil and
$\Delta\omega$ is the detection bandwidth (angular frequency).

The product $T_N R$ can be resolved into a coil part and a sample part

$$R T_N = R_{coil}\, T_{coil} + R_{sample}\, T_{sample}. \tag{5.35}$$

The resistance R_{sample} imparted to the measuring coil because of the sample may be calculated from the dissipated power converted in the sample

$$P_{sample} = 1/2 \int_{sample} \sigma E^2 \, dv. \tag{5.36}$$

where

σ is the electrical conductivity and
E is the electric field strength.

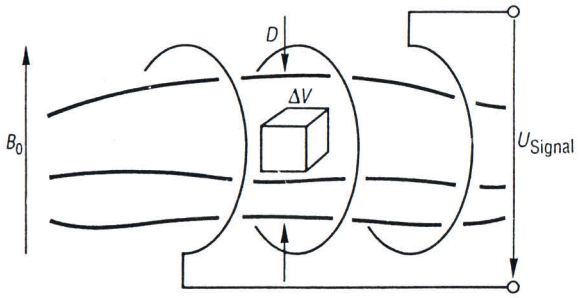

Fig. 5.14
Detection element ΔV inside a patient, surrounded by a radio-frequency coil

From Maxwell's equations we obtain for a homogeneous radio-frequency magnetic field with angular frequency ω and amplitude B_1

$$E = 1/2\, \omega B_1 r_\perp, \tag{5.37}$$

where

$r_\perp$ is the radius perpendicular to the B_1-field,

with the result that the power converted in the sample is

$$P_{sample} = 1/8\, \omega^2 \sigma B_1^2 \int_{sample} r_\perp^2 \, dv. \tag{5.38}$$

This is proportional to the "moment of inertia"

$$\Theta = \int_{sample} r_\perp^2 \, dv, \tag{5.39}$$

and thus depends on the shape of the sample and its orientation. For a cylindrical sample of length l and diameter D, with the RF field oriented perpendicularly to the axis,

$$\Theta = \frac{\pi}{64}\left(D^4 l + \frac{4}{3} D^2 l^3\right)$$

and, with the RF field oriented parallel to the axis,

$$\Theta = \frac{\pi}{32} D^4 l.$$

From the dissipated power it is then possible to calculate the sample resistance, according to the ratio of dissipated power to effective value of the current squared, giving

$$R_{sample} = 1/\sigma\omega^2 B_i^2\, \Theta, \tag{5.40}$$

where B_i denotes the field per unit of current, i.e. a geometrical factor for the RF coil. For the center of a cylindrical coil

$$B_i = \frac{\mu_0}{2n\sqrt{a^2 + l^2/4}}. \tag{5.41}$$

μ_0 Permeability in a vacuum $= 1.256 \cdot 10^{-6}$ Vs/Am
n Number of turns
l Length of coil
a Radius of coil.

The pure coil resistance R_{coil} can also be expressed by the quality factor of the coil

$$Q_0 = \frac{\omega \cdot (\text{energy stored in the coil})}{\text{power dissipated in the coil}} \tag{5.42}$$

and is therefore found to be

$$R_{coil} = \frac{\omega B_i^2 V_{sample}}{2\mu_0 \eta Q_0}. \tag{5.43}$$

Here V_{sample} represents the useful volume in the coil taken up by the sample, while for the 'field distribution factor' or 'filling factor'

$$\eta = B_i^2 V_{sample} / \int B_i^2 \, dv. \tag{5.44}$$

The noise voltage given by equation (5.34) is to be compared with the voltage induced in the coil by the precessing magnetization (equation 5.8)

$$U_{Signal} = M B_i \omega \Delta V. \tag{5.45}$$

following a 90° pulse.

The signal-to-noise ratio is then seen to be independent of the geometrical factor of the coil and is given by

$$S/R = \sqrt{\frac{\pi}{18k^3}} I(I+1)\hbar^2\gamma \frac{N_v \omega}{T_{sample}\sqrt{\frac{V_{sample} T_{coil}}{2\mu_0 \eta Q_0 \omega} + \frac{1}{4}\sigma\Theta T_{sample}}} \frac{\Delta V}{\sqrt{\Delta\omega}}. \tag{5.46}$$

where

N_V is the spin density.

For small samples and a low coil quality factor Q_0, the signal-to-noise ratio is proportional to the measuring frequency $f^{3/2}$; for a high coil quality factor and a low coil temperature, it is directly proportional to the measuring frequency. For a fixed sample volume V_{sample}, the quality of the magnetic resonance coil is determined only by the product of the field distribution factor (filling factor) and the unloaded quality factor ηQ_0. In magnetic resonance tomography the latter is usually so large that the noise induced by the patient predominates over the coil noise, with the result that (for constant detection bandwidth) the signal-to-noise ratio may be regarded as proportional to the static magnetic field strength[1].

[1] Increasing the signal-to-noise ratio by restricting the detection band width is only possible to a limited extent; in order for there to be no loss of information, it is necessary that $\Delta\omega > 1/T_2$. Of course the S/R can also be increased by multiple (n) measurements ($S/R \sim \sqrt{n}$), but this is at the expense of increased measuring time. The number of measurements for a given measuring time T_M is limited by T_1 ($n \sim T_M/T_1$). The relaxation times T_1 and T_2 of the sample and the measuring time T_M can be taken into account in equation (5.46) by replacing $1/\sqrt{\Delta\omega}$ by $\sqrt{T_2 \cdot T_M/T_1}$. These physical dependences are the reason why the number of protons that can be detected by means of a magnetic resonance experiment is limited. At room temperature $5 \cdot 10^{18}$ protons in a liter of physiological saline solution in a magnetic field of 1 T give roughly $S/R \approx 1$ ($n = 1$). For comparison: 1 mm³ of water alone contains $6.7 \cdot 10^{19}$ hydrogen nuclei.

5.2 Methods of spatial resolution

5.2.1 Classification of imaging procedures

To localize the magnetization, magnetic field gradients are superimposed onto the homogeneous static magnetic field during the excitation and measurement of the magnetic resonance signal, with the result that the frequency of the magnetic resonance signal becomes a function of position. Various strategies have been developed for the effective measurement of the spatial distribution of the nuclear magnetization [5.12].

If one imagines the object to be measured as being divided into N^3 volume elements (voxels), then in the simplest case each voxel can be measured in turn; the measuring time for the whole object is thus proportional to N^3. If it is possible to simultaneously register an entire row consisting of N voxels, then in order to obtain the contribution of an individual voxel it is necessary to measure the row N times under different conditions. The measuring time for the whole object thus remains the same, but the signal-to-noise ratio is improved by a factor of $\sqrt{N}$ in comparison to the point-by-point measurement. This is due to each volume being measured N times, although under different measuring conditions, thus reducing the noise by averaging. Extending this principle to the scanning of surfaces and volumes (Fig. 5.15) leads, given the same measuring time, to a further improvement in the signal-to-noise ratio by a factor of $\sqrt{N}$ in each case.

In spite of the above considerations, scanning by volume is not always the most advantageous procedure; this is because the relaxation times T_1 and T_2 of the object being examined place constraints on the times within which a measurement can be repeated. Within the transverse relaxation time T_2 typically N measuring points can be scanned; after each excitation of the total object volume, it is then necessary, before being able to measure a further N points, to wait a time of the order of the longitudinal relaxation time T_1, during which the excited nuclear spin system returns to its original state. In order to scan the entire volume one must therefore figure with measuring times of $N^2 T_1$; thus for a 64^3 matrix and typical measurement repetition times of 0.5 s, this would amount to 34 min.

For planar scanning, the measuring time is only of the order of NT_1, i.e. in the above example around 30 s, so that in the interest of improving the spatial resolution the scan matrix may be enlarged to $N = 256$. The measurement of further layers (or 'slices') in the object is also possible without a significant increase in the measuring time, since other slices which have not previously been excited can be measured in the relaxation pauses.

Often, it is not actually interesting to study the spatial distribution of the magnetization at all, but rather to conduct as precise a determination as possible

of a particular magnetic resonance parameter – for example the spectral splitting – at a particular location.

Limiting the object to be measured to a partial volume can be done in various ways: by employing a measuring coil which only receives signals from the subregion of interest. These so-called surface coils are popular, because of their improved signal-to-noise ratios compared with whole-body coils (equation 5.46): in this way the 'moment of inertia' (equation 5.39) can be significantly reduced; on the other hand, the inhomogeneity of the radio-frequency field is a disadvantage.

Limiting the resonance volume by shaping the main static magnetic field [5.13, 5.14] has not proved acceptable, since this 'field focus" is technically difficult to vary with the necessary flexibility in regard to its position and range. This is where the strength of 'selective excitation' lies.

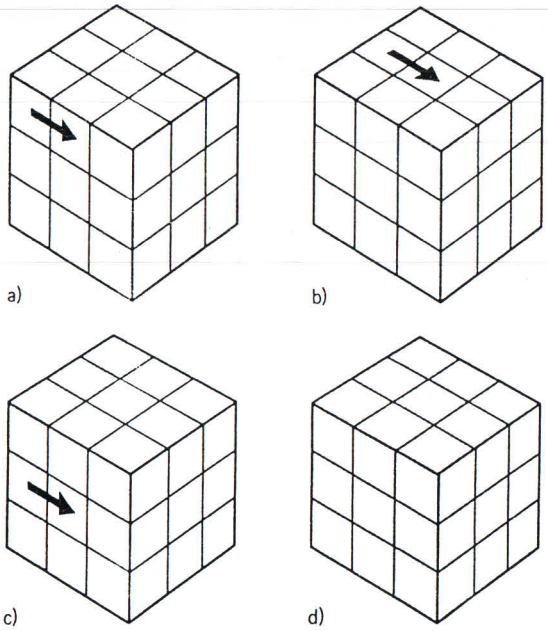

Fig. 5.15
Point (a), line (b), surface (c) and volume (d) scanning of an object in a three-dimensional scan matrix

5.2.2 Selective excitation

It has already been mentioned in Section 5.1.5 that the actual magnetic resonance signal is preceded by the excitation caused by a radio-frequency pulse, the frequency of which coincides with the Larmor frequency. If during a 90° pulse a magnetic field gradient G_z is superimposed onto the object to be measured in addition to the homogeneous main static magnetic field B_0 (Fig. 5.16), then the resonance frequency varies according to

$$\omega_{\text{Larmor}} = \gamma(B_0 + G_z z) \tag{5.47}$$

along the object, and only those nuclei in the slice with position

$$z = (\omega_{\text{Larmor}} - \gamma B_0)/\gamma G_z \tag{5.48}$$

are excited. Thus, only these nuclei yield a magnetic resonance signal, while all the others remain unaffected. In a similar way the magnetization in a slice can be inverted by means of gradient-superimposed (selective) 180° pulses.

The case of a selective 90° pulse will be examined in the following in greater detail. For small angles of rotation about the axis of the RF-field $\gamma B_1 \, dt$ the Bloch equations can be linearized, giving (5.9) for the response of the spin system to an amplitude-modulated RF pulse of frequency ω_{Larmor}

$$dM_\perp = \gamma M_0 B_1(t) e^{(-i\omega t)} dt, \tag{5.49}$$

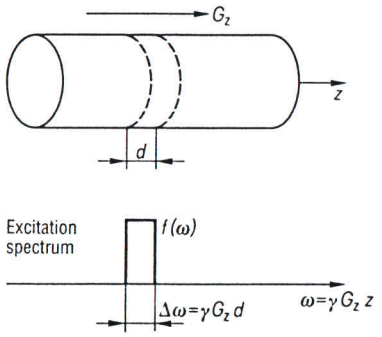

Fig. 5.16
Selective excitation of a slice in a cylindrical object. A gradient along the object allows a spatial variation in the magnetic resonance frequency, with the result that the spectrum of the applied 90° pulse determines position and thickness of the slice

i.e. to a first approximation, the spatial dependence of the transverse magnetization (in the frame rotating with γB_0) is given by the Fourier transform of the selective radio-frequency pulse

$$M_\perp(z) = \gamma M_0 \int_0^{t_{max}} B_1(t)\, e^{-i\gamma G_z z t}\, dt. \qquad (5.50)$$

Here, the x and y components of the transverse magnetization have been combined in the complex quantity $M_\perp = M_x + iM_y$.

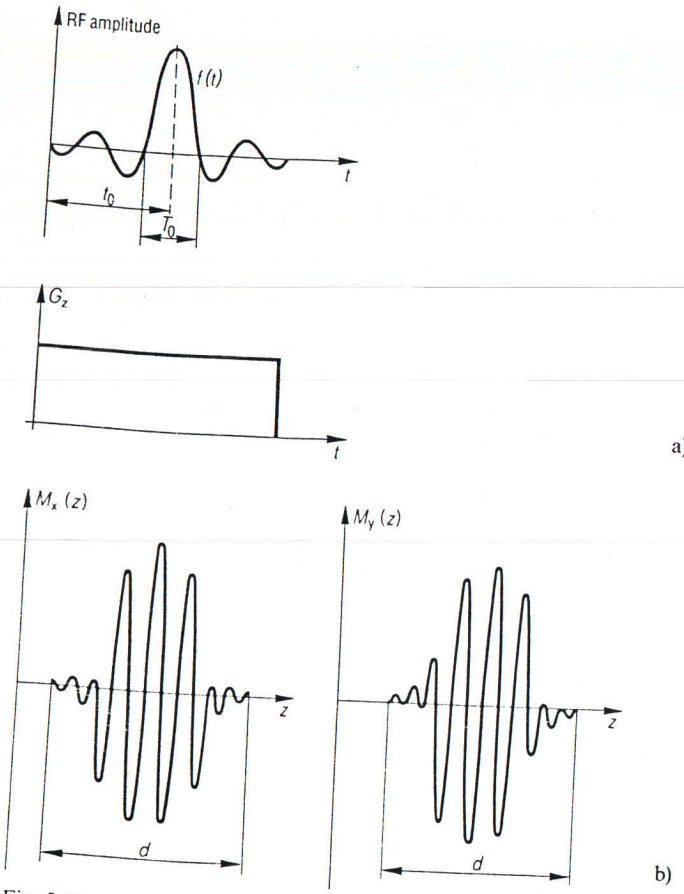

Fig. 5.17
(a) To excite a rectangular slice, the radio frequency of the 90° pulse is modulated with a sinc (sin x/x) function
(b) x and y magnetization (in the rotating frame) as a function of the slice thickness following selective excitation; the magnetization rotates in a spiral fashion

In order to achieve as rectangular a distribution of the transverse magnetization as possible over the thickness of the slice, it is necessary to impose a time dependence on the exciting RF pulse, corresponding to the sin x/x (sinc) function (Fig. 5.17a):

$$B_1(t) = B_1(t_0)\frac{\sin\left(\frac{1}{2}\gamma G_z\, d(t-t_0)\right)}{\frac{1}{2}\gamma G_z\, d(t-t_0)}. \quad 0 \le t \le 2t_0 \qquad (5.51)$$

where

d is the slice thickness desired and
t_0 is the half-length of the pulse.

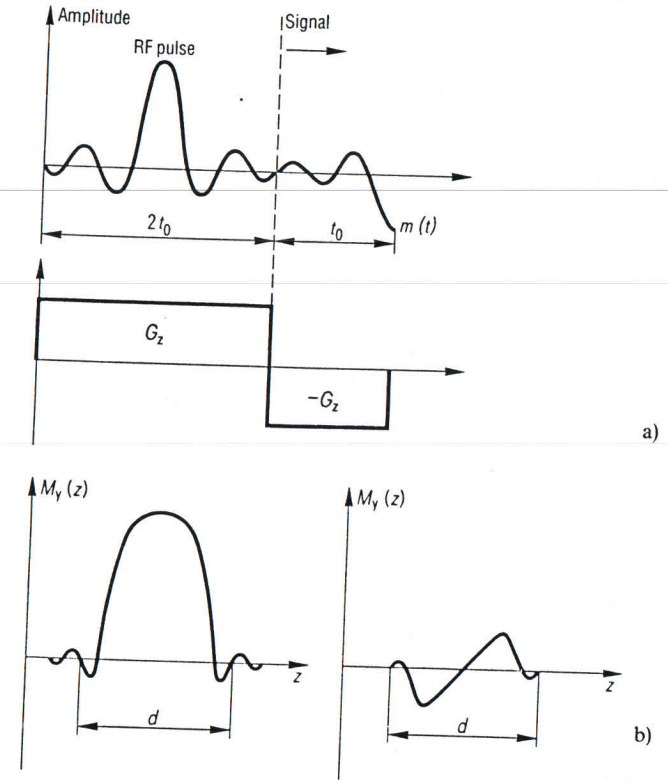

Fig. 5.18
(a) In order to realign the transverse magnetization, which rotates immediately after the selective 90° pulse, an interval with a reversed-polarity field gradient is added on after the RF pulse.
(b) x and y magnetization as a function of slice thickness for selective excitation with refocussing. The remaining oscillation is an expression of the non-linearity of the Bloch equations. It can be improved by means of modified RF modulations

In accordance with equation (5.50), it follows for the transverse magnetization that

$$M_\perp = M_0 \,\mathrm{rect}\left(|z| - \frac{d}{2}\right) \mathrm{e}^{i\gamma G_z z t_0} \tag{5.52a}$$

(rect = rectangular function)

an oscillating function (Fig. 5.17b) with width

$$d = 4/\gamma G_z T. \tag{5.52b}$$

where

T is the distance between the two innermost zeroes of the sin function.

Although the 'selective RF pulse' has flipped each 'spin' into the transverse plane along the slice, this is only in its own co-rotating frame. After termination of the RF pulse the magnetization is therefore rotated. Reversing the polarity of the field gradient during a period t_0 (Fig. 5.18a) following the RF pulse [5.15] aligns (refocusses) all spins so that they are parallel again (Fig. 5.18b). Instead of the reversed gradient it is also possible to use a 180° pulse and a gradient with the same polarity.

Linearization of the Bloch equations is a good approximation up to angles of rotation of 30°, but larger angles, such as 90° or 180°, require numerical solutions. Thus, for a sinc-shaped 90° pulse with subsequent refocussing there still remains a small oscillation of the magnetization across the slice. This can be avoided by means of modified RF pulse shapes.

5.2.3 Imaging procedures

In order to measure the spatial distribution of the precessing transverse magnetization following a selective slice excitation, a magnetic field gradient G is superimposed onto the main static magnetic field in the slice. As a result, the Larmor frequency is constant in strips perpendicular to the direction of the gradient the amplitude of the magnetic resonance signal as a function of the frequency corresponds in each case to the sum of all the 'spins' in this strip, i.e. it represents the projection of the magnetization onto the field gradient [5.16].

Following Fig. 5.19 one obtains for the projection

$$P(r, \varphi) = \int M_\perp(x, y)\,\mathrm{d}l. \tag{5.53}$$

What is actually measured experimentally is the time signal; for a frame rotating with γB_0

$$m_\perp(t, \varphi) = \int P(r, \varphi)\,\mathrm{e}^{-i\gamma G r t}\,\mathrm{d}r. \tag{5.54a}$$

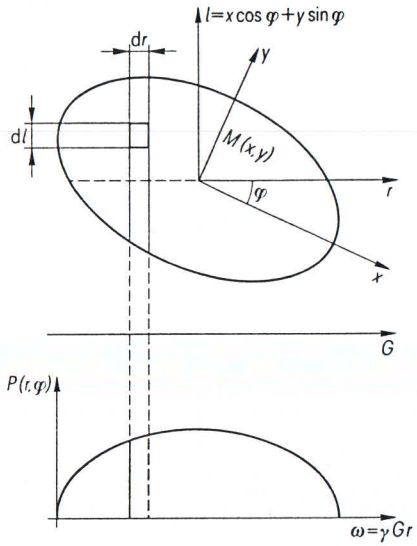

Fig. 5.19
The magnetic resonance signal as a function of the frequency for an object in a linear magnetic field gradient G represents the projection of the transverse magnetization onto the direction of the gradient

Introducing a 'normalized time'

$$k = \gamma G t \tag{5.55}$$

the measured signal

$$m_\perp(k, \varphi) = \int P(r, \varphi)\,\mathrm{e}^{-ikr}\,\mathrm{d}r \tag{5.54b}$$

and the projection

$$P(r, \varphi) = \int m_\perp(k, \varphi)\,\mathrm{e}^{ikr}\,\mathrm{d}k \tag{5.54c}$$

are seen to be Fourier transforms of each other. Inserting equation (5.53) into equation (5.54) it then follows that a set of measured signals $m_\perp(q, \varphi)$ in successively rotated gradients is the two-dimensional Fourier transform of the magnetization

$$m_\perp(k, \varphi) = \int M_\perp(x, y)\,\mathrm{e}^{-i(k_x x + k_y y)}\,\mathrm{d}x\,\mathrm{d}y. \tag{5.56}$$

The space defined by the Fourier inverse of the space in which the object to be measured is located is thus scanned by means of a grid in polar coordinates. However, the pictorial representation of the magnetization takes place in Cartesian coordinates. Instead of a re-interpolation of the measured data onto a Cartesian grid and a two-dimensional Fourier transform, it is also possi-

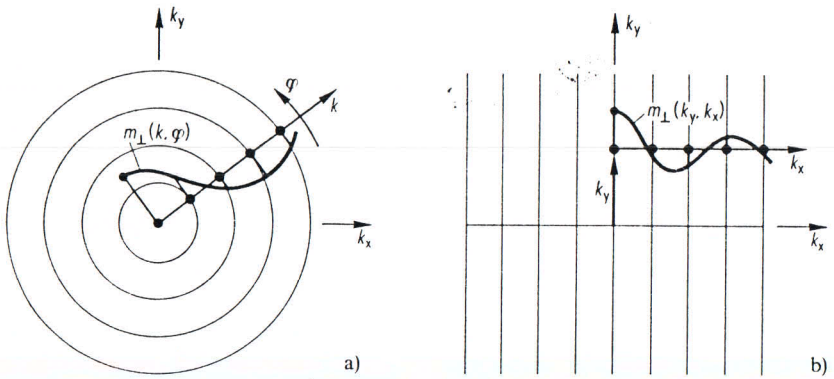

Fig. 5.20
Scanning of the Fourier space by means of (a) polar and (b) Cartesian coordinates

ble to calculate the projection from the measured signal by means of a one-dimensional Fourier transform and then reconstruct the image through filtered back projection.

Unlike x-ray computed tomography, which only permits the construction of images from successively rotated projections, magnetic resonance tomography offers another possibility. Instead of employing a grid in polar coordinates, one can scan the Fourier space with a grid in Cartesian coordinates (Fig. 5.20). This then allows a direct reconstruction of the image by means of the two-dimensional 'Fast Fourier Transform (FFT)' [5.17] within a few seconds.

After excitation of a slice in the object through a selective RF pulse, the magnetization is dephased for a certain length of time t_y in the gradient G_y and then read out within a time t_x in the projection gradient G_x (Fig. 5.21 a). After a certain waiting period, during which thermal equilibrium is reestablished, this sequence is repeated with different values for the gradient G_y or coding time t_y [5.18]. The precessing transverse magnetization in the rotating coordinate frame as a function of the dephasing gradient strength or time and the readout time is then given by

$$m_\perp(G_y t_y, t_x) = \iint M_\perp(x, y)\, e^{-(i\gamma(G_y y t_y + G_x x t_x))}\, dx\, dy. \qquad (5.57)$$

A two-dimensional Fourier transform applied to this signal directly yields the desired spatial distribution of the transverse magnetization.

5.2.4 Pulse sequences and contrast

In practice, a sequence modified from that shown in Fig. 5.21 a is used (Fig. 5.21 b), which measures a spin echo signal. The reason is that, on the one hand, inhomogeneities in the main static magnetic field are compensated

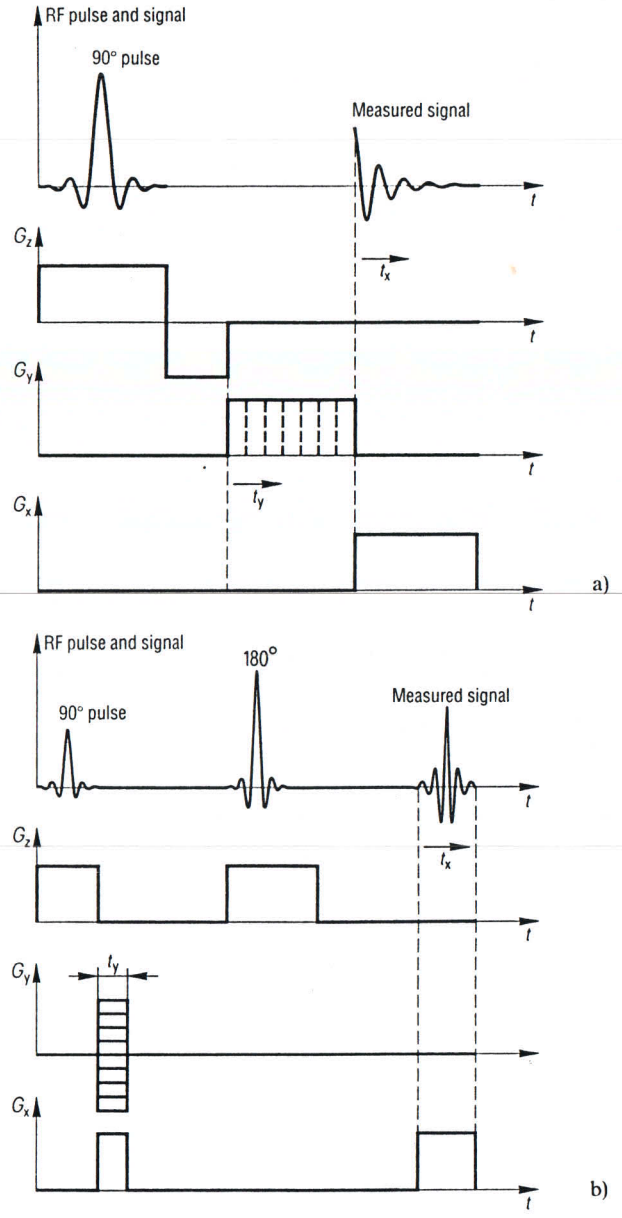

Fig. 5.21
(a) Sequence for measuring a slice by scanning the Fourier space in Cartesian coordinates. After a selective excitation in the gradient G_z, the magnetization is first coded with G_y and then read out in G_x.
(b) Sequence for measuring a slice with a spin-echo sequence

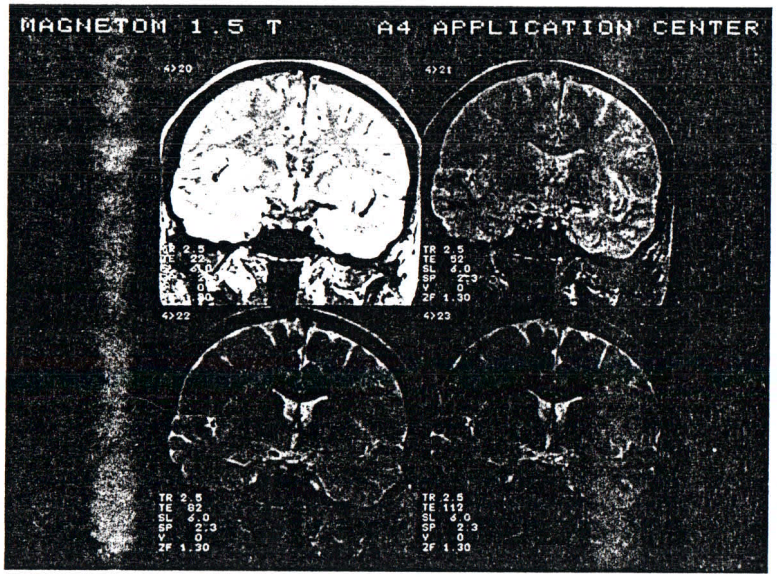

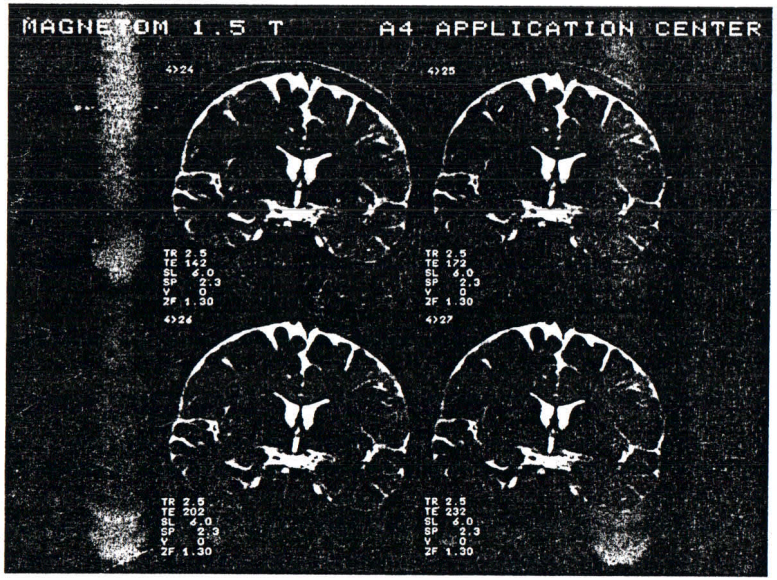

Fig. 5.22
Multiple echo image of a normal volunteer: the echo time increases by 30 ms from image to image. Areas with long transverse relaxation times remain bright

for, at least in the direction of the coding gradient and, on the other hand, that by reading out the spin echo a whole line of the Fourier space is scanned, and not just half a line as before. The total scan time is thus halved.

According to the sampling theorem, the size of an image element (pixel) is determined by the duration of the maximum scanning period

$$\Delta x, y = \pi/\gamma G_{x,y}\, t_{x,y\,\max}; \tag{5.58a}$$

and the size of the scan matrix then follows from the maximum object diameter D according to

$$N_{x,y} = D/\Delta x, y. \tag{5.58b}$$

In practice $N_{x,y}$ is rounded up to a power of two, in order to be able to employ the fast Fourier transform (FFT) algorithm.

As already mentioned, the use of a selective 180° pulse permits the measurement of additional slices in the breaks between repetitions without prolonging the measuring time. The repeated application of 180° pulses in a sequence allows several images to be constructed with varying T_2 weighting for a single slice, from which the transverse relaxation times can then also be calculated locally. Fig. 5.22 shows an example of such a multiple-echo series.

The local transverse magnetization in a spin-echo sequence may be influenced externally through the echo time T_e and the time interval T_r with which the sequence is repeated. For a single echo sequence

$$M_\perp(x, y) = N_v\left(1 - 2\,e^{-\left(T_r - \frac{T_e}{2}\right)\frac{1}{T_1}} + e^{-\frac{T_r}{T_1}}\right) e^{-\frac{T_e}{T_2}}. \tag{5.59a}$$

where

N_v is the local spin density.

For the case $T_r \gg T_e$ this relation may be simplified to

$$M_\perp(x, y) = N_v\, e^{-\frac{T_e}{T_2}}\left(1 - e^{-\frac{T_r}{T_1}}\right). \tag{5.59b}$$

The contrast resulting in the image of the magnetization is given by the difference in signals $M_1 - M_2$ between two regions of unequal magnetization. By choosing the pulse parameters T_r and T_e it can be enhanced, inverted, or even made to vanish. The head scan images in Figs. 5.23a and 5.23b are instructive; here white matter yields a stronger signal than gray matter for short repetition times, whereas for long repetition times and long echo times the situation is

a)

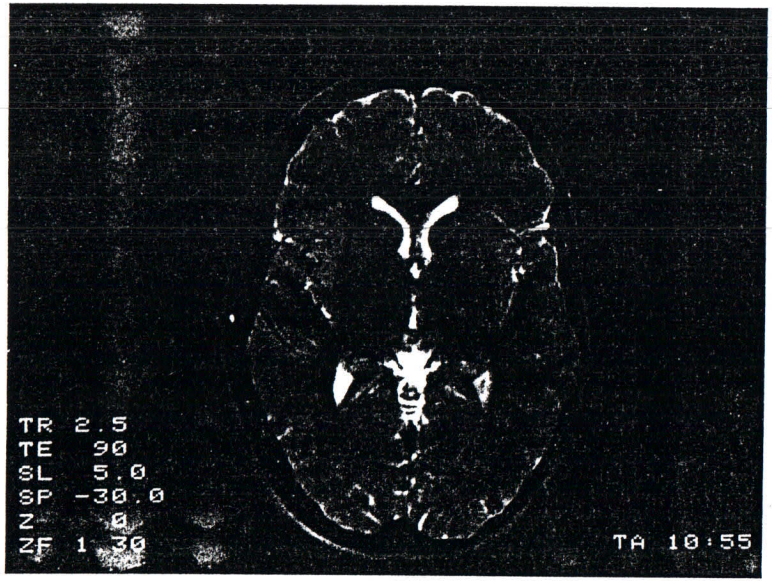

b)

Fig. 5.23
(a) Head scan taken with a repetition time of 500 ms and an echo time of 22 ms. The white matter appears brighter than the gray matter.
(b) The same slice as in (a), but with a repetition time of 2.5 s and an echo time of 90 ms. The white matter now appears darker than the gray matter

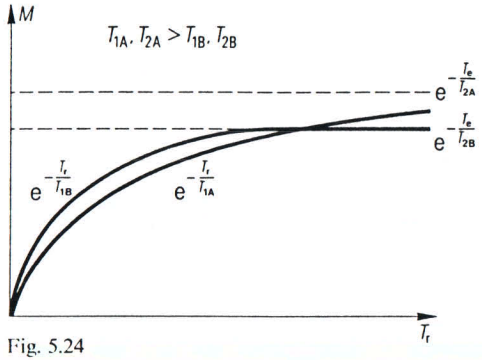

Fig. 5.24
Dependence of the transverse magnetization on the repetition time for tissue with larger and smaller T_1 and T_2 values, respectively

reversed; Fig. 5.24 illustrates this graphically. In addition two images taken with different repetition times and the same echo time also make it possible to determine quantitatively the distribution of the longitudinal relaxation times T_1.

5.2.5 Flow in the magnetic resonance image

It has already been mentioned in Sect. 5.1.5 that the magnetic resonance signal is not only characterized by the relaxation times, but also by the diffusion of the nuclei under observation. However, in biological tissue the diffusion constant is so small that it does not lead to any effect in a normal spin-echo image – in order to determine the diffusion constant, additional strong gradients are required before and after the 180° pulse. On the other hand, the nature of the image is significantly influenced by flowing nuclei, i.e. by blood flow.

Here, it is necessary to make a fundamental distinction between two cases: flow perpendicular to the excited slice and flow within the excited slice. In the first case it is observed that the magnetic resonance signal increases initially at low velocities and then decreases strongly at high velocities (Fig. 5.25). The initial increase in signal, which is often described as a paradoxical enhancement, can be explained by the fact that in the repetition pauses, nuclear spins which no longer carry any magnetization from the previous excitation, i.e. which are unsaturated, flow into the slice under examination. At high velocities, on the other hand, some of the excited spins flow out of the slice being measured between the 90° and 180° pulse and therefore no longer contribute to the magnetic resonance signal.

Formally, this may be described by introducing effective relaxation times T_1' and T_2' [5.19], which are shortened compared to the original relaxation as

a result of flow terms

$$1/T_1' = 1/T_1 + v/d, \tag{5.60a}$$

$$1/T_2' = 1/T_2 + v/d, \tag{5.60b}$$

where

v is the velocity of flow perpendicular to the slice and
d is the thickness of the slice.

If we examine vessels containing flowing matter within a slice by means of a multiple echo sequence, then in all odd-echo images we observe a signal intensity which decreases with the flow velocity; the signal intensity remains the same, however, in the even echoes (at least for laminar flow).

This is due to the fact that if transverse magnetization flows along a field gradient G, then in the time $T_e/2$ between the 90° and 180° pulses a phase shift builds up relative to static magnetization,

$$\varphi = \int_0^{T_e/2} \gamma G v \, dt = \gamma G v \, T_e^2/8 \tag{5.61}$$

which is inverted by the 180° pulse and assumes the value $\gamma G_v T_e^2/4$ in the

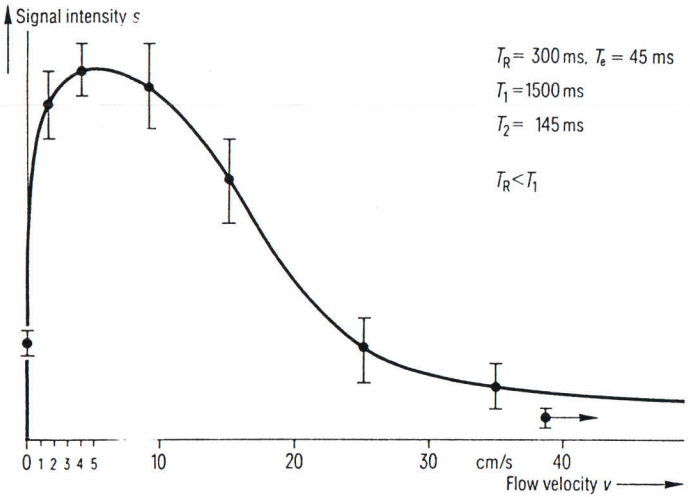

Fig. 5.25
Dependence of the signal intensity of matter flowing perpendicular to the slice on the flow velocity

echo (Fig. 5.26). This phase is reduced to zero again in the second and all subsequent even echoes.

In magnetic resonance tomography, the phase shift due to flow is produced (in the odd echoes) by the gradient used for imaging. The distribution of phases, which is linked to the distribution of flow in the vessels, is then (as a consequence of the vectorially averaged magnetization over the slice, which is represented in the image) the cause of reduced signal intensity. Fig. 5.27 gives an example of this. Thus, in principle, magnetic resonance imaging offers the possibility of noninvasive angiography for large vessels.

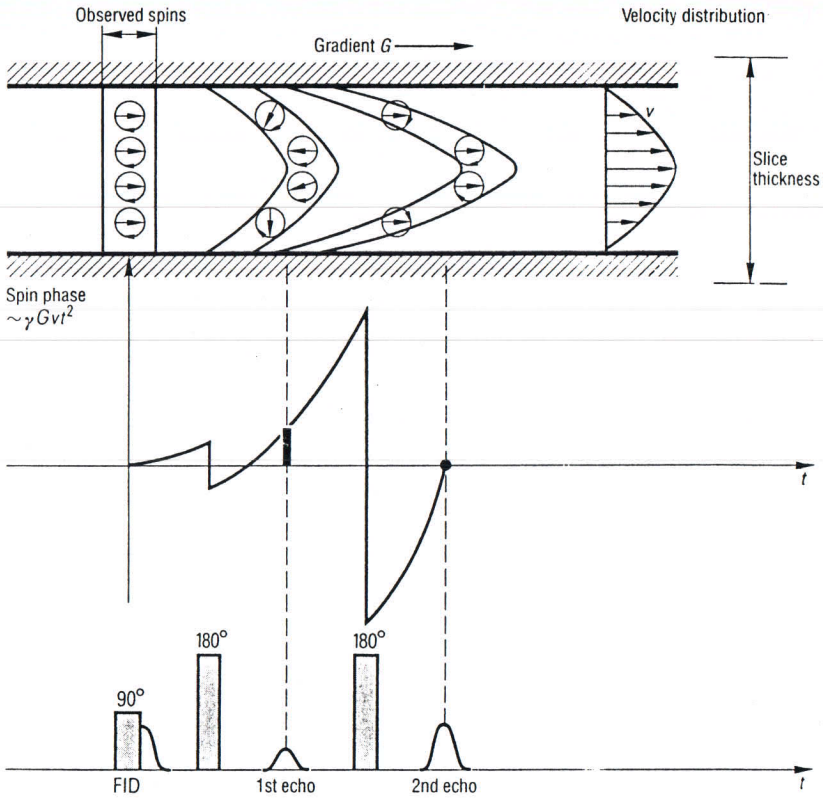

Fig. 5.26
Flow within the slice. As a consequence of the field gradient used in the imaging sequence the phase of the transverse magnetization varies over the slice in proportion to the velocity, so that in the first echo a reduced average signal results; in the second echo the phase shift has been compensated

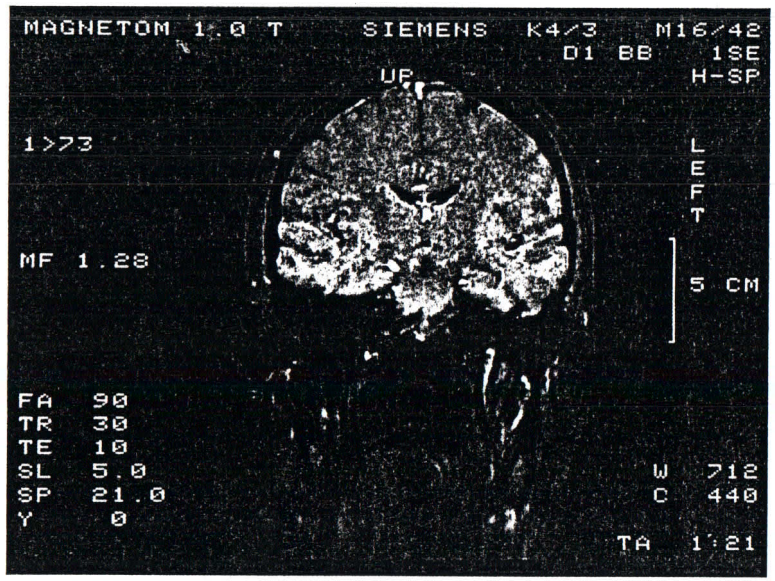

a)

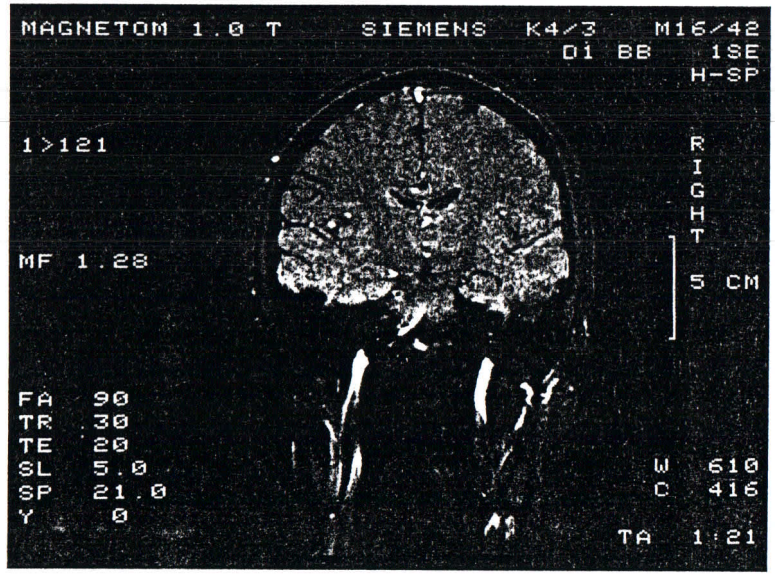

b)

Fig. 5.27
(a) Magnetic resonance tomogram from the first echo obtained from the area of the carotid arteries in a normal volunteer; the flow in the vessels appears dark.
(b) The corresponding image from the second echo, in which the carotid arteries appear bright; only where turbulent flow occurs is the signal intensity diminished

5.2.6 Spatially resolved spectroscopy

For the magnetization measurement described up to now, spatial resolution was obtained by relating the MR frequency to the position with the aid of magnetic field gradients. However, if one is interested in the spatial distribution of chemical shifts and spectral splitting, it is of course not permissible for an additional magnetic field to be acting during signal acquisition. Various procedures have been developed for spatially resolved spectroscopy, in which this requirement is fulfilled. Essentially they may be reduced to two principles, those pre-coding the magnetic resonance signal and those employing a volume-selective excitation.

Fig. 5.28 shows a pulse sequence for the first case, designated as 'chemical shift imaging' (CSI). Following a (generally non-selective) 90° pulse, a combination of magnetic field gradients G_x, G_y, G_z are switched on for a specified length of time and then the magnetic resonance signal is read out in the absence of any gradients. This signal is then given by

$$m_\perp(G_x t_x, G_y t_y, G_z t_z, t) = \int M_\perp(x, y, z, \omega)\, e^{-i\gamma(G_x x t_x + G_y y t_y + G_z z t_z + \omega t)}\, dx\, dy\, dz\, d\omega. \quad (5.62)$$

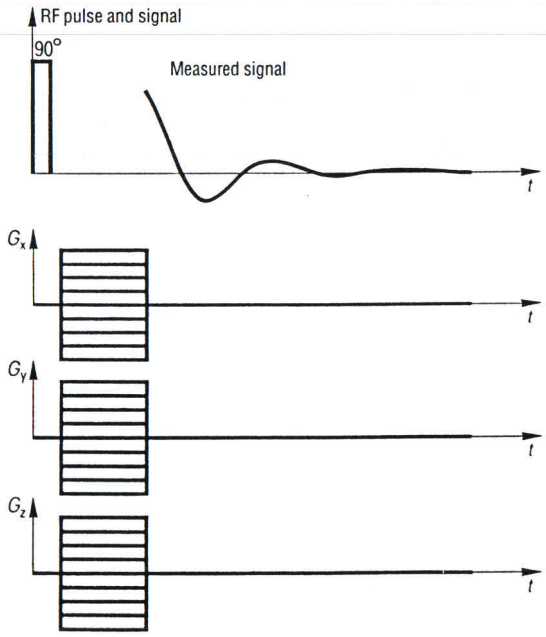

Fig. 5.28
Principle of the sequence for spectroscopic imaging: the magnetic resonance signal is coded by a combination of the three gradients G_x, G_y, G_z and then read out in the absence of a gradient

This sequence is repeated as often as necessary with other gradient combinations until the desired spatial resolution results in accordance with equations 5.58a and b. A four-dimensional Fourier transform of this set of signals then yields the desired spatial distribution of the resonance lines.

If a sample with a uniform resonance frequency is used, e.g. water, the procedure described yields the spatial distribution of the static magnetic field [5.20]. However, even a spatial resolution as coarse as that given by 16^3 image elements and a typical repetition time of 1 s would require a measuring period of over one hour. Instead of the non-selective RF excitation pulse, therefore, one generally uses a selective pulse and only determines the distribution of the resonance frequencies in a single slice. The pictorial representation of the data can be given in the form of a summed image, which shows the magnetization of all the spectral lines as a gray shade value; with this image it is possible to call up the desired spectrum of the labelled pixels by means of a cursor from the image evaluation console. A pictorial representation of the magnetization of a frequency component can, however, also be given; this would correspond, e.g. to the distribution of a chemical compound.

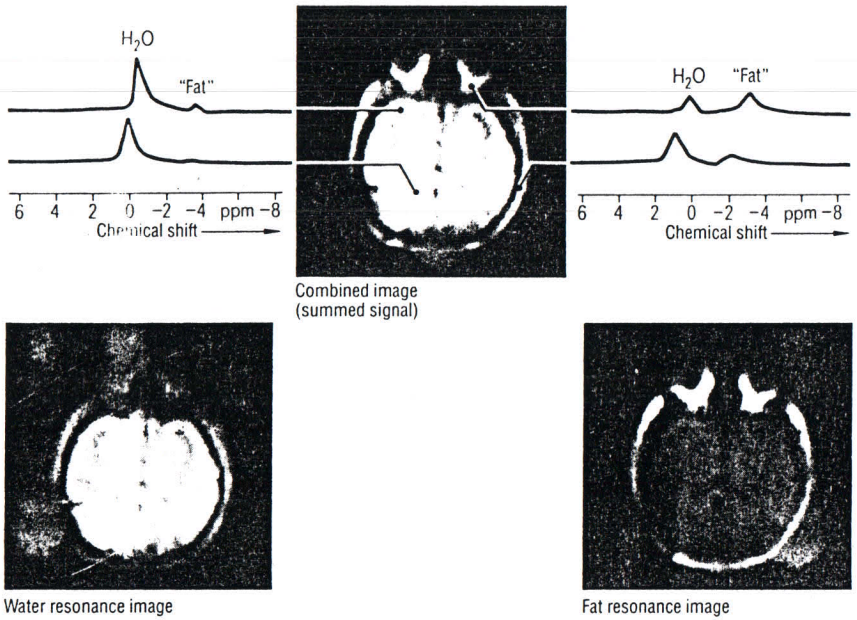

Fig. 5.29
Example (showing the human head) of spectroscopic imaging by means of protons. A 32 × 32 matrix was used in conjunction with selective excitation

For the magnetic resonance of hydrogen nuclei in the human body, however, nearly always only those two components which are due to lipids and to water are observed in the spectrum (Fig. 5.29). Given this information, lengthy measurements to gather data for a multidimensional Fourier transform are of course pointless.

A procedure has been described by Dixon [5.2] in which one specifically measures the fat and water distribution and where only twice the measuring time needed for a single image is required. In addition to the image obtained by the standard spin-echo sequence, a second image is constructed in which the 180° pulse is shifted relative to the half-way point between the 90° pulse and the middle of the measurement period. In this extra time interval, phase shifts build up between the spins (Fig. 5.30), which may be ascribed to different chemi-

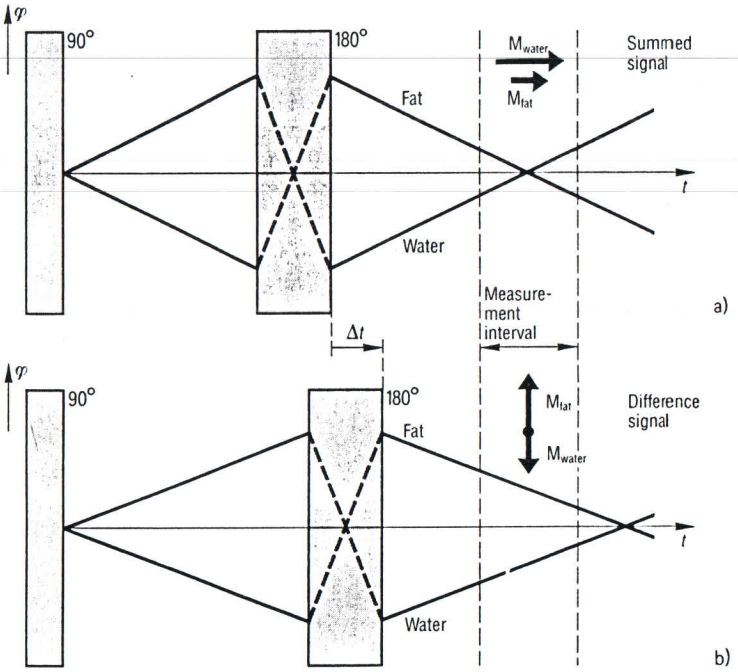

Fig. 5.30
Phase trajectory for the nuclear magnetization of fat and water using (a) a symmetrical and (b) an asymmetrical spin-echo sequence.
For the symmetrical sequence the sub-magnetizations are parallel and for the asymmetrical sequence they are antiparallel

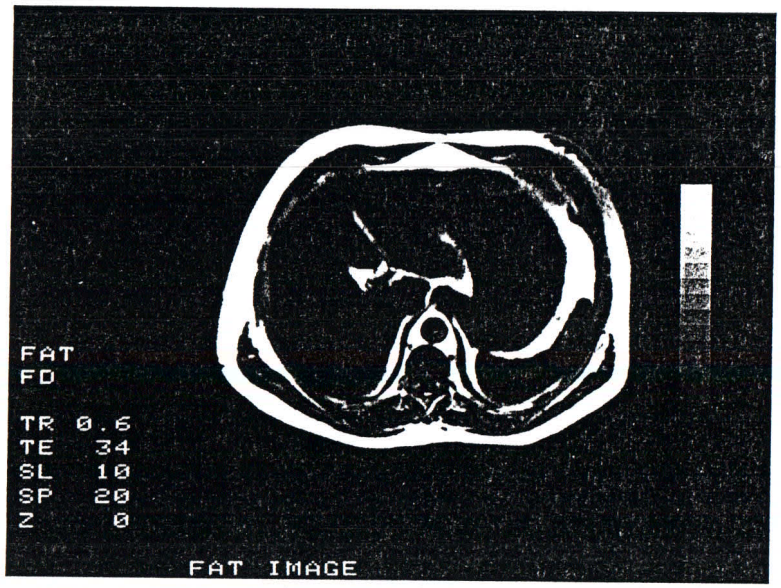

a)

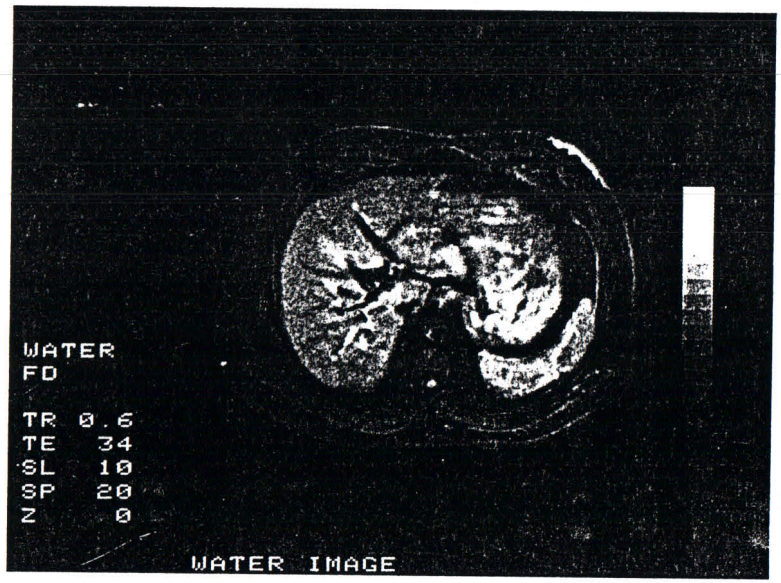

b)

Fig. 5.31
Calculated pure fat image (a) and pure water image (b) obtained using the Dixon sequence. To correct field inhomogeneities, a circular water phantom was employed, the contour of which can still be recognized in the images

cal shifts (but may also be due to static field inhomogeneities). If, in particular, a time shift of the echo is performed,

$$\Delta t = \frac{\pi}{\gamma \delta B_0}, \tag{5.63}$$

where

δ is the difference in the chemical shifts between fat and water

then at the time of signal readout, the magnetization of the lipids is antiparallel to that of the water. This means that by addition and subtraction of the image generated with the 'symmetric' echo, a pure fat and a pure water image may be calculated (Fig. 5.31).

It has already been mentioned that, for an asymmetrical 180° pulse, effects arise which are not only due to different chemical shifts but also to field inhomogeneities. For the condition given by equation (5.63), this means that the difference vector for the magnetizations of fat and water is locally rotated with respect to the sum vector, i.e. the pure fat and the pure water image can only be calculated if this angle is known. To obtain this angle, it is necessary to carry out a calibration measurement with a homogeneous phantom. The comparison of the 'image in phase' with the image 'out of phase' yields the distribution of the phases caused by field inhomogeneities.

Metabolites, e.g. lactate, occur in tissue only in a concentration 10000 times smaller than that of lipids or water. Detecting them by means of proton resonance therefore functions only if the strong water and fat signals are not excited or suppressed in the process. For this purpose, special pulse sequences [5.22] have been developed in analytical spectroscopy. In order to be able to use them selectively with regard to position, we can by way of example ensure by means of so-called selective saturation pulses that the magnetization is oriented only along the static magnetic field in the subvolume of interest and is otherwise distributed as randomly as possible in space (Fig. 5.32a); then the application of an arbitrary non-selective sequence only yields information from the previously selected subvolume.

One method of selective saturation consists in first rotating the whole magnetization into the transverse plane by means of a non-selective 90° pulse, and then, with a selective RF pulse in a magnetic gradient, rotating all the spins from one slice back again. The spins outside the slice remain in the transverse plane and dephase in the field gradient and then no longer yield a signal. Immediately repeating this sequence in the two other orthogonal gradients first selects a strip from the slice and then, from this, a cube (Fig. 5.32b).

As mentioned in Table 5.1, the detectability of heavy nuclei is about 1000 times smaller than that of protons. Field strengths substantially larger than 1 T are required in order to be able to resolve the spectral splitting. Detection is conse-

quently limited to relatively large volumes. Imaging with such nuclei requires very long measuring times and even then only gives very coarse spatial resolution and a poor signal-to-noise ratio. The best solution is to make use of surface coils, frequently in conjunction with an additional localization procedure.

Apart from the methods of selective excitation or selective saturation already briefly described, one procedure seems especially well suited to achieving additional localization. This procedure, 'rotating frame spectroscopy', does not require magnetic field gradients and only utilizes the radio-frequency field gradient of a surface coil [5.23, 5.24]. The problems associated with the rapid switching of magnetic fields, e.g. of eddy current compensation, are avoided by this method; the measurement can start immediately after the RF pulse without losing any signal due to transverse relaxation.

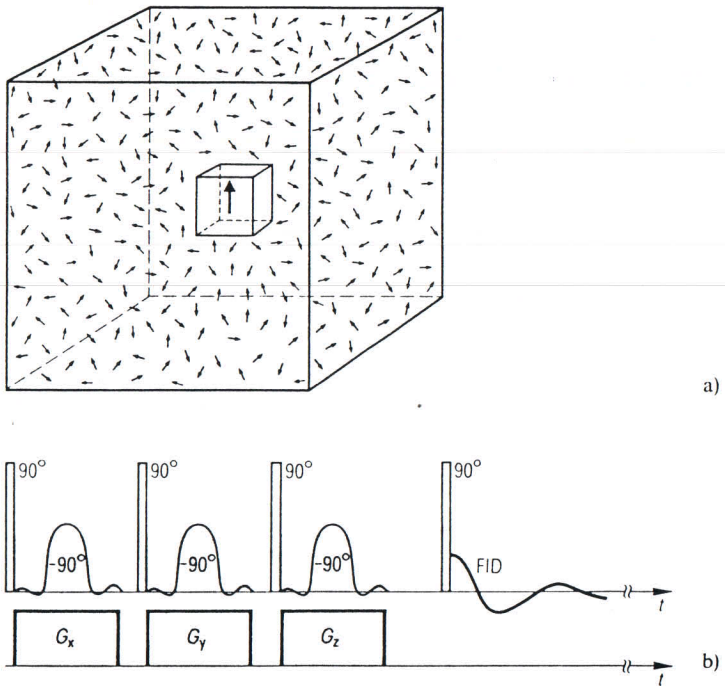

Fig. 5.32
(a) With selective saturation, the magnetization is dephased outside the subvolume ΔV of interest.
(b) Principle of the selective saturation sequence: With a non-selective 90° pulse, transverse magnetization is generated. In each case this dephases in the magnetic field gradient, while selective 90° pulses restore the equilibrium magnetization in the desired volume element. A final non-selective 90° pulse then reads out the magnetic resonance signal from this volume element only

If we transmit an RF pulse through a surface coil, nuclear spins in its vicinity are rotated away from the equilibrium orientation by a larger angle than distant ones. This is demonstrated in Fig. 5.33, in which the transverse magnetization of a phantom is depicted following excitation by means of a surface coil. For the shells with no signal

$$\sin \alpha = \gamma B_1(r)\, t = n\, 180° \; (n = 0 \ldots n_{max}), \tag{5.64}$$

where

B_1 is the RF field strength at position r and
t is the duration of the RF pulse.

With rotating frame spectroscopy, we detect nuclear magnetic resonance spectra on these shells: If r denotes the position of constant field strength $B_1(r)$ (given by the geometry of the surface coil), then the transverse component of the magnetic moment following an RF pulse is given by

$$m_\perp(\alpha, t) = \int m_\perp(r, \omega) \sin(\alpha(r))\, e^{-i\omega t}\, dr\, d\omega. \tag{5.65}$$

By varying the field strength or the length of the RF pulse successively, the two-dimensional Fourier transform of this set of signals described by equation (5.65) then gives the spectra on the shells characterized by equation (5.64).

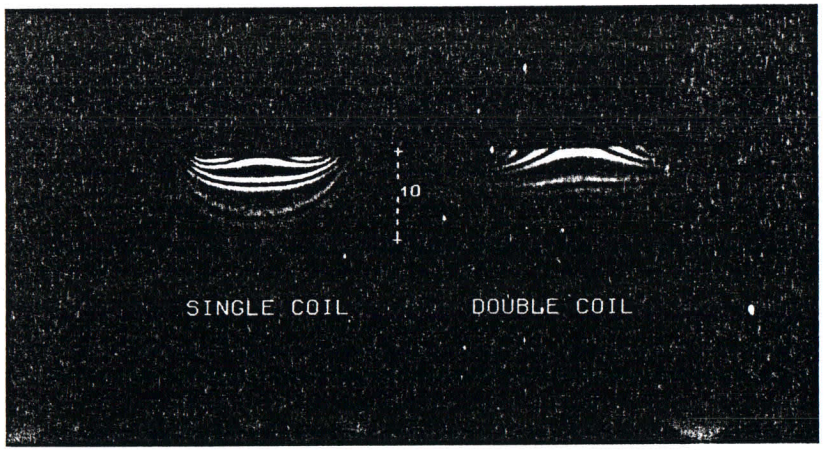

Fig. 5.33
(left) Distribution of the transverse magnetization beneath a single surface coil which has been subjected to a radio frequency pulse.
(right) Distribution of the detected transverse magnetization beneath a concentric double coil in which the outer coil was used for transmitting and the inner coil for receiving

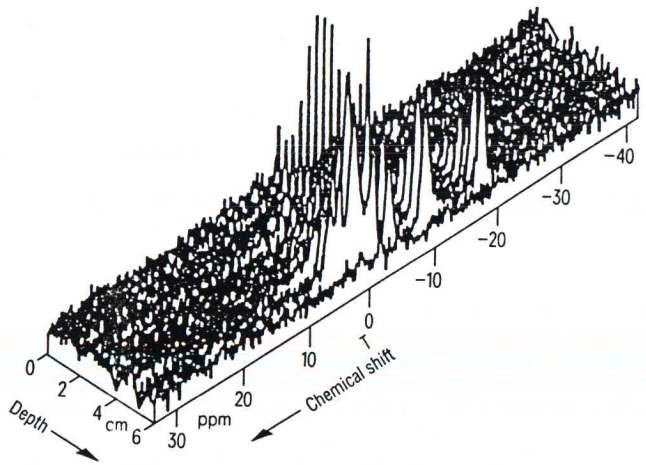

Fig. 5.34
Rotating frame spectrum of the human liver. The surface spectrum corresponds to a muscle spectrum, whereas the more deeply lying spectrum indicates the presence of sugar phosphates and phosphodiester, but no longer any phosphocreatine

When using single coils placed over the body, even the 'deepest' spectrum still contains information from the surface, because of the curvature of the shells. If concentric double coils are used, with the outer coil transmitting and the inner coil receiving, then the latter essentially cuts out parallel planes from the excited shells (Fig. 5.33b). An in-vivo phosphorus spectrum of the human liver, obtained by using a double coil and rotating frame spectroscopy, is shown in Fig. 5.34.

10 Magnetic resonance imaging

10.1 System Overview

A magnetic resonance imaging (MRI) system is similar to the type of processor-controlled Fourier NMR Spectrometer (NMR = Nuclear Magnetic Resonance) used routinely today in analytical chemistry for the determination of molecular structure. In addition to standard NMR components an MRI system has gradient field coils and the appropriate pulsed power supply for the spatial encoding of the magnetic resonance signal (MR signal), as well as monitors for image display. The system is also adapted to the size of a normal patient, and the control program is structured to meet imaging requirements.

Figure 10.1 shows the basic arrangement and interaction of the components of an MRI system. Important aspects of the construction and specifications for these components will be discussed in more detail in the following sections: Magnet with Shim Coil and Gradient Coil System, RF System, System Control and Patient Table, on which the patient – reclining on a cradle-shaped support – can be moved into the gantry of the scanning system.

The main magnet system (1) generates a magnetic field constant in time, in order to polarize the nuclei of the atoms of the patient's body. The necessary spatial homogeneity within the measurement volume is guaranteed by the shim coils (2) in the magnet bore and by iron plates mounted both inside and outside when necessary. The cylindrical gradient coil (3) is placed concentrically in the opening. It consists of three sets of windings, which generate a linear gradient field in the direction of the Cartesian coordinates (see Fig. 10.2) proportional to the superimposed current. Inside the gradient coil there is a radio-frequency (RF) coil or RF resonator (antenna, 4). The purpose of this antenna is to transform the RF pulse generated by a power transmitter into an alternating magnetic field to excite the spins in the tissue being examined. This antenna then picks up the alternating field generated by the excited spins and converts it into a voltage which is forwarded to the receiver.

After the pulse sequence controller has been supplied with appropriate control programs, it runs the measurement sequence for the most part independently of the system processor. It assures the correct timing of the gradients via digital-to-analog (DAC, 9) converters and an RF pulse with defined phase and amplitude via a modulator. The time base is the synthesizer which functions as a central clock. The control processor generates the conversion pulse for the analog-to-digital (ADC, 8) converters, which translate the low frequency demodulated MR signals into digital numbers which can be utilized by a computer.

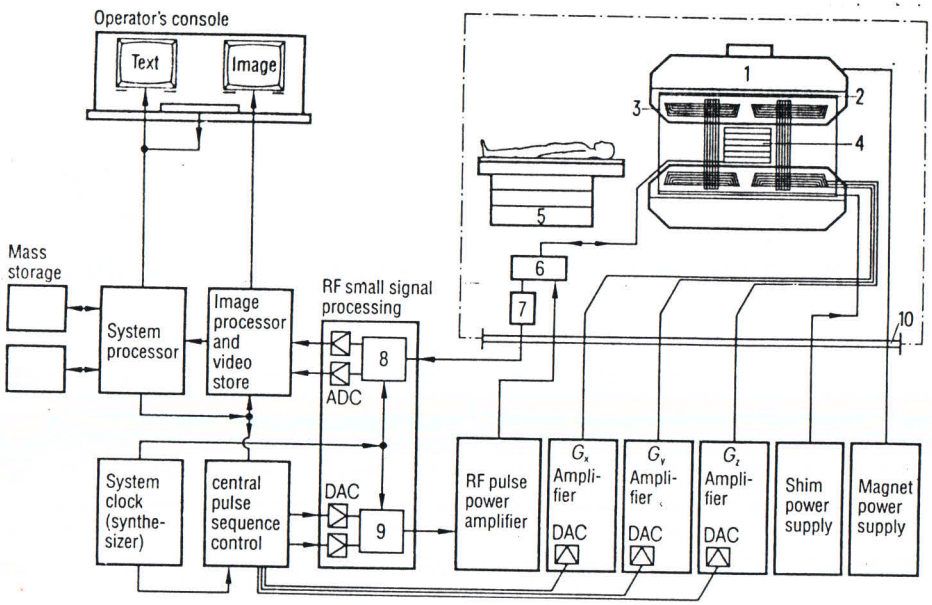

1 Magnet with cryo tank and cryogenic shielding
2 Shim coil system
3 Gradient coil system
4 RF resonator (antenna)
5 Patient table
6 Transmit-receive switch
7 Preamplifier
8 Quadrature demodulator with two low-frequency low-pass filters and ADC
9 SSB modulator with two DACs
10 RF-proof leadthroughs

Fig. 10.1 Schematic wiring diagram of an MRI scanning system

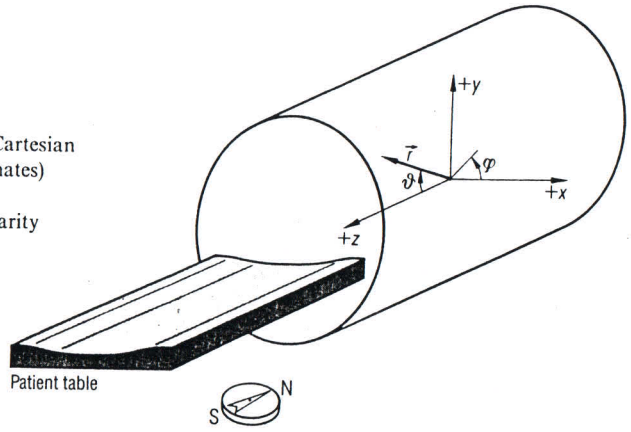

Fig. 10.2
Coordinate system (Cartesian and spherical coordinates) of the gradient coils; definition of field polarity

Measurement data are fed directly into the programmable image processor, which reconstructs them as image data immediately after data acquisition. Image data are copied to the video memory of the control console monitor.

The host computer manages the measurement data, image data and control programs. The video terminal serves as the interface between the host computer and the user.

10.2 System components

10.2.1 Magnet

Criteria for the selection of field strength

As has been shown in Section 5.1.8 the signal-to-noise-ratio (SNR) increases linearly with the main magnetic field B_0 (assuming a scanning object which generates RF losses, as is the case with a patient). This fact could lead to the assumption that the quality of an MRI system, expressed as the attainable SNR per volume element (and per square root of the invested measurement time), increases without limit with an increase in field strength. There are several practical and physical reasons, however, for not increasing the field strength to any arbitrary value, especially for systems used primarily for hydrogen imaging [10.1]. As will be discussed, the selection of field strength also has an important effect on the gradient and RF systems.

Considerations in regard to the technical implementation of these components are governing factors in the selection of field strength.

Those factors which must be taken into consideration are summarized in Table 10.1.

Chemical shift

The chemical shift is the main characteristic employed in NMR spectroscopy. The resonant frequency of the MR signal shifts slightly depending upon the type of chemical bond in which the nucleus of the material being examined occurs. This is caused by the diamagnetic shielding effect which the electron cloud within the molecule has on the nucleus and which is proportional to the main field B_0.

Due to their concentration in the human body, the hydrogen nuclei of free water (H_2O) and in aliphatic bonds (fat, $-CH_2-$) comprise essentially all protons visible in the MR image. Their relative resonance frequency difference δ is approximately 3 ppm, i.e. about 130 Hz at a field strength of 1 Tesla (T) (42.6 MHz). As explained in Section 5.2.3, spatial information is encoded in frequencies during readout in field gradients. Since the nuclei do not differentiate

Table 10.1 Factors to consider in selecting the field strength for ^{1}H MRI

Cause	Effect
Chemical shift	Image shift between fatty and aqueous tissue
Constant field inhomogeneity	Distortion
RF penetration characteristics (skin effect)	Inhomogeneity of intensity
RF losses	Patient warming
Field-dependent T_1 time	Change of contrast-to-noise ratio
Fringe field	Attraction of ferromagnetic objects, interference with cardiac pacemakers and other equipment

between outer and molecular fields, the result is a spatial shift between fat and water in the image (Fig. 10.3):

$$\delta x = \delta B_0 / G_x . \tag{10.1}$$

δx Spatial shift caused by chemical shift
G_x Readout gradient

In order to prevent spatial shifts from becoming too large, one must increase the readout gradient and therefore also the sampling bandwidth. Since noise

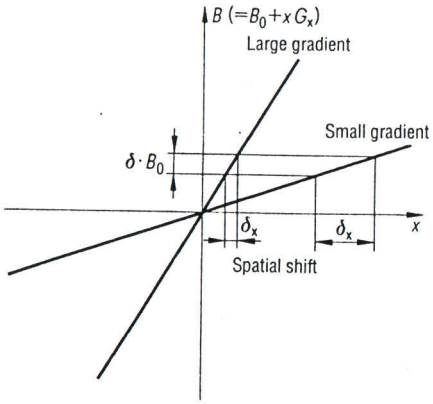

Fig. 10.3
Fat/water shifts as a function of the field gradient

increases with the square root of the bandwidth, however, a significant amount of the improvement in the SNR will be lost.

The same applies to selective slice excitation, i.e. the fat slice position is shifted with respect to the water slice position:

$$\delta z = \delta B_0 / G_z . \tag{10.2}$$

This requires an increase in the selection gradient G_z in proportion to the field. If the slice thickness, Δz, remains constant, the pulse bandwidth will increase, since:

$$\Delta \omega_p = \Delta z \gamma G_z . \tag{10.3}$$

As the bandwidth increases, the pulse duration becomes shorter, so that a higher RF field amplitude peak or pulse power becomes necessary.

Inhomogeneity of the constant magnetic field

The constant field inhomogeneity has an effect similar to a chemical shift. A field changed in relation to the nominal field strength by external influences acts on the nuclei. The result is a spatially-dependent dislocation of volume elements in the direction of the readout or slice selection gradients, which is calculated analogously to equation 10.1 and 10.2 by replacing the "chemical shift" with the relative field inhomogeneity.

$$\delta = (B(x, y, z) - B_0)/B_0 . \tag{10.4}$$

Since magnetic field inhomogeneities cannot be reduced at will, owing to the magnet's construction, undesirable distortions must be reduced by increasing the gradient strengths with the field strength. An additional undesirable effect is caused by the inhomogeneity of the field across a volume element. This results in a dispersion of the phases of the nuclear magnetization (T_2^* effect) and, therefore, in a signal loss.

Irregularities in the macroscopic magnetic susceptibility of the subject can also cause local distortions, which increase with field strength at constant gradient strength.

RF power loss in the subject under study

According to the Maxwell equations, there is always a proportional electric field linked to a given time derivative of the magnetic field [10.2].

$$\vec{\nabla} \times \vec{E} = \frac{\partial \vec{B}}{\partial t} \quad \text{or} \quad \oint \vec{E} \, d\vec{r} = \int_F \frac{\partial \vec{B}}{\partial t} \, d\vec{F} . \tag{10.5}$$

The electric field induces eddy currents with a current density of $\vec{j}$ in a conductive material. When B_1 is sine-shaped the eddy currents increase linearly with the frequency ω_0 due to the proportionality between E and $\frac{\partial B}{\partial t}$.

Disregarding the losses in the RF coil (resonator) and the minimal frequency dependence of the conductivity in the subject, the transmit power P required to generate a given B_1 field strength increases as the square of the nuclear resonance frequency, because:

$$P = \int_V \vec{j}\vec{E}\,\mathrm{d}V = \int_V \sigma E^2\,\mathrm{d}V. \tag{10.6}$$

Thus

$$P \sim \omega_0^2. \tag{10.7}$$

This increase in required RF power must be multiplied by the increase resulting from the pulse bandwidth, as shown in Equation (10.3). The RF output warms the patient like a diathermy unit. Since a patient's thermoregulation system may not be functioning properly, the regulatory agencies of some countries have established relatively low specific absorption rates (SAR) (the permissible levels of absorbed RF power per unit of body weight). The Food and Drug Administration in the USA, for example, recognizes the ANSI guidelines of 0.4 W/kg. Fig. 10.4 shows the experimentally determined pulse output per B_1^2 field for an average patient during transmission using a whole-body antenna as a function of the field strength, B_0. Coil loss is subtracted using the following equation:

$$P_{\text{sample}} = P_{\text{input}} - P_{\text{coil}} = P_{\text{input}}\left(1 - \frac{Q_1}{Q_0}\right). \tag{10.8}$$

Q_1/Q_0 = Loaded/unloaded Q

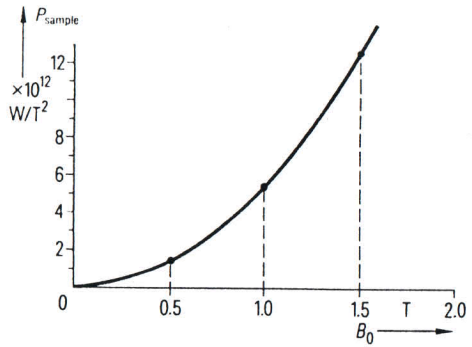

Fig. 10.4
Pulse power, P_{sample}, required per B_1 field squared for a given field strength B_0. (B_1 field – circular component – for a linearly polarized resonator; average patient weight approx. 70 kg)

There are limitations for the sequence repetition time at fields of 1.5 Tesla or greater for spin-echo sequences with two 180° pulses of approximately 1 ms duration. In this case, the sequence repetition time is no longer limited by the capabilities of the measurement system, but by the SAR.

RF penetration characteristics

The eddy currents induced by the RF field themselves generate an opposing field which weakens the applied RF field. This so-called skin effect [10.3] causes a spatially inhomogeneous excitation of the nuclear spins. RF field penetration decreases as the frequency, or conductivity, increases. At frequencies higher than approximately 40 MHz, shading of varying degrees, depending on the shape of the body being examined, may become visible.

Field dependence of the T_1 relaxation

The increase in the T_1 relaxation time with an increase in field strength [10.4] causes the relative saturation of the nuclear magnetization to increase with the field strength when the repetition time, T_r, remains constant. Consequently the increase in the SNR is less than proportional to the field strength, B_0 (Fig. 10.5).

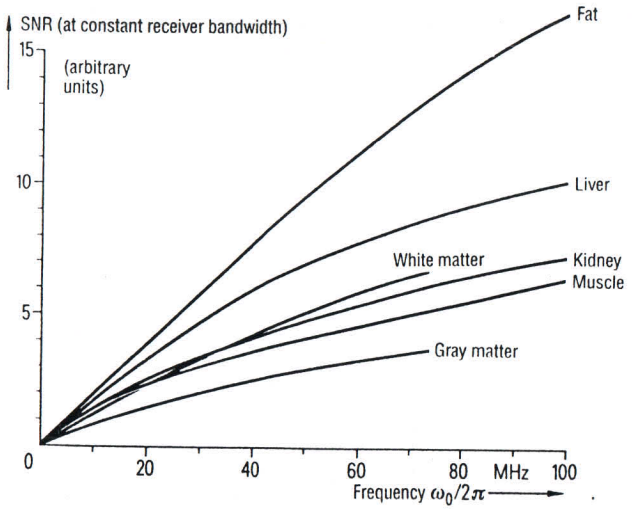

Fig. 10.5
Increase in the SNR with field strength, taking into consideration the dependence of the T_1 relaxation time on the field strength B_0 for a constant repetition time T_r

Safety considerations

It is obvious that the operation of large magnets with high field strengths is not possible without considering safety problems. The stored field energy increases with the square of the field strength. It must be possible to dissipate this energy quickly in an emergency (quench for superconducting magnets).

Large fields exert a substantial force on ferromagnetic objects, such as oxygen tanks, fire extinguishers, transport machinery or tools inadvertently brought near the magnet. If these objects are magnetically saturated – whether this occurs depends strongly on the material, shape and orientation of the object – the forces increase linearly with the fringe field. For unsaturated objects, the increase in the force is quadratic. In order to avoid accidents, ferromagnetic objects must be kept at a safe distance from the magnetic resonance equipment.

Patients with cardiac pacemakers or other electronic implants may not enter an area having a fringe field strength greater than 0.5 mT without medical supervision. The so-called pacemaker zone becomes larger with increasing field strength. Table 10.2 shows the distance of the 0.5 mT line from magnets of the same size, but for field strengths of 0.5 to 2.0 T.

Installation problems

There are several types of medical equipment in a physician's practice which are sensitive to static magnetic fields (see Table 10.3) and which cannot be set up in close proximity to a magnetic resonance scanning system. The selected field strength therefore has a direct effect on the amount of space required for an MR system and thus on installation costs, including any system shielding which might be necessary.

A consideration of the above mentioned points makes clear that there is no well defined optimum for field strength in an MR system. Along with the desire for high image quality and short exposure times, there is the important question of expenditure for the system itself and its operation. As will be shown in greater detail later in this chapter, the technological requirements increase at

Table 10.2
Safe distance for cardiac pacemaker wearers (for magnets having a 1.05 m bore and a length of 2.30 m without shielding)

B_0	0.5 mT line (radial)	0.5 mT line (axial)
0.5 T	6.5 m	8.3 m
1.0 T	8.2 m	10.5 m
1.5 T	9.4 m	12.0 m
2.0 T	10.3 m	13.1 m

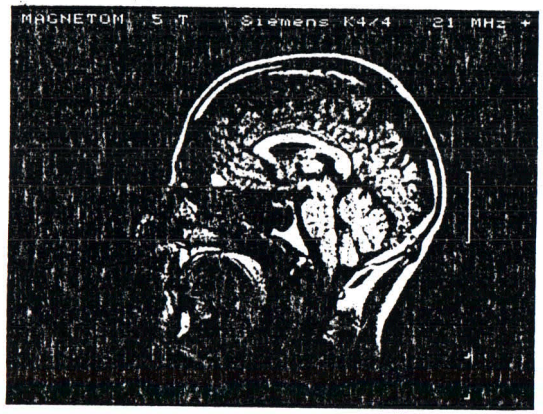

Fig. 10.6
Comparison of magnetic resonance image quality of cranial images at field strengths of

a) 0.5 T

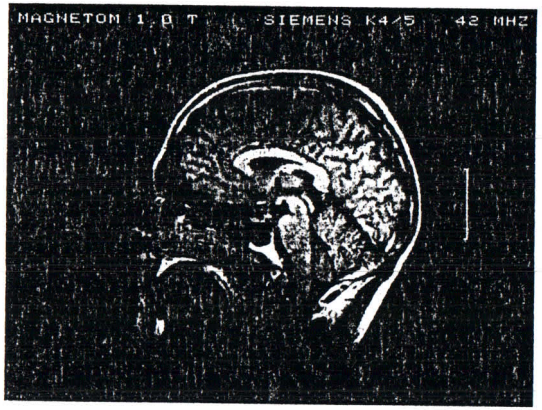

b) 1.0 T

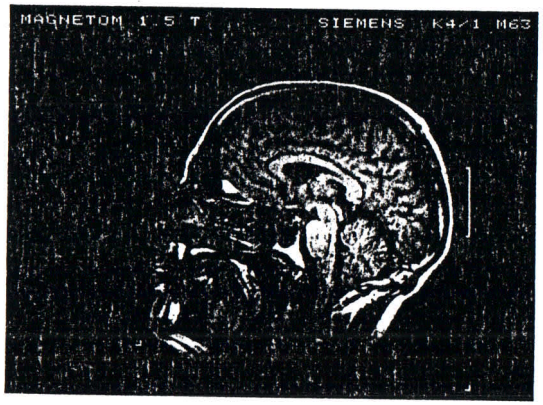

c) 1.5 T

Magnetic disks or tapes	3 mT
Video monitors with shielding or correction	3 mT
Video monitors (monochromatic)	1 mT
Cardiac pacemakers	0.5 mT
X-ray units	0.2 mT
Image intensifiers	50 μT
Photomultipliers	50 μT
Earth's magnetic field for comparison	50 μT

Table 10.3
Sensitivity of different systems to (static) magnetic fields

field strengths above 1 T without a corresponding increase in image quality or decrease in examination time per patient.

Since spatial and contrast resolution in MR imaging can be obtained by increasing the measurement time, systems with relatively low field strengths can be useful if purchase and operation costs are low enough to compensate for reduced patient throughput.

Figure 10.6 shows three cranial images taken at three different field strengths, but with otherwise identical parameters, including the bandwidth per pixel. The image quality (SNR) is clearly better from 0.5 T to 1.0 T, but the improvement is not as striking from 1.0 T to 1.5 T.

It should be noted that magnetic resonance imaging or spectroscopy on a living subject with nuclei other than hydrogen (sodium, phosphorus or fluorine, for example) is, for reasons of sensitivity, nearly impossible at field strengths of less than 1.5 T.

Types of magnets

Permanent magnets, resistive electromagnets and superconducting magnets are all used in analytical magnetic resonance spectroscopy as well as in medical magnetic resonance imaging. Either the air-core or the iron yoke construction is used for resistive electromagnets. Figure 10.7 shows the construction of several types of magnets. Table 10.4 summarizes the characteristics of the various types. The most important will be discussed further in the following.

In addition to field strength, other particularly important characteristics in magnetic resonance imaging are field stability, especially short-term stability ranging from milliseconds to several seconds, and the degree of homogeneity which can be achieved by shimming procedures within the measurement volume, which is almost always spherical in shape and which should be at least 40 cm, or preferably 50 cm, in diameter.

Field strength

The attainable field strength in the effective volume of a permanent magnet is determined by the required field energy produced there in relation to the energy stored in the permanent magnetic material. In consideration of the relatively large air gaps involved, such a magnet then requires either an extremely large amount of fairly inexpensive material or a smaller amount of very expensive material having a high magnetic remanence. The limitation in resistive magnets, on the other hand, is caused by the required electrical power. In both cases the maximum field strength is approximately 0.3 T.

Superconducting magnets with an inner bore of approximately 1 m can be constructed with field strengths of up to 4 T. Its limits are defined by the fact that current carrying capacity decreases as the field of the superconductor increases and also by the forces generated.

Homogeneity

A large homogeneous image volume requires a correspondingly large main magnetic coil, i.e. a large permanent magnet. Since power requirements in a typical clinical installation should not exceed 100 kW, more volume in a resistive magnet can only be achieved by sacrificing field strength. The homogeneous volume in superconductive magnets can be influenced by the length of the magnet and can therefore be adapted to requirements relatively easily.

Field stability

The Fourier MRI procedure requires an extremely stable main magnetic field over time in order to generate images free of artifacts. The reason for this

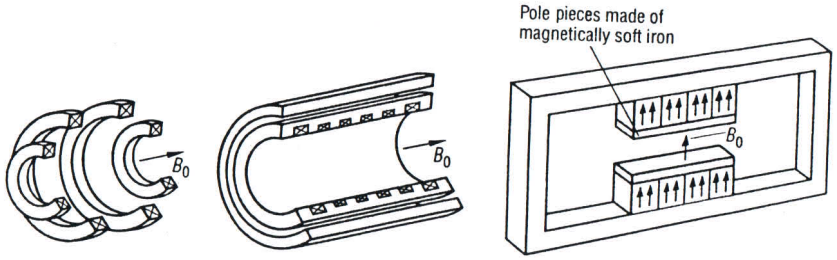

a) resistive magnet (air coil)
b) superconducting magnet
c) permanent magnet (yoke type)

Fig. 10.7 Construction of various types of magnets

Table 10.4
Comparison of magnet types for MRI Systems

	Superconductor	Resistive	Permanent Magnet
1. Technical characteristics			
Field strength	very high field possible (to 4 T)	relatively small to 0.3 T	to 0.3 T
Effective volume and typical homogenity	large 15 ppm/50 cm dia.	sufficient 40 ppm/40 cm diam.	sufficient 40 ppm/40 cm diam.
Field stability	very good	moderate, dependent upon power supply 0.3 to 1 ppm	very good
Shielding of external interfering fields	significant	extensive shielding with iron yoke; no shielding without iron yoke	good shielding
Eddy currents due to pulsed gradients	Extensive compensating measures needed	very limited (feedback to power supply)	very limited anisotropic
Field orientation	Z	Z (or Y)	Y
Fringe field	very large	small (due to small B_0)	negligible
Emergency shutdown	relatively slow due to quench	can be shut down immediately (small L/R)	cannot be shut down
Dimensions	large: 1.8 m diam. × 2 m	average: 1.5 m diam. × 1.6 m	very large: 4.2 m × 2.5 m × 2.3 m
Mass	average: 6 t	relatively low: 2 t	very large (yoke type) 80 t
2. Costs			
Initial price	high	low	high
Energy usage	none	very high to 100 kW ($\sim B_0^2$)	none
Cooling	Cryogens 0.5 l liquid helium per hour	large amount of cooling water needed	none

is that the spatial information is encoded in the phase of the signal generated by the volume elements to be imaged. Simulations show that phase errors as small as approximately 3° can generate visible artifacts. In the simplest of MR experiments, the FID, the phase errors $\Delta\varphi$ caused by time varying field shifts, $\Delta B_0(t)$, accumulate up to the read-out time, t, to:

$$\Delta\varphi = \gamma \int_0^t \Delta B_0(t')\,\mathrm{d}t' \tag{10.9}$$

$t=0$ represents the time of the excitation pulse. The equation for a spin echo experiment is as follows:

$$\Delta\varphi = \gamma\left[\int_{T_e/2}^{t} \Delta B_0(t')\,\mathrm{d}t' - \int_0^{T_e/2} \Delta B_0(t')\,\mathrm{d}t'\right] \tag{10.10}$$

where $T_e/2$ is the time between the 90° and 180° pulse. The phase error, $\Delta\varphi$ can be calculated for a sinusoidal field modulation of frequency ω_b and phase φ_b. Other time characteristics can be described as a Fourier synthesis of sinusoidal modulations. For:

$$\Delta B_0(t) = \Delta B_0 \sin(\omega_b t + \varphi_b) \tag{10.11}$$

the following expression results:

$$\Delta\varphi = -\frac{1}{\omega_b}\gamma\Delta B_0[\cos(\omega_b t + \varphi_b) - \cos\varphi_b]. \tag{10.12}$$

At very low $\omega_b\left(\omega_b \ll \frac{\pi}{t}\right)$ and an unfavorable phase angle, $\varphi_b = \frac{\pi}{2}$, the following relation applies:

$$\Delta\varphi(t) \approx \gamma\Delta B_0 t. \tag{10.13}$$

Otherwise, the phase error decreases as the reciprocal of the interfering frequency:

$$\Delta\varphi_{max} \leq \frac{1}{\omega_b}\gamma\Delta B_0. \tag{10.14}$$

At $t=5$ ms, for example, this gives: $\Delta B_0 < 0.04$ μT. The amplitude of a 60 Hz ripple field should be less than 0.06 μT. These requirements demand a current

stability of less than 0.2 ppm, a condition technically difficult to achieve for a resistive magnet. In contrast, superconducting magnets, which are short-circuit operated, and permanent magnets are absolutely stable with respect to measurement time for an MR image. Superconducting magnets also shield very effectively against external interfering fields. Experience shows that an external interference field strength of up to 0.6 μT can be tolerated for the above frequency range without affecting image quality.

A consideration of all the advantages and disadvantages, including those pertaining to image quality and operating costs, leads to the conclusion that superconducting magnets are to be preferred for magnetic resonance imaging. All major manufacturers therefore employ this type of magnet almost exclusively.

Superconducting magnets

The following is a discussion of the technical considerations important to the construction and operation of large superconducting (SC) magnets in magnetic resonance imaging. For further information on construction of the magnets, the physics of superconductivity and producing the extremely low temperatures required refer to the relevant publications [10.5].

The characteristic parameters of an SC magnet are the maximum possible field strength, field homogeneity across a given volume generally spherical in shape and the consumption rates for cryogens, especially liquid helium, which is relatively expensive.

Field strength and homogeneity

The current carrying capacity of the wire material must be taken into consideration when constructing a magnet. It must be superconductive at the temperature of liquid helium, i.e. the critical temperature at which the wire in a magnetic field becomes resistive must be appreciably higher than 4.2 K, the boiling temperature of helium at atmospheric pressure. A suitable material is a multifilament wire composed of 30 niobium-titanium strands of 0.1 mm diameter, each of which, for reasons of stability, is embedded in a copper matrix having a diameter of approximately 2 mm. Such a wire can carry currents of up to 500 A. The desired field strength determines the number of windings on a core of pre-determined length. A 2 T magnet comprises wire lengths of approximately 60 km and has an average radius of 650 mm. The winding is divided into 6 subcoils and the number of windings on each is calculated so that the field is optimally homogeneous at the central spherical volume of 50 cm diameter. Without external interference or assembly tolerances, which are unavoidable, such a field coil would exhibit an inhomogeneity of less than 5 ppm within

a spherical volume of 50 cm diameter. In practice, this figure is only approximately 100 ppm, even in environments which are nearly free of iron, so that additional shimming procedures are required (see section on shimming).

Cryostat

The required thermal insulation for the coils can be calculated using the allowable rate of evaporation, (V/t), the surface area of the helium tank, $F(\approx 26\ m^2)$, the specific evaporation energy, $E_M = 21$ kWs/kg and the density, $\varrho_{He} = 0.1$ kg/l of helium as follows:

$$R_T = \frac{\Delta T \cdot F}{\frac{V}{t} \cdot E_M \cdot \varrho_{He}}. \qquad (10.15)$$

If an evaporation rate of less than 0.5 l/h is required for the liquid helium, the surface-specific thermal resistance must be $R_T > 2 \cdot 10^4\ Km^2/W$. Figure 10.8 shows a cross section of the cryostat for a superconducting magnet. The figure illustrates the individual measures taken to insure such low heat transfer.

Care must be taken to prevent convection, as well any kind of thermal radiation, from penetrating to the helium tank, which contains the steel cylinder with the superconducting coils. The latter is accomplished by a radiation shield and superinsulating foil and the former by evacuating the entire magnet container to high vacuum. The components of a cryostat are suspended within each other on thin, extremely strong, fiberglass-reinforced plastic rods with low thermal conductivity. At the top of the cryostat there is a so-called service

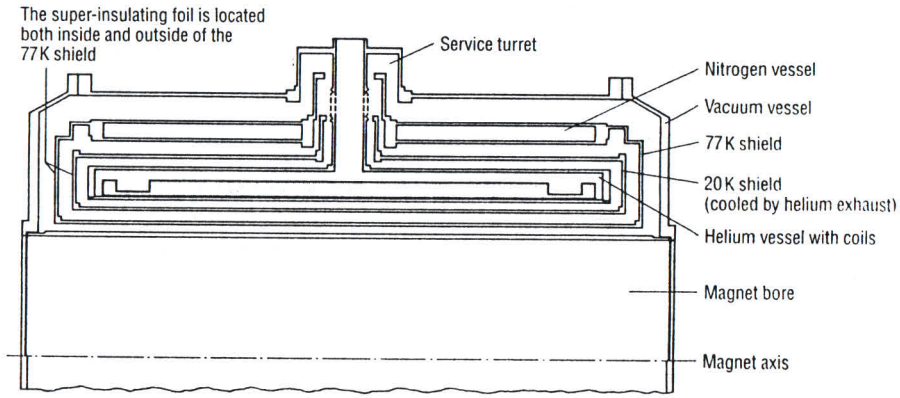

Fig. 10.8
Construction of the cryostat for a superconducting magnet (longitudinal cross section)

turret with openings to allow cryogens (N_2 and He) to be refilled and for the attachment of power cables. The evaporation of cryogens can be reduced to a reasonable level through using shield cooling machines (so-called refrigerators).

Loading and quenching

When the magnetic coil has been properly cooled and has reached the temperature of the helium it becomes superconductive and the field can be ramped up by connecting the coil to a power supply. This is illustrated in the circuit diagram shown in Fig. 10.9. In the quiescent state, switch S_L is at helium temperature and therefore represents the ideal short circuit. An electrical heater is used to warm S_L above the critical temperature, at which it takes on the resistance R_S, i.e. poorly conductive in comparison to the SC coil; the current superimposed by the magnet PSU begins to flow through the field coil. The rate of increase is determined by the voltage (U) generated by the power supply and the inductance of the magnet:

$$U = L\frac{dI}{dt}. \tag{10.16}$$

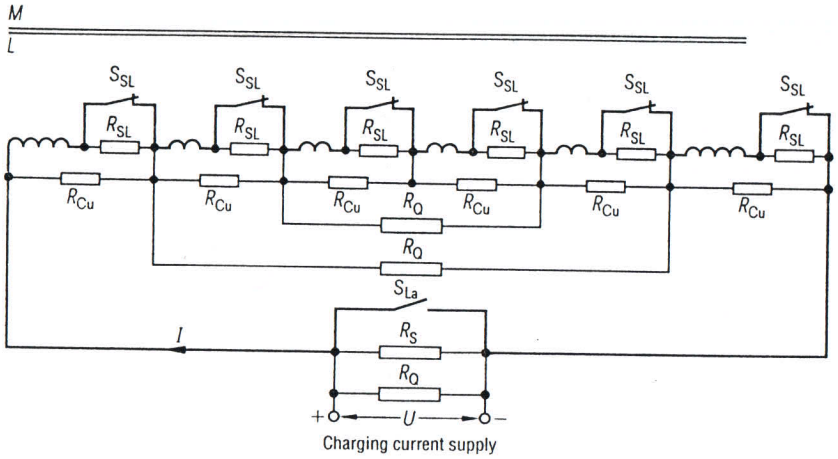

M	Inductive coupling between the coils	R_{Cu}	Distributed ohmic resistance of the copper matrix
L	Winding inductance	R_Q	Quench protection resistors
S_{SL}	Switch closed during SC state	R_S	SL switch resistor S_{La} – open
S_{LA}	SL switch (open during ramping)		
R_{SL}	Distributed ohmic resistance of the SC		

Fig. 10.9 Equivalent circuit diagram of an SC magnet with six coils

When the preselected current level or field has been established, the current regulator decreases the voltage to zero and S_L is closed by switching the heater off. The power supply system may then be removed; recharging is not necessary.

Controlled discharging of the stored field energy (for a 2T magnet with an inner bore of 1 m approximately 7 MWs) is performed by reversing the energizing procedure, i.e. the power supply superimposes the current that was set before the S_L switch is opened. A negative voltage is then applied until the current is reduced to zero.

A quench is understood to be the loss of superconductivity, either spontaneous or through external influences. In case of emergency, electrical heating elements increase the temperature of the coil windings beyond the critical point, thus precipitating a quench. Otherwise a quench is most often caused by negligence or the improper handling of the magnet, e.g. allowing the liquid helium level to drop too low.

The rate of current reduction is determined by the resistivity in the resistive zone of each coil winding, as well as their self inductance and mutual inductance. Since the resistive state spreads through the wire at finite speed, the values of these resistors are time dependent. In order to limit voltages, the so-called quench protection resistors are connected in parallel to the windings, giving the induced current a low resistance alternate path (see Fig. 10.9).

The total field energy is converted to heat in both the resistors and coils, which causes the liquid helium to boil off. A quench, especially at high field strength, is therefore highly undesirable and very expensive. In addition, the helium containers and the vacuum tank are subjected to great mechanical stress, due to the increase in pressure and eddy currents during a quench.

Fringe field shielding

If the space available for the installation of an MR system is limited, it is necessary to provide adequate shielding from the magnet's fringe field. Only ferromagnetic materials are suitable as shielding for static magnetic fields.

One differentiates between room shielding, such as iron plates in the walls of the examination room [10.6], and shielding mounted directly on the magnet, so-called self-shielding.

A considerable mass of iron is necessary for effective shielding, because the efficiency of the shielding is lost if the levels of magnetization rise above saturation inductance levels. One may assume that the same iron mass is required for comparable shielding effects in either room or self-shielding; although the thickness of the shielding material required is less at greater distances from the magnet, the total surface area to be shielded is larger. Highly permeable

materials, such as Permalloy, are not suitable since they do not exhibit high saturation inductance and are too expensive.

Shielding measures have a substantial effect on the field homogeneity of the measurement volume. The tighter and more eccentric the distribution of ferromagnetic material is, the more difficult it is to compensate for field distortions. Room shielding is generally dependent on conditions in the building and is seldom positioned symmetrically around the magnet. Self-shielding, on the other hand, is highly symmetrical and provides for minimal fringe fields relatively close to the magnet. The major disadvantage of self-shielding is the loading capacity required of the floor at the installation site. Figure 10.10 shows a 1 Tesla magnet in a 21 t self-shield. In comparison to an unshielded magnet (see Table 10.2) the 0.5 mT limit lies at 4.3 m in the radial and at 6.5 m in the axial direction.

Instead of complete shielding, it is sometimes sufficient to use a single iron plate as partial shielding in order to shield an adjoining room, for example, from the pacemaker control area.

Recently, so called actively shielded magnets have been developed. In these magnets the fringe field is reduced via an opposing, external, current-carrying winding. The active shield is integrated into the cryostat; this increases the size and cost of such a magnet considerably. Such magnets are constructed so that the dipole field (decreasing with the cube of the distance) is almost fully suppressed and only a quadrupole field (decreasing with the fifth power of the distance) remains. The advantage of an actively shielded SC magnet is its relatively low total weight compared with an iron-shielded magnet for the same fringe field distribution.

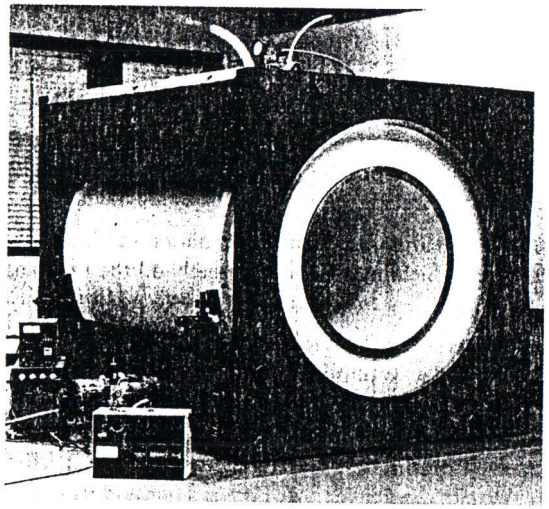

Fig. 10.10
1 T magnet with a 21 ton self shield

Shimming

Shimming is the elimination of constant field inhomogeneities originating from environmental influences and manufacturing imperfections.

The following technique is generally adopted: The field is measured using an MR probe on the surface of the spherical homogeneity volume, with expansion of the field according to spherical harmonics, followed by the determination of the expansion coefficients from measurement data and setting the corresponding currents for the shim coils, for which the windings are configured in such a manner that each generates a correction field closely approximating one expansion coefficient. Shimming is also possible by lining the bore surface or the external surface of the magnet with a suitable combination of iron plates.

Expansion by spherical harmonics

The characteristics of the magnetic field can be described by the Laplace equation:

$$\vec{\nabla}^2 \cdot (B_x, B_y, B_z) = 0. \tag{10.17}$$

As long as the field is sufficiently homogeneous, the field magnitude most important for the magnetic resonance frequency is equal to the field component $B_z = B_0$. The following spherical harmonic expansion is a solution of the Laplace equation in spherical coordinates, taking the center of the magnet as the origin:

$$B_0(r, \vartheta, \varphi) = \sum_{n=0}^{N} \sum_{m=0}^{M \le N} \frac{r^n}{R^n} P_n^m(\cos \vartheta)[A_n^m \cos m\varphi + B_n^m \sin m\varphi]. \tag{10.18}$$

The coordinate system is illustrated in Fig. 10.2. The functions P_n^m are designated associated Legendre polynomials of the nth degree and mth order [10.7]. The coefficients A_n^m and B_n^m comprise the so-called spectrum of the spherical harmonic expansion. They are expressed either as absolute field units (in T) or as relative field deviations $(B(\vec{r}) - B_0/B_0$ (in ppm), each normalized to the radius R. The purpose of the spherical harmonics expansion is the evaluation of the spectrum from the field measurements across the surface of the sphere with radius R (analysis). Using the coefficients, the reverse is also possible; that is, calculation of the field at any point within the sphere (synthesis).

A simple interpretation of the expansion in spherical harmonics is possible for the special case of $m = 0$:

$$B_0(r, \vartheta) = \sum_{n=0}^{N} \frac{r^n}{R^n} P_n(\cos \vartheta) A_n^0. \tag{10.19}$$

On the surface of the sphere the field is not dependent upon the angle φ. The coefficients A_n^0 are also called zonal terms, while terms in which m is not equal to 0 are called tesseral terms. The P_n functions are Legendre polynomials of the nth degree. P_0 is the constant 1, so that the A_0^0 coefficient can be interpreted as the strength of the constant field without any perturbations and all other terms as perturbations. P_1 describes a linear change in the field in the z direction. A_1^0 is then the z gradient. The tesseral coefficients A_1^1 and B_1^1 correspond to the linear gradients in the x and y directions.

The factors $(r/R)^n$ show that for small radii substantial field perturbations are generated only by terms of low degree, while perturbations of higher degree are only effective at the edges of the spherical volume. The magnitudes of the coefficients decrease with increasing degree. For this reason, the expansion can be terminated beyond a certain degree.

Measurement and determination of shim coefficients

In order to calculate the spectral term of the nth degree and the mth order from measurement values, the field must be measured to $n+1$ circles parallel to the xy plane at $2m$ points. The sampling points are equidistant in ϑ and φ, i.e. the distances from the circles to the origin are on the order of $R\cos\varphi$. Field measurement is performed by using a small MR probe attached to a positioning gear, which allows the coordinates $r=R\sin\vartheta$ and $z=R\cos\vartheta$ to be adjusted. The field spectrum is calculated from the values acquired at the points of measurement.

Shimming with correction coils

Current-carrying windings are arranged on a cylindrical tube inside the magnet bore. The windings are configured so that the field of each partial winding corresponds exactly to one coefficient of the spherical harmonics expansion. Figure 10.11 shows the arrangement of the twelve windings for the terms which are usually compensated electrically. The cylindrical windings correspond to the zonal and saddle-shaped configuration of the tesseral coefficients. The higher the degree and order, the more complex and less effective the coil set becomes. The orthogonality of the spherical harmonics expansion corresponds to coil sets which are almost completely decoupled both from the SC coil and from each other. The linear gradients may not be activated on the shim coil, since they couple strongly with the pulsed gradients. They can therefore be eliminated and are compensated by offset currents from the pulsed gradient coil. The winding geometry of the coils determines the (non-linear) gradients generated per current unit. This value can also be determined experimentally: The spectrum of the magnet without shimming current and with a defined current level applied to one coil set is determined as described. The difference calculated from the two coefficient spectra should, ideally, have only one coefficient. This

coefficient divided by the current results in the calibration factor for the corresponding shim coil. If all the factors are known, the magnet can be shimmed by setting the coil currents via a precision power supply.

Shimming with iron

One can also compensate for field inhomogeneity by mounting iron plates in the magnet bore or on the outside of the cryostat [10.8]. For each standard plate position one can determine, either by calculation or experiment, the field spectrum generated. The field spectra, of course, do not contain only one coefficient. It is practical that each position be located on a fixed grid. At such high field strengths, the iron plates are fully saturated, so that n number of plates will cause n times as much interference. Through varying the linear combi-

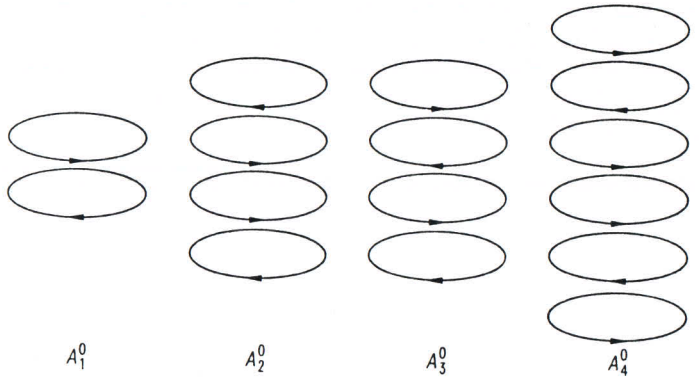

a) Zonal windings

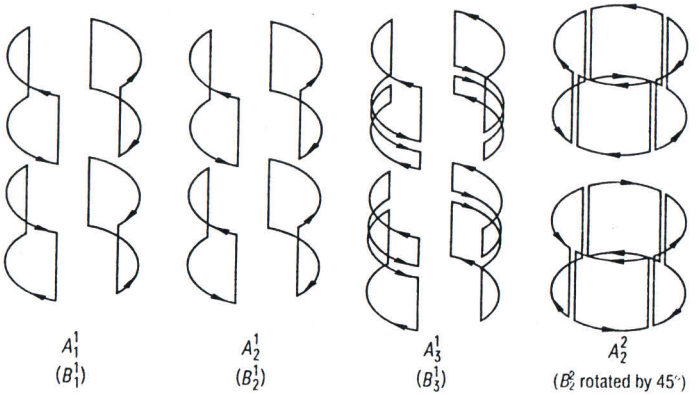

b) Tesseral windings

Fig. 10.11 Schematic drawing of shim coil windings

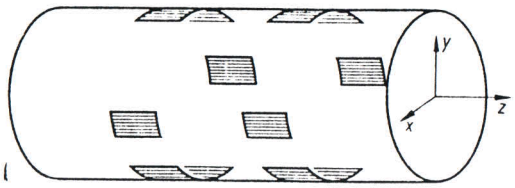

Fig. 10.12
Positioning of iron plates (passive shim) of the A_4^4 Term

nation of the different spectra corresponding to the various positions of the iron plates, one can establish a plate geometry that will compensate for the inhomogeneity of the magnet. This procedure can also be used with a magnet that is already electrically pre-shimmed.

Shimming with iron has the great advantage that the number of possible degrees of freedom, and therefore the degree and the order of the shimmable terms, is substantially higher than with electric shimming coils. A typical example is the compensation of the A_4^4 term, which is reasonably large in magnets with self-shielding (see Fig. 10.10) and which can be eliminated with passive shimming (Fig. 10.12). An added advantage is the reduced power consumption. When one dispenses with electrical shimming, the complex coils and the precision shim current regulator are eliminated and, along with them, a potential source of field instability. The main disadvantages of iron plate shimming: Retrofitting is extensive and time consuming. For spectroscopic application, this means that an additional correction coil system is usually necessary. Additionally, the iron mass per position is quantized and cannot be negative. These restrictions must be taken into consideration when writing a program for positioning the iron plates.

10.2.2 Gradient system

Criteria for required gradient field strength

As in the discussion of optimal field strength, the question arises here regarding the extent to which the maximum available gradient strengths influence attainable image quality. Here, too, the answer is not immediately obvious, since the dependencies which must be taken into consideration are quite complex. Since expenditures for a gradient system increase considerably with the maximum obtainable gradient strength and technological limits are quickly reached, practical compromises must be found here as well. The major parameters of immediate interest are the contrast/noise ratio (ΔS/N) and the desired spatial resolution. ΔS/N at a constant spatial resolution is dependent only on the length of the pulse sequence time intervals [10.9]. If these are set for an optimal S/N ratio, the gradients necessary for a certain spatial resolution are defined.

Pulse sequence time intervals

Since the design of a pulse sequence can be very flexible and there is a great range of variation in contrast which is influenced by the relaxation times T_1 and T_2 and the spin density of the subject, the optimization procedure can only be achieved through the use of several examples. The T_2 relaxation time plays an essential role.

The MR image contrast between two adjacent materials excited by 90° pulses can be approximately described by the following proportionality (see section 5.2.4):

$$\Delta S \sim \varrho' e^{-T_e/T_2'}(1-e^{-T_r/T_1'}) - \varrho'' e^{-T_e/T_2''}(1-e^{-T_r/T_1''}) \qquad (10.20)$$

T_e represents the time between excitation and readout of the MR signal (echo time) and T_r the repetition time of the pulse sequence. Prerequisite to the approximation are short pulse (T_p) and sampling (T_s) and echo (T_e) times, respectively ($T_e \ll T_1$, $T_p \ll T_2$, $T_s \ll T_2$) and a long repetition time ($T_r \gg T_2$) in comparison to the relaxation times. Image noise (N), on the other hand, is inversely proportional to the square root of T_s:

$$N \sim 1/\sqrt{T_s}. \qquad (10.21)$$

The relationship between T_e and T_s is dependent upon the form of the pulse sequence. For spin-echo sequences capable of probing multiple slices (often

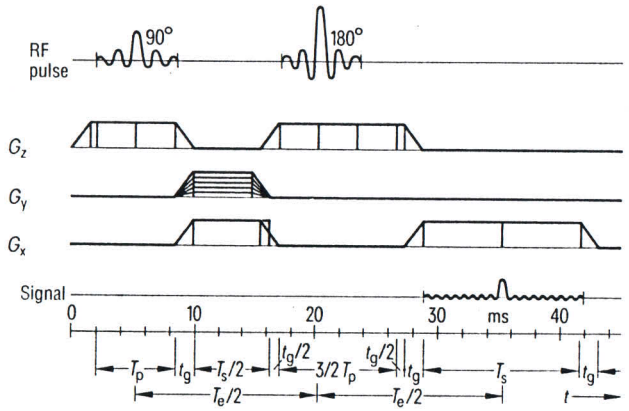

Fig. 10.13 Multiple slice spin-echo pulse sequence

used in practice) having one selective 90° and 180° pulse of the same length T_p (Fig. 10.13), T_e is:

$$T_e = T_s + 2T_p + 3t_g \tag{10.22}$$

(t_g is the rise and fall time of the gradients, which must be less than $T_s/2$), so that the noise is given by:

$$N \sim 1/\sqrt{T_e - 2T_p - 3t_g}. \tag{10.23}$$

Using the above formulas (10.20 and 10.23) ΔS/N can then be calculated as a function of T_e for various pairs of materials. Figure 10.14 illustrates a few examples; tissue parameters are taken from the literature [10.10].

It can be seen from the graph that the ΔS/N maximum lies at a rather long readout time and, consequently, at long echo times in relation to T_2. If the pulse time (or the sum $2T_p + 3t_g$) is added as an additional parameter, this results in ΔS/N curves such as those in Fig. 10.15. Shortening the quasi-parasitic T_p and t_g times yields a substantial improvement in MR image contrast.

There are additional limiting factors to be considered in the selection of sequence times:

On the one hand, due to the shifts between fat and water portions in the MR image and the constant field inhomogeneity, it is impractical to select

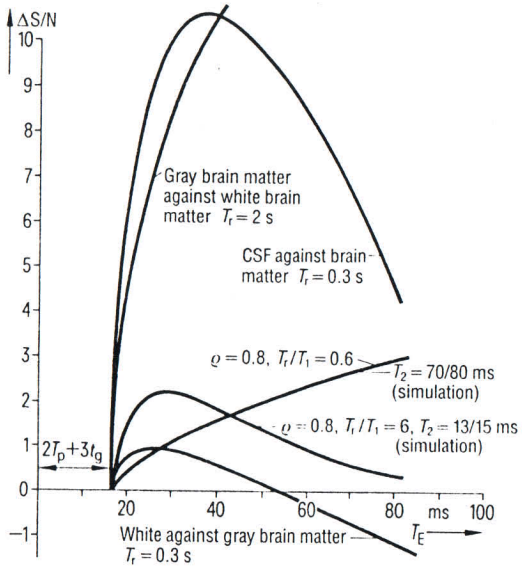

Fig. 10.14
Contrast/noise ratio as a function of echo time for gray and white brain matter at different pulse times

too small a receiving bandwidth, and therefore a T_s time which is too long. An acceptable compromise is to allow a fat/water shift equal to the pixel size, Δx.

Because

$$\delta x = \delta B_0 / G_x \quad \text{and} \quad \Delta x = \frac{2\pi}{\gamma G_x T_s} \tag{10.24}$$

the following is true for the data acquisition interval with $\delta x = \Delta x$:

$$T_s = \frac{2\pi}{\delta \gamma B_0}. \tag{10.25}$$

For a constant field strength of 1 T the readout interval is approximately 7.8 ms.

Another factor preventing an arbitrary decrease in pulse time is the fact that such a decrease causes a quadratic increase in the peak pulse power and therefore (if the pulse repetition rate is constant) a linear increase in power dissipation in the patient. As a compromise between the conflicting requirements of a short T_p, limited RF output and the sharpness of the slice profile, an (effective) pulse band width, $\Delta\omega_p/2\pi$, of approximately 0.8 kHz is chosen for the selective 90° pulse. In general a weighted sinc-pulse (see Section 5.2.2) with a length of at least twice the reciprocal bandwidth is used. This results in pulse lengths

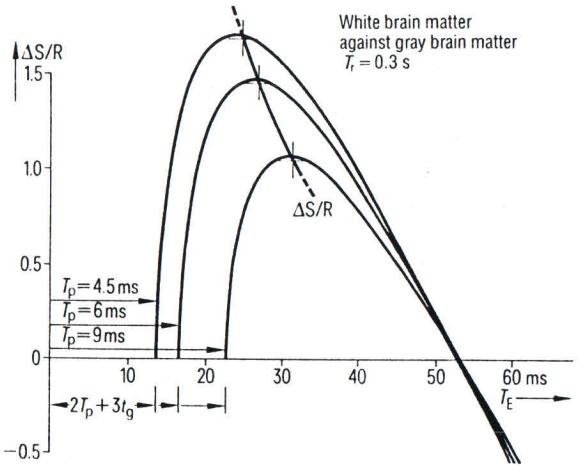

Fig. 10.15
Contrast/noise ratio as a function of the echo time for gray and white brain matter at various pulse times

of at least 2.5 ms. After the pulse sequence time intervals have been determined, the necessary gradients are calculated from the desired spatial resolution in readout, phase encoding and slice select direction as follows:

$$\Delta x=\frac{2\pi}{\gamma G_x T_s},\quad \Delta y=\frac{2\pi}{\gamma G_y T_s},\quad \Delta z=\frac{\Delta\omega_p}{\gamma G_z}. \tag{10.26}$$

At a minimum slice thickness of 3 mm or a pixel size of 0.5 mm, a maximum gradient of approximately 6 mT/m is required for a 1 T constant field under the above conditions. If the condition $\delta x=\Delta x$ is to be maintained at higher field strengths, or if even finer spatial resolution is desired, correspondingly larger field gradients are required.

Several of the special imaging procedures, such as flow refocussing, can also be implemented only when relatively high gradient field strengths are available.

Gradient coil

In principle the gradient coil set exhibits the same design as the shim coils of the first order. The dimensions of the winding, however, are adapted to the different requirements, namely high gradients and short switching times. High efficiency precludes the coil set's large linearity volume and free choice of diameter. The required number of ampere turns per gradient increases, taking into account the eddy currents generated in the cryo-shield, by the 4th or 5th

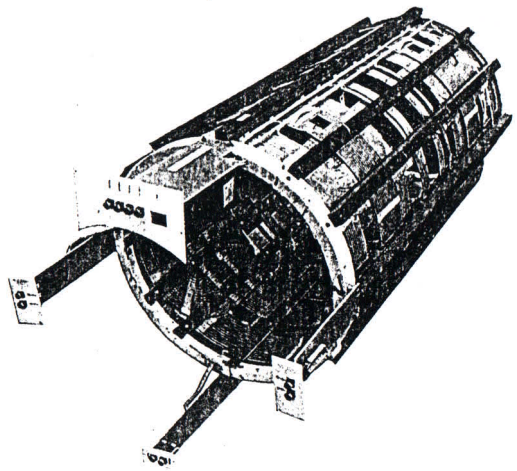

Fig. 10.16. Gradient coil system with 72 cm diameter for 6 mT/m at 100 A

power of the coil radius. A coil with a large number of windings requires less current. Such a coil shows, however, considerably more inductance and requires a correspondingly high voltage to switch the gradient fields in as short a time as possible. Figure 10.16 shows a gradient coil system having a 72 cm diameter, which generates a field of approximately 6 mT/m at 100 A.

Pulsed gradient power supply

The function of the gradient power supply is to generate current pulses of the correct amplitude and duration which correspond to the commands programmed in the pulse sequence controller. The currents required, including eddy current compensation (see section on effects of eddy currents), are 120 to 150 A. Since the gradient switching times are detrimental to the pulse sequence and should therefore be kept as short as possible, current increase rates of 150 kA/s are necessary. The inductive load requires a correspondingly high output voltage. Powerful amplifiers are required for this function alone. In addition, the power supply must be extremely precise and function with little ripple or noise. As described in Section 5.2.3, the gradient strength as a function of time directly determines the location of the sampled point in the spatial frequency domain (k space). The sampling error is the integrated time function of the gradient amplitude error from one sampling point to another. The sampling error, δk, is easily calculated for a sinusoidal gradient ripple of amplitude δG_b. Any other modulation can be expanded into a sum of sinusoidal modulations. The greatest sampling error occurs when the phase 0 or π coincides with the sampling time. It is then:

$$\begin{aligned}\delta k&=\delta G_b\gamma\int_0^{\Delta t_s}\sin\omega_3 t'\,dt'\\&=2\delta G_b\gamma\int_0^{\Delta t_s/2}\cos\omega_b t'\,dt'\\&=\frac{2}{\omega_b}\delta G_b\gamma\sin\frac{1}{2}\omega_b\Delta t_s.\end{aligned} \tag{10.27}$$

One can see that the sampling error disappears regardless of the phase when the ripple frequency is a multiple of the sampling frequency. Figure 10.17 shows the frequency-dependent limit curve for the permissible relative gradient interference amplitudes for each sampling error relative to the sampling interval. Simulations show that this should be less than 1% for incoherent and 0.2% for coherent (with respect to the sampling interval, Δk) gradient modulations and that these levels may not be exceeded if visible artifacts are to be avoided. This applies to the readout gradients as well as to the phase encoding gradients, as can be seen from the equivalence of $\Delta t_s \cdot G_x$ and $\Delta G_y \cdot T_s/2$.

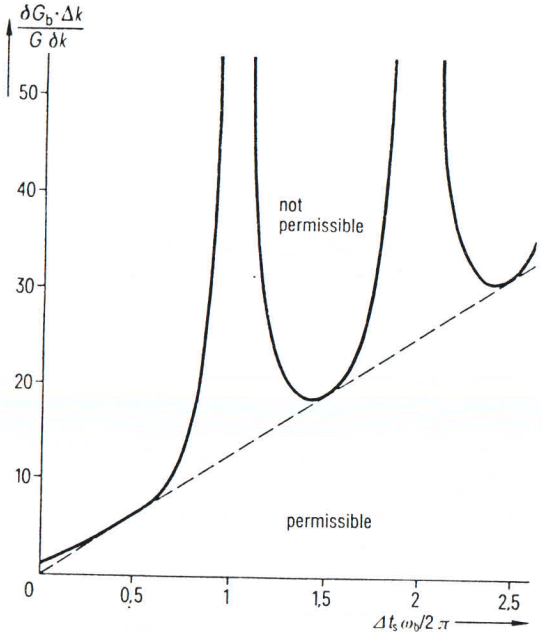

Fig. 10.17
Permissible gradient field ripple as a function of the ripple frequency

The reciprocal time between the RF pulses can be designated as the lowest ripple frequency that must be considered, since slower periodic interferences across a sampling line for all practical purposes cause a constant shift in the k space, for which

$$\frac{\delta G}{\Delta G} \leq \frac{\delta k}{\Delta k}. \tag{10.28}$$

Here, $\Delta G = G/N$, with an image matrix size of N is required. This is identical to the necessary reproducibility for the gradient amplitude.

For a field of view of 50 cm and a readout time of 8 ms, ΔG has the value 12 μT/m. For incoherent, low-frequency fluctuations of the gradient strength, 0.12 μT/m or 20 ppm of the maximum gradient strength of 6 mT/m or of the coil current is permissible.

For slice positions which do not pass through the center of the magnet, an instable gradient field has the same effect as a fluctuation of the constant field:

$$\delta B_0(t) = z\,\delta G_z(t). \tag{10.29}$$

The limits for this were formulated in Section 10.2.1.

As expected the resulting stability requirements are comparable to those discussed above.

Current amplifiers having a linear final stage or a switch-mode final stage operating at a relatively high frequency are used to comply with the required output specifications (Fig. 10.18). The gradient pulse, which is in digital form, is converted to an appropriate voltage pulse via a digital-to-analog converter (DAC). This pulse is predistorted using a high-pass filter which, in general, comprises multiple time constants in order to compensate for the field pulse distortion due to the cryo-shield eddy currents (see next section). The driver amplifier and the final stage follow, both powered by a high output bi-polar DC power supply. All the components in the amplifier chain must meet the stringent requirements mentioned above.

The regulator circuitry is particularly critical, since it is essential that this is not prone to oscillations, despite the required level of precision and a large bandwidth (≈1 kHz). It must be able to stabilize oscillating counter-EMF voltages resulting from the mechanical vibrations of the gradient coil in the constant field, as well as ripple caused by the DC power supply. The fundamental difference between linear amplifiers and switching amplifiers lies in the control over the final stage: The linear amplifier is directly driven by the analog signal, whereas a so-called modulator is connected just prior to the final stage of the switched amplifier. The modulator converts the control voltage into a rapid series of rectangular switching pulses having a pulse duty factor proportional to the desired output current. The current flows through the gradient coils via diodes during the "off" phase and falls off with the time constant, L/R. The frequency of the pulse signal must be significantly higher than R/L, in order that the current ripple remain sufficiently small. In addition, higher frequency ripple causes less interference.

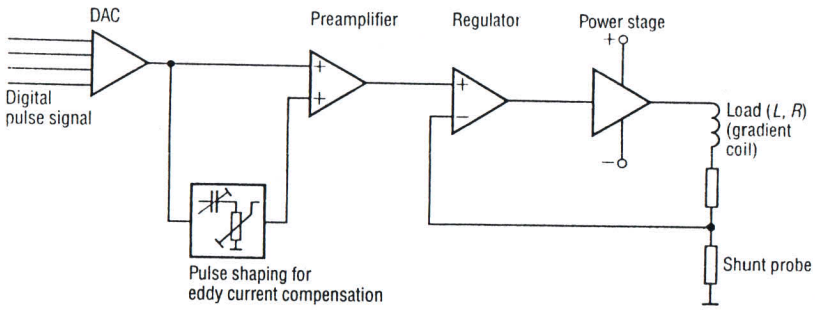

Fig. 10.18 Block circuit diagram of a gradient amplifier

The switching amplifier has several advantages over the linear final stage that make its use worth the extra technological effort. The power dissipation of the final stage, and therefore energy usage and cooling effort, is significantly lower. In the linear final stage the full supply voltage is present between the collector and the emitter of the output transistors after the gradient coil has been excited to the programmed current level; with the switching amplifier there is only the saturation voltage. The power supply in this case needs to supply power to compensate for losses in the coil and the cables only. As can be seen in Fig. 10.13, the excitation and de-energization of the gradient field is accomplished in exactly defined time periods. The power transistors in a linear controller must withstand a high counter-EMF voltage at high currents during the fall time. Diodes cannot take over the induced voltage in this case, because this would lead to current-dependent switching times. The effective switching times of the output transistors in a switching amplifier, on the other hand, are only about 1 µs. Inductive voltages can be handled by diodes, since transients are irrelevant in relation to the effective current through the gradient coil. This technology therefore allows for substantially more compact and powerful amplifiers.

Eddy current effects

Since the tradient coils are surrounded concentrically by the cryostat, as shown in Fig. 10.1, the magnetic flux in the cryoshields changes when the coil current is changed. This leads to the formation of eddy currents which counteract the field changes according to Lenz's law, as demonstrated for the Z-gradient in Fig. 10.19. Since the eddy current distribution, especially in the radial direction, differs from the coil current distribution, the spatial dependence of the eddy current field is different from that of the coil field. This must be taken into consideration when calculating the design of the coil, in order to avoid dynamic gradient non-linearity. Eddy currents increase with increasing coil current. As soon as the coil current has reached a constant value, the eddy current begins to decay. This can be closely approximated using an exponential function with

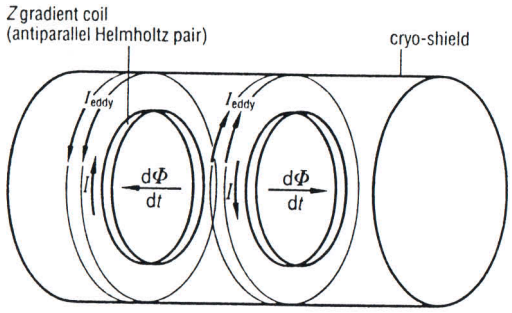

Fig. 10.19
Eddy currents generated by a pulsed gradient field

a time constant determined by the conductivity and the effective inductance of the cryo-shield. As the field penetrates through the first shield, eddy currents are induced in the outer shield and possibly in the superconducting coil itself. This leads to a complex distribution of eddy currents, in turn resulting in a gradient counter-field. For the rise times of approximately 1 ms considered here, the initial strength of the eddy current (and therefore the weakening effect on the field) is determined solely by the geometry of the coils and the innermost shield, i.e. by their inductive coupling. For the most part, only the ratio of diameters has to be taken into consideration, while the conductivity of the shield is practically irrelevant.

The gradient field increases as the eddy currents decay (Fig. 10.20a) and also changes in regard to its spatial dependence. This dynamic change in field distribution, which can be as much as a few percent of the eddy current field, cannot be compensated for by a modification of the current pulse form. This means that the conductivity of the innermost shield of the cryostat should be relatively high, so that the eddy current time constants are significantly longer than the length of the gradient pulses normally used. Such a time/space dependency of the gradient field makes it impossible to reconstruct an image exactly from the measurement data with the help of a Fourier transformation and can lead to image degradation. In addition, good conductivity reduces heat generation in the shield and prevents the boil-off rate for the nitrogen and helium from rising.

In addition to spatial changes in the field, the eddy current field has the same effect on the gradient pulse sequence as a low-pass filter. The inclusion of an adjustable high-pass filter in the gradient amplifier distorts the shape of the pulse in such a way that the desired gradient pulse shape is re-established (see Fig. 10.0b).

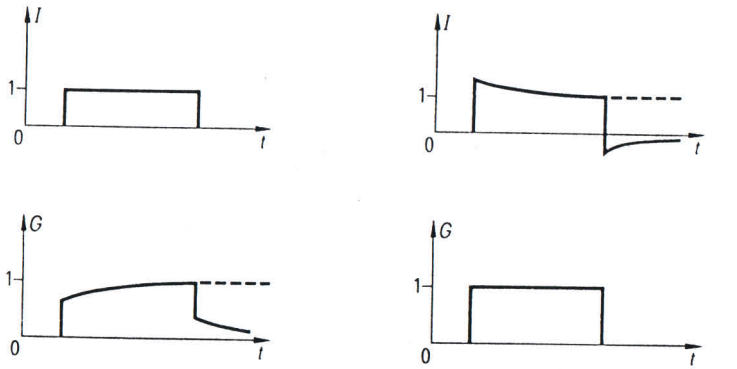

a) without eddy current compensation b) with eddy current compensation

Fig. 10.20 Current and gradient pulse shape

There are several aspects to the importance of exact eddy current compensation. A short discussion of the most important of these follows.

Equidistant sampling points in the spatial frequency domain (k space)

The same considerations apply here as were presented for the specifications of gradient amplifier stability. It follows at once from

$$k=\gamma\int_0^t G(t')\,dt' \quad \text{or} \quad \Delta k=\gamma\int_{t_s}^{t+\Delta t_s} G(t')\,dt' \tag{10.30}$$

that the gradient must be constant during the readout of the MR signal in equidistant time steps, Δt_s, so that the spatial frequency domain is evenly sampled. The same applies to the slice selection method with frequency selective excitation pulses in the gradient field.

Refocussing in selection Gradients

As explained in section 5.2.2, a gradient pulse of appropriate length and amplitude must make up for the phase dispersion of nuclear magnetization in the slice direction after an excitation pulse. Improper refocussing across the slice leads to signal loss, since only magnetization parallel to the direction of magnetization at the center of the slice contributes constructively to the signal. This is illustrated in Fig. 10.21.

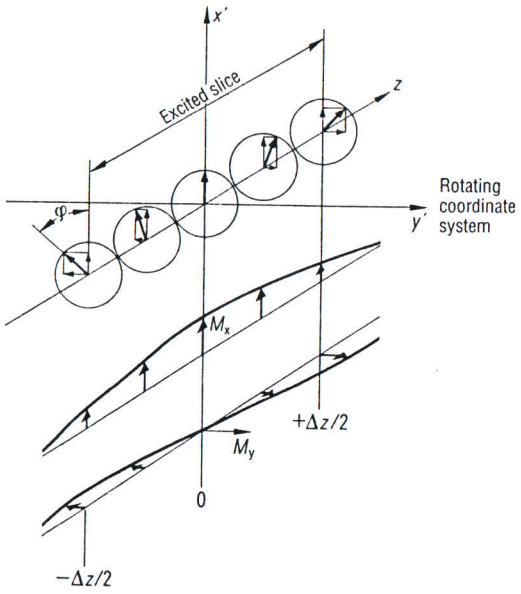

Fig. 10.21
Phase dispersion of magnetization across the slice due to incomplete refocussing

The phase angle in the slice direction is:

$$\varphi(z)=z\gamma\int G_z(t)\,dt=z\Delta k_z. \tag{10.31}$$

Integration limits for a pulse sequence without a 180° pulse extend from the center of an excitation pulse to the readout interval. This also applies to spin echoes, but the time integrals before and after the center of the 180° pulse must be added together with opposite signs. Since the expression for the signal across the slice behaves as $\cos\varphi(z)$, the relative signal loss as a function of Δk_z is:

$$\frac{S}{S_{max}}=\frac{2}{\Delta z}\int_0^{\Delta z/2}\cos\Delta k_z\,z\,dz=\mathrm{sinc}(\tfrac{1}{2}\Delta z\Delta k_z). \tag{10.32}$$

Since the pulse sequence programs are written independently of the system, with the length of the refocussing gradient pulse just equal to $0.5\,T_p$ (apart from a small correction for the rise time, t_g) (Fig. 10.13), a trapezoidal gradient pulse form must be assured via correct eddy current adjustment. This is necessary to achieve $\Delta k_z=0$, i.e. an optimal signal/noise ratio.

It should be mentioned that the potential problems caused by eddy currents can be eliminated, at least partially, by so-called active shielding; that is, an external, opposed winding similar to the shielding of the fringe field for a magnet [10.11]. In principle, the active shield is a second set of gradient coils mounted concentrically on a cylinder of a larger radius. The windings are connected in series electrically opposite to the direction of their corresponding field windings. Their dimensions are such that flux changes at the cryo-shield (and as a result the eddy currents) during current changes are kept to a minimum. At the same time the useful gradient amplitude is reduced, since the shield coil field is superimposed on the field of the inner coil. The size and weight of this configuration are also disadvantages. Ohmic loss is disproportionately high, because the necessary degree of efficiency can only be obtained by raising the number of ampere turns and because the power dissipation of the shield winding must also be taken into account.

10.2.3 RF system

Transmit and receive system

The RF electronics of an MR system are designed to generate the pulsed RF output required to excite magnetic resonance and to prepare the signals picked up by the antenna for the image processor. The signal paths are illustrated in Fig. 10.22.

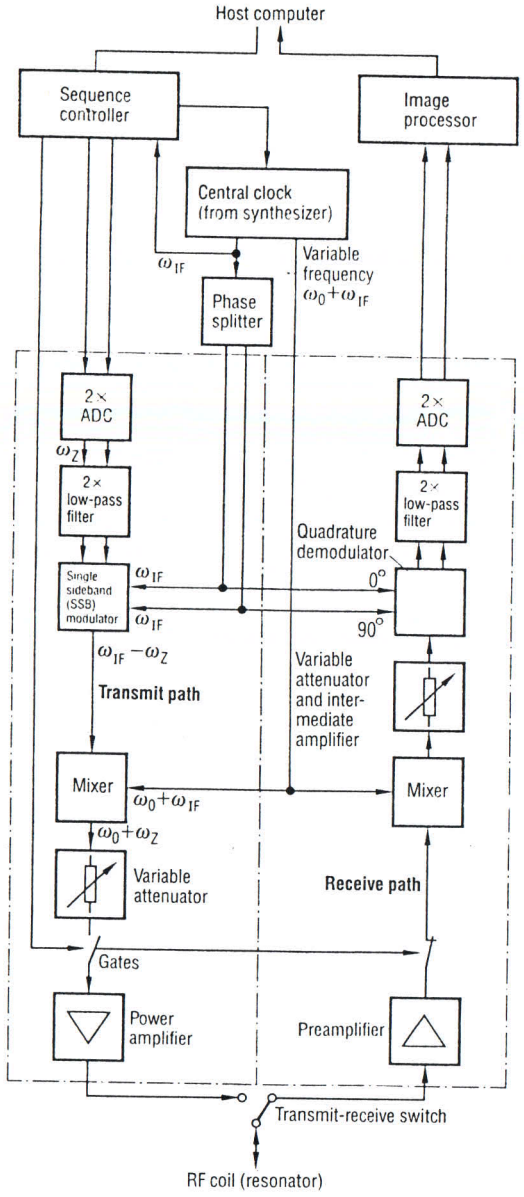

Fig. 10.22
Circuit diagram of the RF System

Transmit path

The RF pulses required for magnetic resonance are supplied digitally as a series of complex numbers by the sequence controller. The magnitude of a complex numerical value represents the momentary amplitude and the phase determines the direction of the B_1 field in the rotating frame. The series of complex numbers is converted to low-frequency voltage pulses by two digital-to-analog converters (DACs). The bandwidth and the length of the programmed pulse form are determined by the sample clock and the number of data points. The signals are fed into the modulator via two low-pass filters, which suppress the undesirable harmonics caused by the digital generation of the pulse.

Modulator

The function of the modulator corresponds to the transformation from the rotating frame to the laboratory frame. It multiplies the complex pulse form (the low frequency signal), $\mathcal{F}(t)$, by the complex carrier signal, $e^{i\omega_0 t}$ (Fig. 10.23a). The real part of the product appears at the output of the modulator:

$$\mathrm{Re}[\mathcal{F}(t)\,e^{i\omega_0 t}] = \mathrm{Re}[\mathcal{F}(t)]\cos\omega_0 t - \mathrm{Im}[\mathcal{F}(t)]\sin\omega_0 t. \qquad (10.33)$$

If the low-frequency signal is:

$$\cos(\omega_z t+\varphi)+i\sin(\omega_z t+\varphi)=e^{i(\omega_z t+\varphi)},$$

the output signal is:

$$\mathrm{Re}[e^{i(\omega_0 t+\omega_z t+\varphi)}]=\cos[\omega_0 t+\omega_z t+\varphi).$$

By introducing the factor $e^{i(\omega_z t+\varphi)}$ into the low-frequency pulse signal, the frequency and phase of the high frequency excitation pulse can be shifted as

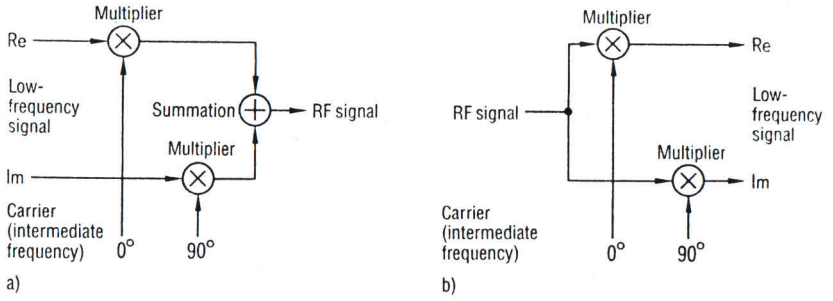

Fig. 10.23 Single sideband modulator (a) and quadrature demodulator (b)

desired. When feeding the modulator with $e^{i\omega_z t}$ only one frequency, $\omega_0+\omega_z$, appears at the output. Since the carrier frequency, ω_0, as well as the mirror frequency, $\omega_0-\omega_z$, are suppressed, the configuration is referred to as a single side-band modulator (SSB) [10.12].

Programming a frequency offset is a simple method of achieving a shift, z, of the slice excited with the help of a selective pulse while the gradient, G_z, is switched on:

$$z=\omega_z/(\gamma G_z). \tag{10.34}$$

The modulator is composed of a pair of ring mixers, supplied with the carrier signals shifted in phase by 0° or 90°. The most important characteristics are the linearity (i.e., the absence of spurious signals and harmonics), which determines the fidelity of the pulse shape, and the suppression of carrier and unwanted sideband signals. Insufficient suppression of undesirable frequencies results in magnetic resonance excitation at locations other than the slice selected and therefore leads to artifacts. A constant DC voltage on the low-frequency side generates a carrier signal at the modulator output. A signal from the unwanted sideband is generated if the two ring mixers are not precisely balanced or when the carrier signals are not shifted in phase by exactly 90°.

A single sideband modulator possessing good side-band suppression and carrier attenuation is best realized at sufficiently narrow frequency ranges. An intermediate frequency is used as a carrier, so that it is not necessary to have a different modulator for each type of nucleus or each variation in field strength. The mixer, coupled at the output side of the modulator, generates the pulse signal at a center frequency, ω_0, for the corresponding MR frequency. Transmission output is regulated for the differing B_1 field strength requirements using adjustable, variable attenuators. A gate circuit inhibits the transmit path while the system is in the receive mode. This prevents the noise and the carrier signal generated by the modulator from reaching the receiver circuitry via the power stage and interfering with the weak MR signal.

RF power transmitter

The RF final stage must amplify the pulse so that a (rotating) B_1 field is generated in the subject surrounded by the resonator. This field must fulfill the following requirements:

$$B_1=\frac{\alpha}{\gamma t_p} \tag{10.35}$$

α = Flip angle of magnetization
t_p = effective time for the B_1 field

If the RF field is linearly polarized, twice the B_1 amplitude is required for the same flip angle. Power is required because there are losses in the object being measured, as well as in the resonator and its connecting lines. For a cylinder with its axis parallel to the constant field and therefore perpendicular to the B_1 field, the power required to generate a given B_1 field can be approximated as follows:

$$P_{\text{sample}}=\frac{\pi}{512}\omega_0^2\,\sigma B_1^2[D^4 l+\tfrac{4}{3}D^2 l^3]. \tag{10.36}$$

If one assumes the following values, for example: Cylinder dimensions: $D=l=40$ cm, conductivity $\sigma=0.5/\Omega$m (equivalent to a physiological saline solution), flip angle = 180° with an effective time of $t_p=1.0$ ms, thus resulting in a linearly oscillating field $B_1=23.5\,\mu$T and a center frequency $\omega_0=2\pi\cdot 42.576$ MHz, then P_{sample} is approximately 2.8 kW. Under experimental conditions using a patient of average weight (approximately 80 kg), 1.3 kW of power can be measured at the input of the antenna. As was determined by the measurement of loaded and unloaded Q, (Eq. 10.8 in Sect. 10.2.1) approximately 20% of this is lost in the resonator. Only slightly more than 1 kW will therefore be absorbed by the patient; the cylindrical model is therefore too pessimistic. This can be explained by the inhomogeneity of conductivity and the shape of the human body. The cables and components of the transmit/receive switch attenuate the RF output by approximately 1 dB. The final stage, therefore, must be able to provide 2 kW of pulse power. The final stage at 42 MHz is designed for 8 kW, so that shorter pulses are possible and so that there is some reserve power to compensate for the greater degree of attenuation caused by heavier patients. The 63 MHz final stage is designed for a pulse output of 15 kW to allow for the rise in loss, proportional to ω_0^2, within the measured object.

The average available output power may be considerably lower than the above. Output power is basically governed by local regulations for medical equipment and by how much the patient's safety will be affected by the specific rate of absorption. Thermal dimensioning and the power supply for the final stage are designed for the continuous output power needs, while the energy for a high-output pulse or series of pulses is taken from a buffer storage device, such as a capacitor battery, which is recharged during off times. Figure 10.24 shows the operating range of the transmitter between the pulse period and the continuous output power limits. The pulse duty factor and pulse output are approximately inversely proportional to one another over the operating range. The position of this range in the diagram marks the storage capacity.

Power amplifiers with these characteristics are equipped with tubes, since these are less sensitive to short-term overloads and are less expensive. The output circuit is tuned to the resonance frequency and is simultaneously the primary

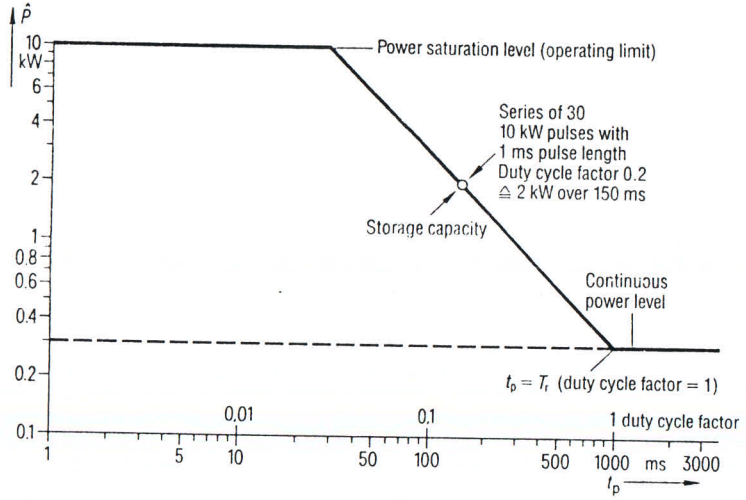

Fig. 10.24 Effective operating range of the pulsed RF final stage

side of the output transformer, which matches the final stage to the line impedance. Final stages are biased as Class C, i.e. without quiescent current when no input signals are present, as well as in the pulsed Class A (quiescent current equal to half of the maximum current during the transmit phase). The Class-C mode is characterized by an efficiency of nearly 1, but the RF output voltage is not proportional to the input voltage. This can be compensated for by pre-distorting the amplitude of the pulse shape, $|\mathscr{F}(t)|$. When using pulsed Class A operation, the power supply must generate power independently of the RF amplitude during the entire transmit phase; i.e., the amount of power dissipated is relatively high, especially for amplitude-modulated pulses. On the other hand, amplitude correction (pre-distorting) may not be necessary. The gain during the receive intervals for both modes is minimal, so that noise from the modulator, mixer and driver amplifier is largely suppressed.

Receive path

The receiving channel is shown in the right half of Figure 10.22. The MR signals are received by the receiver coil and then amplified to a sufficient level by the preamplifier, so that line attenuation and input noise from the following stage is negligible. The frequencies received from the coil are approximately the nuclear resonance frequency, ω_0. This band of frequencies is then translated by the mixer to an intermediate frequency range, so that a standard attenuator/demodulator assembly can be used regardless of the type of nucleus or the constant field strength.

Demodulator

The function of the demodulator is complementary to that of the modulator, namely the transformation of the laboratory coordinate system into the coordinate system that rotates with ω_0. The input voltage represents the transverse magnetization as

$$M_x \cos \omega_0 t + M_y \sin \omega_0 t, \tag{10.37}$$

where

$$M_x + iM_y = M_\perp e^{i(\omega_0 t + \varphi)}$$

and

$M_\perp$ = Magnitude of magnetization
φ = Phase of magnetization.

The demodulator multiplies (see Fig. 10.23b) the complex carrier signal by the input signal as follows:

$$\begin{aligned}(M_x \cos \omega_0 t + M_y \sin \omega_0 t) \cos \omega_0 t &= \tfrac{1}{2} M_x + \tfrac{1}{2} M_x \cos 2\omega_0 t - \\ &\quad - \tfrac{1}{2} M_y \sin 2\omega_0 t \\ (M_x \cos \omega_0 t + M_y \sin \omega_0 t) \sin \omega_0 t &= \tfrac{1}{2} M_y - \tfrac{1}{2} M_x \sin 2\omega_0 t + \\ &\quad + \tfrac{1}{2} M_y \cos 2\omega_0 t. \end{aligned} \tag{10.38}$$

With the exception of terms having twice the carrier frequency, signals representing the M_x and M_y components of the nuclear magnetization reach both outputs. This type of circuit is called a quadrature demodulator. Since it can distinguish between frequencies greater and smaller than ω_0 (upper and lower side bands) the output bandwidth is half of the input bandwidth. This improves the signal-to-noise ratio by $\sqrt{2}$ in comparison to simple phase-sensitive rectifiers [10.13], which can represent only one component (M_x or M_y). In addition, only half the conversion rate is necessary for the analog-to-digital conversion. On the other hand, there must be two of each of the components following the demodulator. Output signals are transmitted through a pair of low-pass filters which cut off all frequencies exceeding half the sampling frequency (the Nyquist frequency). The two ADCs then convert these into a sequence of complex numbers suitable for processing by computer.

The frequency responses and the phases of the ring mixers, filters and ADCs must be in exactly equal pairs, and the two carrier signals for the quadrature demodulator must be shifted by exactly 90°. If these conditions are not met, the result will be artifacts, such as mirror images, corresponding to the incomplete separation of the upper and lower side bands.

Signal levels

In order to specify the necessary total gain and dynamic range; i.e., the operating limit divided by the noise level, the expected signal-to-noise ratio and input voltage at the preamplifier must be known. Prognoses, however, as discussed in the section on pulse output, are only valid within limits, because the human body can not be described by a simple mathematical model. It is also not possible to calculate coil characteristics exactly. One must rely on the results of empirical studies. If the antenna impedance is always matched to the actual line impedance, R_L (50 Ω), via tunable circuits, the noise voltage at the input of the preamplifier (input impedance Z_i) is always the same, regardless of the coil load.

$$U_N = \frac{|Z_i|}{R_L + |Z_i|}\left(4kTR_L \frac{\Delta\omega_s}{2\pi} \cdot 10^{F/10\,\mathrm{dB}}\right)^{1/2}, \qquad (10.39)$$

where F is the noise figure of the preamplifier in dB.

The total gain of the receive channel is given by the gain of the individual components minus the attenuation values of both the attenuator and the cables. The antenna and preamplifier noise, which is dependent upon the input bandwidth $\Delta\omega_s = \pi/\Delta t_s$, should be sufficiently higher than the frequency-independent ADC quantization noise. For the smallest commonly used bandwidth the gain must be greater than:

$$\frac{U_0}{U_i} > \frac{1}{\sqrt{12}} \frac{U_{LSB}}{U_N} \qquad (10.40)$$

(see level plan, Fig. 10.25).

The amplitude of a useful signal depends largely on the type of MR experiment performed, especially on the volume excited. Several typical results for $\omega_0/2\pi = 63$ MHz are shown in Fig. 10.25. The dynamic range of the MR signal is substantially higher than 100 dB, especially for non-selective excitation. This means that the S/N gain resulting from the excitation of a large volume (e.g., for three-dimensional imaging) cannot be fully realized in any case with conventional 16-bit ADCs. It is then obvious that the dynamic range of all the components in the receive branch should not be smaller than that of the ADC. The adaptability of the preamplifier as well as the variable attenuation elements in the intermediate amplifier also allow the processing of high input signals, such as found when dealing with thick slices and non-selective excitation. This can be performed without overloading the ADC or the output of the preamplifier.

Transmit/receive switch

The transmit/receive switch is the link between the RF resonator and the RF pulse transmitter or the preamplifier. It must enable the path from the transmitter to the antenna during the RF pulse and at the same time protect the sensitive preamplifier from the high pulse power. In the receive mode the weak MR signal must reach the preamplifier with as little attenuation as possible, and the noise of the final stage must be excluded from the antenna circuit. Figure 10.26 shows a simplified wiring diagram of the switch, which automatically toggles between transmit and receive without additional control circuitry. The anti-parallel pair of diodes in the transmit cable does not conduct during the receive mode and prevents noise generated by the power section from reaching the preamplifier, as well as preventing the MR signal from disappearing in the transmitter. In the transmit mode, the voltages are high enough to switch on the diodes, so that the power reaches the antenna (resonator) with practically no loss. The pair of diodes at the preamplifier input also conducts. The $\lambda/4$ cable connected in front of the diodes transforms the short circuit to a high impedance at the input of the antenna. In the receive mode, the impedance

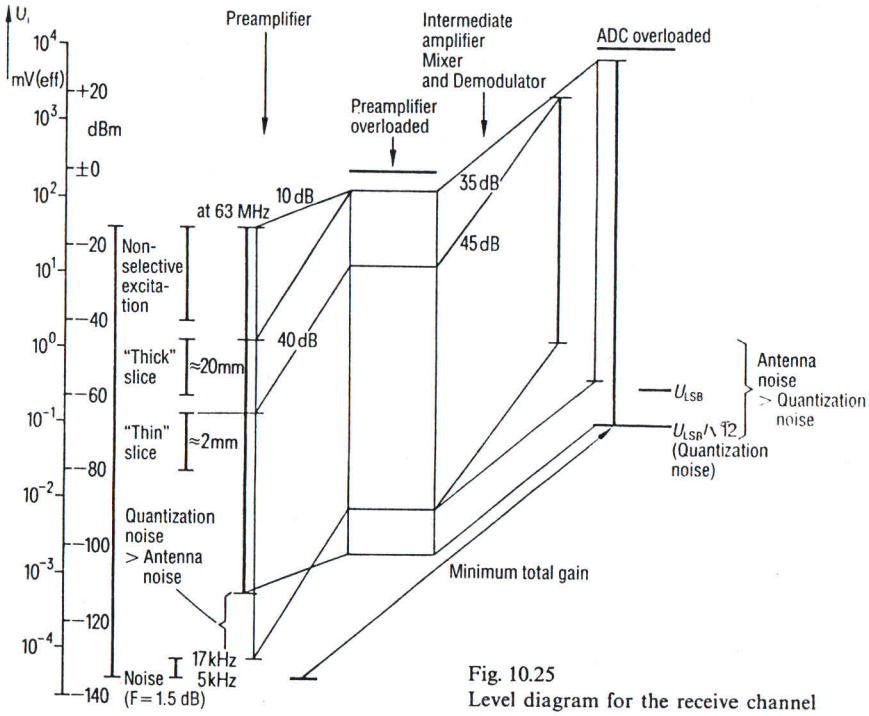

Fig. 10.25
Level diagram for the receive channel

of the diodes is high and the signal reaches the preamplifier virtually unattenuated via the $\lambda/4$ line. The circuit contains other adjustable components which neutralize the diode capacitance.

Phase noise

Section 2.1 mentions the importance of the phase stability in MR signals for the generation of artifact-free images when using the Fourier method. It therefore follows that all phase fluctuations generated by all the RF components together must remain significantly under the critical 3° limit. This is especially true for the frequency synthesizer, which serves as the system clock.

Coils and resonators

Coils and resonators, generally called antennas, generate the alternating magnetic field for magnetic resonance excitation and receive the field emitted by the precessing nuclear moment. They therefore comprise the component of the MR system directly interacting with the object to be measured.

In connection with the discussion of the signal-to-noise ratio of the magnetic resonance experiment presented in Section 5.1.8, the most important properties of antennas were described. These are the distribution function of the B_1 field resulting from the current in relation to the sample geometry and the coil quality factor, Q.

Antenna characteristics

The peak output voltage $\hat{U}$ from a coil characterized by a field-current distribution $\vec{B}_i(\vec{r})$ over a sample with precessing nuclear magnetization is:

$$\hat{U} = \omega_0 \int_{V_{sample}} \vec{M}\vec{B}_i \, dV. \tag{10.41}$$

The resulting received output power (short circuit at the coil outputs) is then:

$$P = \tfrac{1}{2}\hat{U}^2/R. \tag{10.42}$$

A maximum of only half the output is available when the coil has been matched to subsequent components; e.g., using the matching circuitry illustrated in Figs. 10.26, 10.27 or 10.33 (impedance transformers). This fact is of no importance, however, for the following discussion (see equivalent circuit diagram 10.27). Important is that the useful signal output amplitude increases with matching the spatial coil field distribution to the distribution of the magnetization and falls with the resistive loss. The term "matching" is to be understood

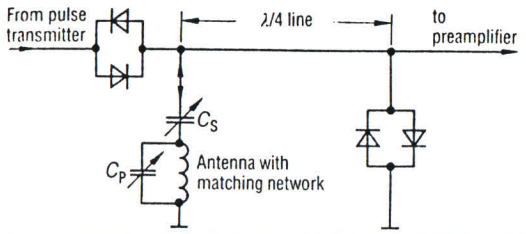

Fig. 10.26
Simplified circuit diagram of transmit-receive switch

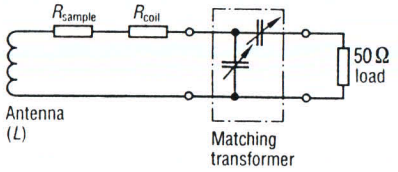

Fig. 10.27
Equivalent circuit diagram of a transmit-receive coil (antenna) with loss

in a very general manner; i.e., not only that the probe volume should correspond to the sensitive volume of the antenna, but that the vectors $\vec{M}$ and $\vec{B}_i$ should be parallel. It then follows that an antenna whose B_1 field is perpendicular to B_0 and is circularly polarized should be, theoretically, superior to any other configuration, because the nuclear magnetization precesses about the B_0 direction. Loss due to resistance is simultaneously the source of undesirable noise. It can be divided into the resistance induced by the sample and that caused by the coil:

$$R = R_{sample} + R_{coil}. \tag{10.43}$$

The loss in useful signal caused by the subject to be measuremend and the noise it generates is unavoidable. An expression for R_{sample} can be found in Section 5.1.8. R_{coil}, on the other hand, can be optimized:

$$R_{coil} = \frac{\omega_0 \int_{V_{coil}} B_i^2 \, dV}{2\mu_0 Q_0}. \tag{10.44}$$

With the definition of the filling factor η:

$$\eta = \int_{V_{sample}} B_i^2 \, dV \Big/ \int_{V_{coil}} B_i^2 \, dV \tag{10.45}$$

i.e., the fraction of the field energy penetrating the sample in relation to the total field energy produced, it follows that:

$$R_{\text{coil}} = \frac{\omega_0 \int_{V_{\text{sample}}} B_1^2 \, \mathrm{d}V}{2\mu_0 \eta Q_0}. \qquad (10.46)$$

Coil losses therefore increase with frequency and sample volume and decrease with the unloaded Q_0 and the filling factor. In summary, the following characteristics are required for an optimized MR antenna:

1. The field distribution should be homogeneous across the measurement volume to assure spatially uniform nuclear resonance excitation.
2. The filling factor should be large.
3. The direction of polarization should be perpendicular to the constant field and (if possible) circular.
4. Energy losses should be minimal compared to the losses induced by the subject to be measured; i.e., the unloaded Q_0 should be high.

Characteristics 1 and 2 may occasionally conflict in medical practice, namely when a portion of the body which cannot be surrounded by a coil is to be imaged. For these cases so-called surface coils are used; i.e. the homogeneity of the B_1 field (in general, only in the receive mode) is sacrificed in favor of a large filling factor in order to achieve the largest possible $\Delta S/N$. In turn, this can be traded off against adequate spatial resolution.

Antennas with homogeneous field distribution

Coils and resonators (antennas) must surround the subject to be measured in order to generate a homogeneous B_1 field within the subject. A suitable configuration would be a solenoid arranged coaxially with the axis of the body. Since B_1 and B_0 must be perpendicular to one another, this type of coil configuration can be used only with yoke or resistive magnets (see Sect. 10.2.1 and Fig. 10.7). In addition, the resonance frequency of a solenoid having a diameter corresponding to the size of a human body is substantially lower (due to unavoidable parasitic capacitance) than the MR frequency normally used. It is necessary to find cylindrical structures, which at high frequencies generate a homogeneous field polarized in the direction perpendicular to the axis of the magnet. A sufficiently long tube, subjected to a constant current distribution $J(\varphi)$

$$J(\varphi) = \hat{J} \sin \varphi, \qquad (10.47)$$

as shown in Figs. 10.28a and b, will generate the desired field distribution [10.14].

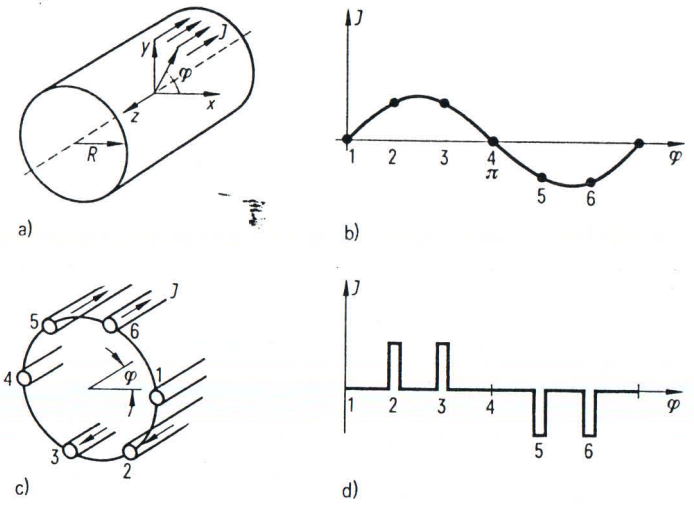

Fig. 10.28 RF Antenna with homogeneous B_1 field

a) Hollow tube with current density distribution in longitudinal direction
b) Ideal current distribution
c) Resonant conductors arranged as a discrete hollow tube
d) Current distribution in a discrete hollow tube for a nearly homogeneous B_1 field

Implementing this current distribution is not a simple matter. The current density can be approximated for several angles with discrete conductor paths (Figs. 10.28c and d). The conductors at $\varphi = 0$ and 2π may be eliminated, since they do not carry any current. If the wire rods are connected in the manner shown in Fig. 10.29, the result is a so-called saddle coil, which can be used in situations when the frequency is not too high or the diameter not too large (up to 30 cm at approximately 25 MHz).

At higher frequencies and larger diameters (whole-body antennas) the length of the conductors is no longer short compared to the RF wave length, so

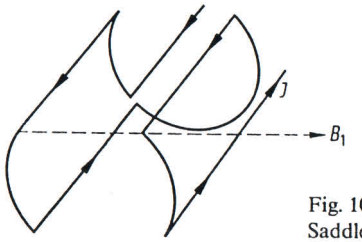

Fig. 10.29
Saddle coil for low frequencies or small coil dimensions

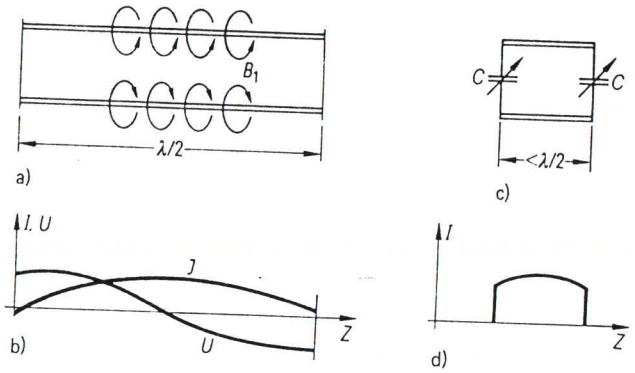

Fig. 10.30 λ/2 (half wavelength) resonator (antenna)

a) Conductor configuration
b) Current distribution
c) Shortening the conductors by applying a capacitive load to the ends
d) Current distribution with shortened conductors

that the desired current distribution can no longer be achieved with a saddle coil. Here the λ/2 resonator principle (see Fig. 10.30) becomes of interest. If a wave having the length $\lambda = 2\pi c/\omega_0$ (where c is the velocity of wave propagation) is generated on a double conductor (Fig. 10.30a) and the conductor is λ/2 long, a resonance or standing wave is produced which has a current distribution as shown in Fig. 10.30b, resulting in the corresponding B_1 field distribution. The circuit can be shortened symmetrically by adding capacitances, so that a nearly uniform current distribution arises in the longitudinal direction (Fig. 10.30c, d). Such resonant conductors can be configured as a hollow tube, as shown in Fig. 10.28d. A cross section of such a configuration is shown in Figure 10.31. The sections of the conductors are composed of rods having adjustable capacitors connected between the antenna and ground (exterior shielding). This λ/2 resonator [10.15] can be used as a transmit/receive antenna for whole-body magnetic resonance imaging up to 63 MHz.

Aldermann and Grant have developed a variation of this principle (Fig. 10.32) [10.16]. It is used primarily for head-imaging antennas, since the structure is open on two sides and is therefore more pleasant for the patient. The symmetrization to ground potential is accomplished via two inner rings.

A circularly polarized B_1 field can be generated with the above antennas by joining pairs of resonators attached coaxially, but at a 90° angle to one another. These partial systems are driven during the transmit mode via a power divider and a phase shifter in such a way that a high-frequency rotating field is generated

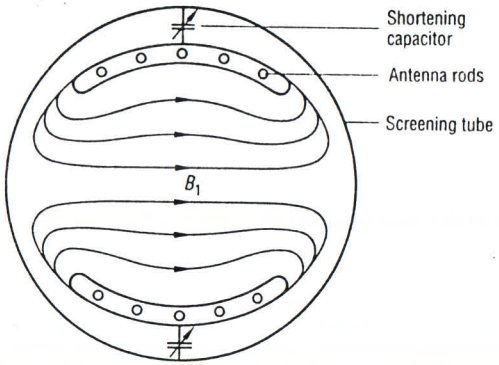

Fig. 10.31
Cross section of a whole-body antenna using the conductor resonance principle (suitable for high frequencies)

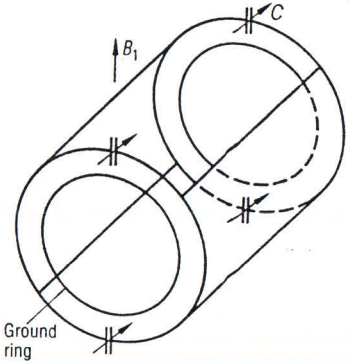

Fig. 10.32
Aldermann-Grant variation of the conductor resonance principle

in the antenna. In the opposite direction, the voltages induced in the resonators by the precessing magnetization, shifted by 90°, are transmitted to the preamplifier via a summation network. This configuration requires only half the RF output to generate a rotating B_1 field and results in a signal-to-noise ratio [10.17] improved by a factor of the square root of two if the Q of the antenna under load conditions (loaded by the subject to be measured) corresponds to that of a comparable linearly polarized configuration. Since a cross section of the human body is more elliptical in shape, the advantages of circular polarization cannot be fully realized in practice.

Surface coils

As the name indicates, these coils are used for imaging organs located close to the surface of the patient's body. They are placed on the patient directly over the position at which the organ is located. The coil must be oriented so that the B_1 field is perpendicular to B_0. In the simplest case, the coil comprises

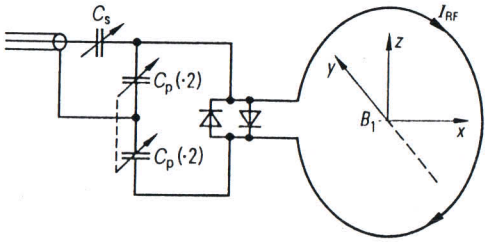

Fig. 10.33
Surface coil with symmetrical matching network

a single wire ring which is tuned to resonance at ω_0 via variable capacitors (Fig. 10.33). The field distribution of a current-carrying circular loop with radius r is described along the y axis of the coil by the following equation:

$$B_i(y) = \frac{\mu_0 r^2}{2(r^2 + y^2)^{3/2}}. \qquad (10.48)$$

The sensitivity along the coil axis and also the remaining field about the wire loop decreases rapidly with increasing distance between the subject and the coil plane. Experience shows that the effective penetration depth is approximately equal to the radius of the coil. In addition, B_i decreases as the radius increases. Depending upon the imaging objective, it is possible in general terms to trade sensitivity for the magnitude of the useful volume by varying the dimensions of the coil. The configuration of the coil windings can also be adapted to the surface of the human body. Surface coils are generally used only to receive MR signals, because of the inhomogeneity of the field distribution. Whole-body resonators are used for uniform excitation. The surface coil may not oscillate

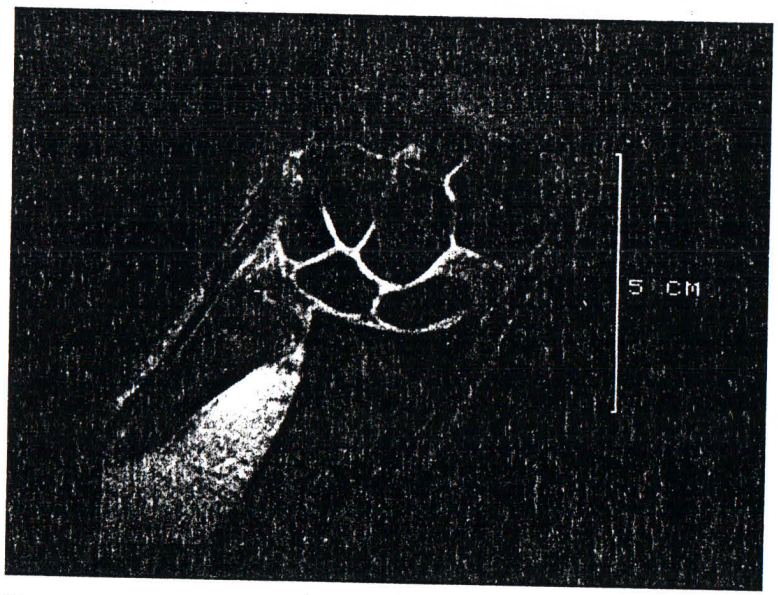

Fig. 10.34
High-resolution MR image of a wrist with carpal bones and ulna, taken with a surface coil
(pixel size: 0.5 mm, $T_r = 0.65$ s, $T_E = 10$ ms, slice thickness: 4 mm, measurement time: 2.5 min, field strength: 1.5 T)

during the transmit phase, since the distribution of the transmitter field would then be distorted. Complete decoupling through the appropriate orientation of the surface coil to the direction of polarization of the transmission antenna is not usually possible. Decoupling is therefore forced via the detuning diodes illustrated in Fig. 10.33; these diodes are switched into the conductive state by the induced voltage.

Figure 10.34 shows the high resolution in MR images which can be obtained using surface coils.

RF-shielded room

Effective antenna shielding against RF interference is essential, because of the extreme sensitivity of the receiving system to high-frequency fields. Antenna sensitivity, self-shielding capacity (a function of the length and diameter of the antenna resonator) and estimates of the intensity of possible RF interference (e.g., short-wave broadcasting stations) must all be included in the calculation of the required attenuation factor.

Experience has shown that the shielding factor must be greater than 100 dB to prevent interference from a 5 kW single-frequency transmitter at a distance of 10 km. In order to obtain such shielding the receiving antenna must be inside a metal housing, which is, for all practical purposes, completely closed. An extension of the shielding tube [10.18] in which the antenna is located, a practice seen occasionally, can only be effective in areas completely free of interference and when using low frequencies. Since high-frequency magnetic fields can hardly penetrate conductive material due to the skin effect, electrostatic shielding of a thickness of several times the skin depth is sufficient (e.g., 0.5 mm copper foil). Gaps in the shielding are to be avoided if possible. If necessary, however, the linear dimensions of such gaps must be clearly smaller than those of the wavelength corresponding to the MR frequency. Doors must be constructed so that they are RF-proof when closed. In general, the entire field generation system, i.e. the magnet, shim, gradient and RF coils and the patient table must all be set up inside the shielded room (see Fig. 10.1). This means that all the cables for these components must be routed through appropriately dimensioned suppression filters. Otherwise these cables, which are excellent antennas for high-frequency interference, would conduct RF noise into the shielded room.

If even these extensive measures are insufficient (in the case of a high-powered short-wave transmitter in the area), the constant field must be changed to provide for sufficient distance between the frequency band used for MR imaging and that of the interference.

10.2.4 System control

Processor systems for examination sequence, monitoring and image reconstruction

Alongside the central system computer, for which the tasks were already listed in Sect. 10.1, the MAGNETOM MRI system, for example, includes a number of additional processors, which control the pulse sequence, reconstruct images from raw data and initiate, as well as monitor, the correct functioning of all essential system components. This decentralization of computer tasks frees the system computer in particular from those operations which depend critically on time. In view of the significance of such a structuring for MR imaging, the function of the pulse sequence control will be dealt with in greater detail in the following. The image processor and also the image display units correspond to the system employed in x-ray computed tomography. The tasks assigned to the other control processors (Table 10.5) are comparatively trivial.

Table 10.5 Tasks of the monitoring processors

Function	Implemented in function module					
	Table	RF antenna control	RF power amplifier	RF small signal part	gradient amplifier	shim current power supply
Remote control on/off switch	×	×	×	×	×	×
Special switch-on procedure			×		×	
Self-testing routine	×	×	×	×	×	×
Electrical overloading			×		×	×
Thermal overloading (cooling)			×		×	×
Special functions	Table lift, table positioning, light localizer	Antenna switching, automatic tuning	Frequency and power range switching	Attenuator and gain switching, synthesizer frequency	None	Shim currents

Pulse sequence control

Fig. 10.35 shows a schematic diagram of the pulse sequence control. The procedure to be executed is present before the beginning of the measurement in the form of control words in the control memory. The bit pattern transferred from here by means of a control logic to the control word register determines what takes place in the corresponding time slice: this may be a gradient pulse, an RF pulse, a data acquisition interval, a delay time or several such events simultaneously. The control word only initiates the functions programmed, which are then executed independently under the control of programmed trigger pulse generators; that is, according to their clock speeds, the data present in the pulse shape memories are transmitted to the DACs or the MR signals are sampled. The image processor receives the measured data directly from the two ADCs and processes them to image data. The pulse data must, just as for the control word sequence before beginning the measurement, already be present in the memories. The same applies for the trigger pulse programs used to determine the time scale for the individual parts of the sequence. The

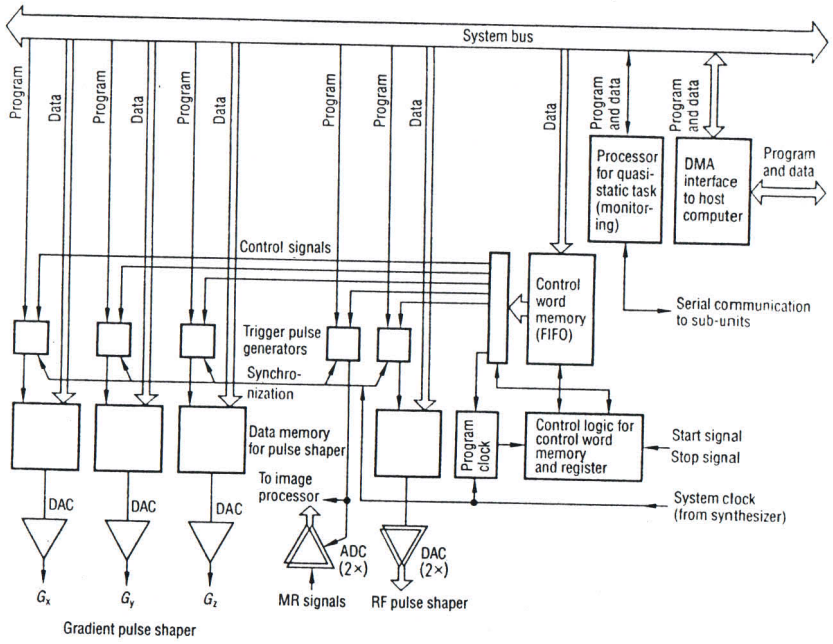

Fig. 10.35 Schematic diagram of pulse sequence control

entire sequence is synchronized from the frequency synthesizer, which serves as the system clock.

This control structure has the property that a control operation; that is, reading and decoding a control word, must only be initiated for each sequence function block and not for each change of an output value. The control word memory can therefore be relatively small. By comparison, the pulse shape data memories are generously dimensioned in order to support long pulse sequences comprising several different pulses.

The pulse sequence control is integrated into a microcomputer system, for which Fig. 10.35 shows only the general data flow path (system bus).

The system computer is connected via an interface with direct memory access (DMA) to the control and supplies the machine language program for the pulse sequence selected, in the form of data which the microprocessor makes available to the appropriate memories.

In the event of insufficient memory capacity, the microprocessor can load data from the backup buffer memories during the measurement process.

Operating program

In an imaging system which performs both measurement sequences and image reconstruction by means of digital computers, the operating program is of particular importance. Moreover, in normal operation the operating program represents the interface through which the user initiates measuring system functions and retrieves results – usually, images (Fig. 10.36).

The particular properties of the imaging process also clearly affect the software design. By contrast, for example, with x-ray computed tomography, MR imaging as a measuring process is relatively slow. The acquisition of a complete raw data file generally requires several minutes. A necessary consequence of this is that the delay time to accommodate other functions, such as image callup and manipulation, must be filled out. The operating system must therefore be able to perform several tasks quasi-simultaneously. This so-called time sharing capability is in conflict with the requirement of real-time operation during measurement. In spite of the long duration of measurement, there is a high rate of data flow: over the course of a single measurement, data for entire series of images can be acquired. This means that the program must be capable of managing large data files and rapidly accessing certain images. Finally, it must also be mentioned for magnetic resonance tomography that the possibilities for variations in the measuring procedure are greater and depend less on the system configuration than for any other modality. A high-capability dialog system for inputting the parameters of measurement is essential in order to be able to take full advantage of the potential which MRI offers.

The generation of the NUMARIS (Nuclear Magnetic Resonance Imaging Program) operating program for the MAGNETOM takes these points into account. It is able to run on a system computer (DEC-VAX) with the VMS Multitask operating system, which supports the requirement of performing several tasks simultaneously. The general structure of the operating program is shown in Fig. 10.37. According to the task at hand, the function blocks will differ.

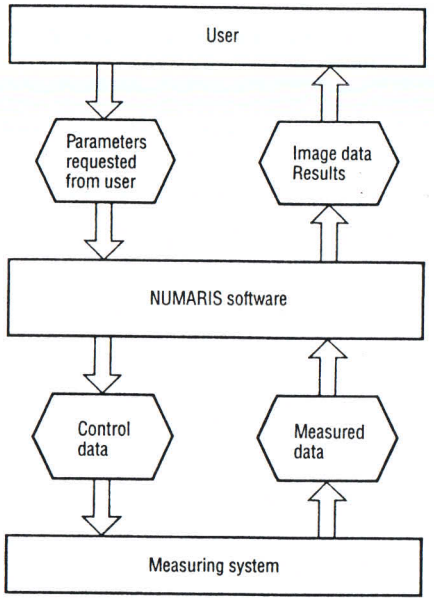

Fig. 10.36
Operating program as interface between user and measuring system

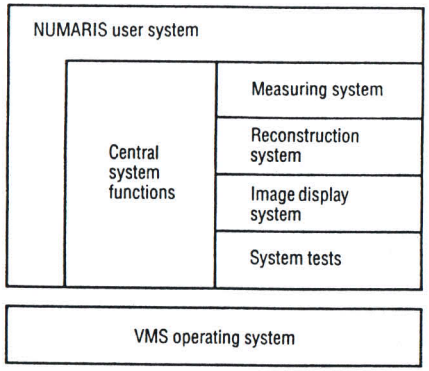

Fig. 10.37
General structure of the NUMARIS operating program

Central system functions:

To these belong process generation (the concept process will be defined more precisely in the following), communication between processes; that is, the transfer of information between processes which depend on each other, coordination of system components, processing of inputs through the operator's keyboard, interpretation of commands and function key codes and the management of the monitor terminal; that is, the assignment of display area to the various processes.

Measuring system:

This comprises the coupling of the system computer to the measurement sequence control, the modification of measurement parameters and the related generation of pulse programs, implementation of settings required and recognition of system status.

Reconstruction system:

This includes the functions of coupling the system computer to the image processor, acquiring measured data, image reconstruction and intermediate storage of measured data and image data files.

Image display system:

To this belong the coupling of the system computer to the image output units, control of image output and presentation (windowing), image evaluation routines, graphics and graphics inputs, and the management of patient and image data (file management).

System test:

This function block is provided for servicing purposes and includes the test routines for all digital components, as well as for adjustments and functional checkouts required in connection with the system installation and optimization.

At the basis of the operating program is the VMS operating system, with functions supporting NUMARIS, in particular during the dynamic assignment of host computer capacity (to take best advantage of the central processing unit and available memory) for processes, as well as for the management of peripheral mass storage devices.

The concept "process" [10.19] means the execution of a task, as well as the provision of the operating means required for performance of the task: computer capacity and programs. Within a process, only a single program can run at any one time, from which it follows that tasks which must be performed simultaneously must be assigned to different processes. A typical time-sharing application, for example, would be the creation of text data files for several users at different video terminals at the same time. For each user, a process is started,

in the framework of which the (same) editor program can run. In this case, the processes would be fully independent of one another. However, in the NUMARIS operating program, the processes form a single system, since they are more or less dependent on each other; that is, they must continuously exchange data and messages among each other. Furthermore, they make use of a common terminal. It would not be meaningful and would only complicate operation if each process had to be operated from a separate input unit.

Distribution of operating functions in processes

Fig. 10.38 shows, in simplified form, the system of processes, their communications paths and the MR system components which they serve. The total number of processes implemented is greater than the number of function blocks described, because interrelated tasks (for example, an adjustment; i.e., specific measurements followed by the immediate calculation of results and control reactions) are combined within a single process and certain partial functions must be able to run together with others from the same block. So far as one or more operator consoles are additionally installed for evaluation tasks on the system, the given processes can be activated several times using identical program segments. The processes communicate with each other through the exchange of messages deposited in so-called mailboxes. The receiving process reads the messages entered and reacts accordingly.

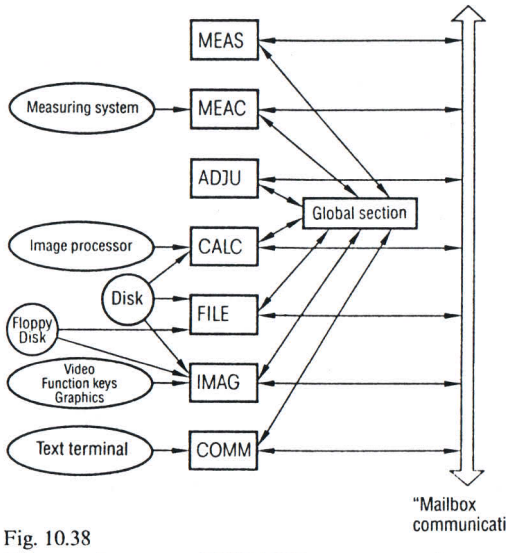

Fig. 10.38
The most important NUMARIS processes and communications paths

Table 10.6 Functions of the important NUMARIS processes

Process name	Process function
COMM[1]	Text terminal management, command input, assignment of text monitor screen into status, error and confirmation message fields and corresponding processor assignment
MEAS	Generation, modification and display of measurement programs (pulse sequences)
MEAC	Transfer of measurement programs to measurement sequence control
ADJU	Measurement programs for subject-dependent system calibration
CALC	Transfer of reconstruction algorithms and measured data or image data files to and from image processor
FILE[1]	Management of peripheral mass storage devices (patient, image and measured data)
IMAG[1]	Image presentation (video memory control), image manipulation, graphics input and output, management of function keys

[1] These processes can run twice in the system when a 2nd satellite console (2nd control console for separate image evaluation) is present.

The processes also obtain information from the common memories (global sections), in which system data of general use, such as system configuration, results of adjustments or conditions of measurement, are entered. Processes not performing a task are switched off in order to relieve the central processing unit of the host computer.

The functions of the NUMARIS processes illustrated in Fig. 10.38 are summarized in Table 10.6.

10.3 Imaging techniques

10.3.1 Subject-dependent system calibrations

After the patient has been positioned, the parameters influenced by the the subject to be measured must be calibrated before the measurement can be started. Calibration procedures for an MR examination are performed as follows:

1. Patient positioning
2. Matching of resonator/coils
3. Setting the MR center frequency
4. Pulse amplitude calibration
5. Selection of measurement parameters (or pulse sequence)
6. Setting the receiver gain
7. Starting the measurement
8. Image reconstruction and image retrieval

Steps 2–4 must be repeated only when the patient has been repositioned. The selection of measurement parameters (step 5) may be performed earlier in this sequence.

Antenna adjustment

The transmit/receive coil impedance, which is dependent on the size and position of the patient, must first be matched to the impedance of the transmission line. With the help of a fully automatic control system the capacitors of the matching network (Fig. 10.27) are set so that there is practically no reflection of the RF power fed into the antenna.

After the desired measurement parameters have been selected, the required procedures described in the following are normally performed automatically by the system.

Setting the center frequency

The next step is the determination of the magnetic resonance frequency. This would seem to be a superfluous step when dealing with the stability of superconducting magnets, but the frequency will change by tens of Hz from patient to patient due to varying susceptibility. A variation in resonance, as shown in Eq. (10.1), would cause a noticeable shift in the image, corresponding to the gradient strength employed. The resonance frequency can be determined by a simple MR experiment, namely the excitation and readout of an FID (free induction decay). The synthesizer is then readjusted accordingly.

Adjustment of pulse amplitude

Since the degree of efficiency of the transmission antenna, expressed in generated B_1 field per square root of the RF power input, is strongly dependent on

the subject under examination, the pulse amplitude must be adjusted. This determines the RF output necessary to tip the nuclear magnetization by an angle α by using a pulse of length t_p. A practical method makes use of the following relationship between transverse magnetization $M_\perp$, which is proportional to the nuclear resonance signal apart from a constant phase factor, and the B_1 amplitude (Fig. 10.39):

$$M_\perp = M_0 \sin(\gamma t_p B_1). \tag{10.49}$$

The first zero passage of the MR signal directly after the RF pulse is sought by increasing the pulse amplitude in a series of FID excitations (Fig. 10.39a), first in larger steps and then in fine steps. The first signal minimum corresponds to a nutation angle of 180°.

Using the pulse length t_p and the amplitude determined during calibration, the scale factor of any other pulse shape of known effective length can be computed.

Receiver gain

The last step in the calibration process is the adjustment of receiver gain with respect to the maximum MR signal occurring during imaging. The importance of this adjustment is discussed in section 10.2.3. The same pulse sequence is used for the measurement as for the following imaging, except for the fact that the phase encoding gradient is not switched on, because the MR signal is at its maximum in this case. For this reason, with few exceptions – such as the size of the field of view, the pulse sequence parameters must be selected prior to this step.

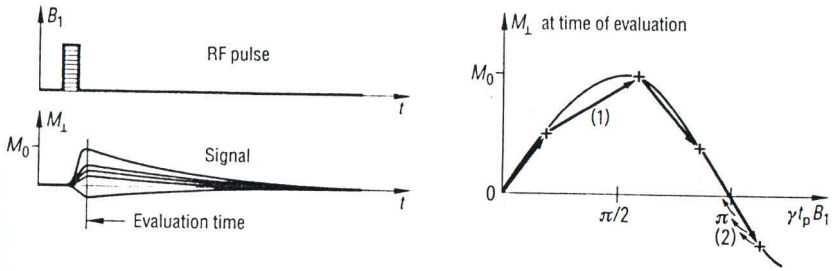

a) Measuring sequence for amplitude calibration

b) Dependence of resonance signal on B_1 amplitude

Fig. 10.39
Pulse amplitude calibration procedure. The condition $\gamma t_p B_1 = \pi$ is first attained in coarse steps (1) up to the sign reversal of $M_\perp$ and then in fine steps (2) up to the signal minimum

If no overload has occurred, the resulting measurement data can be used to calculate the amplifier settings necessary for proper modulation of the receiving components. If this is not the case, the calibration measurement must be repeated using reduced gain.

10.3.2 Spin-echo pulse sequences

Due to its relative insensitivity to inhomogeneities in the static constant field and to other imprecisions of the measuring system and also because of the easily characterized dependence of the resulting image contrast on the parameters echo time, T_e, and pulse repetition time, T_r, the spin-echo sequence remains the most widely used pulse sequence for MR imaging:

$$S \sim \varrho e^{-T_e/T_2}(1 - e^{-T_r/T_1}). \tag{10.50}$$

$$T_e \ll T_1$$

$$T_2 \ll T_r.$$

The underlying principle is described in section 5.2.3, while the form for the individual parts of the sequence was discussed in connection with the gradient strength (see Sect. 10.2.2). In the following, a few variations will be dealt with. Multiple-echo imaging for the production of a series of images with different T_2 weighting and the problems resulting will also be discussed.

Sequences with one spin-echo

The pulse sequence is again illustrated schematically in Fig. 10.40a, without taking the gradient switching times into account. Fig. 10.40b shows the path

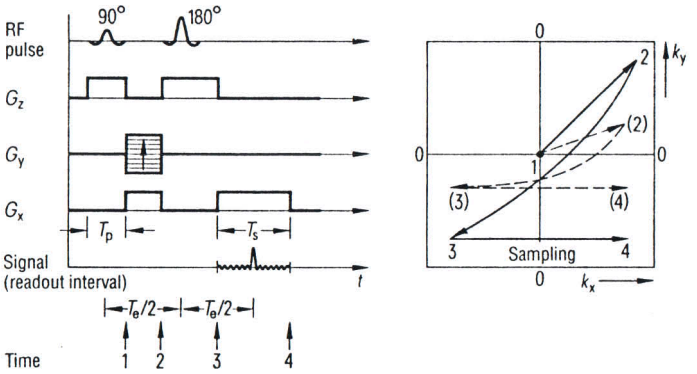

a) Pulse sequence

b) Sampling in k space

Fig. 10.40 Simple spin-echo pulse sequence

over which the plane of spatial frequencies, represented by the measured MR signals, runs. In the following, this plane is referred to as the k plane, or in the three-dimensional extension, as the k space:

$$k_x = \gamma G_x t_x; \quad k_y = \gamma G_y t_y. \tag{10.51}$$

For each 90° – 180° pulse pair; that is, for each repetition interval T_r, a Fourier projection is acquired through changing the strength of the phase encoding gradient, G_y, in equidistant steps and stored in the measured data matrix, until all four quadrants are fully occupied. The reconstruction to an MR image then takes place through the Fourier transform following and the modulus values are then calculated in order to eliminate phase factors of the form $e^{i\varphi(x,y)}$. This is permissible, because the imaginary part of the object function vanishes for the symmetric sampling of four quadrants [10.20]. The phase factors are essentially the result of incomplete diagonalization of the measured data in the k matrix, particularly in the readout direction, due to the generally non-ideal gradient pulse shape. The entire spatial information is already contained in two quadrants, so that the measurement can be terminated after the acquisition of one half of the k plane. The other half is then filled with zeroes. From the complex result of the reconstruction, it is then necessary to extract the real part; due to the determination of phase factors required for this task, this process is generally problematic [10.21]. Halving the time of measurement is of course only possible at the expense of accepting a decrease in the signal-to-noise ratio by a factor of at least $\sqrt{2}$.

For the sequencing of gradient pulses there are various possibilities, as Fig. 10.41 illustrates: thus, the refocussing of the selection gradient can be placed before the 180° pulse (a) or the preparation period; that is, defocussing in the readout

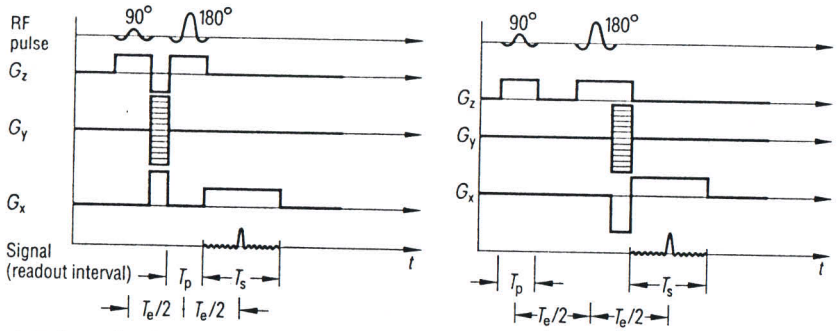

a) Refocussing before the 180° pulse

b) Defocussing following the 180° pulse

Fig. 10.41 Variations of the spin-echo sequence

direction and phase encoding, can follow upon the 180° pulse (b). The first variation permits a shorter echo time, T_e, provided that there is sufficient reserve in the gradient strength and switching time and that $T_p < T_s$. The second variation has the advantage that the phase encoding is also effective with respect to the signals induced by the 180° pulse, referred to in the following as the residual FID. As a result of its finite pulse length, the 180° pulse cannot bring about even an approximately homogeneous inversion of the magnetization, $M = (M_x, M_y, M_z)$, over the entire slice thickness. Furthermore, the B_1 inhomogeneity and the finite pulse calibration error also give rise to deviations from the ideal case. Since the buildup of M_z with the time constant T_1 already becomes noticeable within the time $T_e/2$, the 180° pulse can cause measurable transverse magnetization. If the phase encoding for these signal components is missing (as for the sequence in Figs. 10.40a and 10.41a), a disturbance in the form of a streak artifact is seen in the middle of the image field, in the direction of the readout gradient (x).

Through the alternation of the sign for the 180° pulse with every second Fourier projection, it is nevertheless possible to shift this streak to the edge of the image field, where it no longer represents a disturbance, but not to eliminate it altogether. The periodic alternation of signs modulates the residual FID with the highest frequency which can be represented in the sampling grid in y. This corresponds to the outermost lying position in the y direction. Still better is to alternate the 90° pulses and to take into account the changes in sign of the spin echo during image reconstruction. This also eliminates any offset error of the ADC, which would otherwise be reconstructed to a point in the middle of the image.

The variation depicted in Fig. 10.41b therefore appears less attractive for single echo sequences.

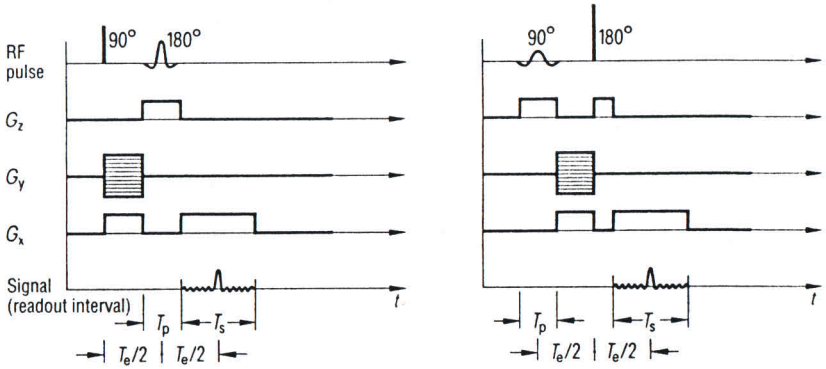

a) 90° pulse (nonselective)

b) 180° pulse (nonselective)

Fig. 10.42 Variations of the spin-echo sequence with a nonselective RF pulse

In the interest of shortening, the echo time, one of the two RF pulses can be made nonselective: either the 90° pulse in Fig. 10.42a or the 180° pulse in Fig. 10.42b. But with this the multislice capability is lost. The version with the nonselective 90° pulse is preferable, because there is no switching process for G_z or the – mostly very intense – residual FID, which is excited from the nonselective 180° pulse acting over the entire object. The minimum T_e time possible is then reduced by T_p.

These represent the most important variations of the spin-echo pulse sequence.

In summary, the most important rules for designing such a sequence are as follows:

1. Symmetry rule: The time integrals of the gradient pulse from the middle of the 90° pulse to the middle of the 180° pulse should agree with those from the middle of the 180° pulse to the middle of the readout interval. This is equivalent to occurring at the same point in time as the spin-echo maximum, with and without gradient pulses, and brings about a complete refocussing of the phase dispersion resulting from field inhomogeneities and the chemical shift. This condition remains satisfied once a pulse sequence has been optimized for different gradient strengths when the gradient switching time is constant instead of the switching speed.

2. With the RF pulse, only one (generally constant) gradient field may act; otherwise, a rotation of the slice normals will take place in the direction of the gradient vector sum.

3. During readout, only a constant gradient field may be switched on; otherwise, a rotated or distorted image will result.

4. Pulse time and pulse bandwidth: The pulse bandwidth, $\Delta\omega_p$, together with G_z, determines the slice thickness and the necessary RF power. The slice profile sharpness is essentially a function of the product $\Delta\omega_p T_p$.

5. Readout time: Together with G_x and G_y, this determines the pixel size, the relative distortion due to field inhomogeneities and the chemical shift, and the signal-to-noise ratio.

Multiecho sequences

The single-echo pulse sequence can be extended through the addition of further – to maintain the multislice capability, preferably selective 180° pulses and readout intervals (Fig. 10.43a) – to a multiecho sequence. Fig. 10.43b shows the associated sampling path in the k plane. As can be seen, the phase reversal through the 180° pulse causes the spatial frequency matrix, and thus the image matrix for each even echo, to be the mirror image of the odd echoes about $y=0$. The reconstructed images are, according to Eq. (10.50), increasingly T_2-weighted with increasing echo number. Examples of this can be seen in Section 5.2.4, Fig. 5.22. In practice, however, such a simple extension does not

function satisfactorily; that is, interference from mirror images and superimposed structures, with the formation of wave patterns, and streak artifacts occur. The cause, as for the residual FID, is to be found in the unavoidable incompleteness of the 180° pulse. Within a pulse sequence, as soon as more than one further RF pulse with a nutation angle not equal to 180° follows an excitation pulse, along with the desired echo for the T_2 determination for each readout interval spurious echos and stimulated echos also appear [10.22]. A detailed account of these rather complex relationships is not possible in this context. A descriptive explanation for the spurious echos is the following: each RF pulse in the sequence can form an excitation pulse or refocussing pair with each following pulse, just as for the normal single-echo sequence. The intensity of these spurious echos depends on the values of both relaxation times and also on the deviation of the pulse angle from its theoretical value (90° or 180°). The number of spurious echos increases strongly with the number of RF pulses, since each echo can in turn be refocussed through the following pulses. After only the second 180° pulse, two spurious echos can already appear with the second echo.

The origin of stimulated echos can be visualized as follows: the second RF pulse folds a part of the magnetization, dephased due to constant field inhomogeneities (the inhomogeneities introduced intentionally through the spatially coding gradients also belong to these), into the xz or yz plane of the coordinate system, which rotates with ω_0. As a result of T_2 relaxation and field inhomogeneities, this part loses its phase coherence in the transverse (xy) direction, so that after a certain time the magnetization executes a conically shaped precession, at an angle corresponding to the dephasing which has occurred up to the second RF pulse. This means that, except for the part which – as a result

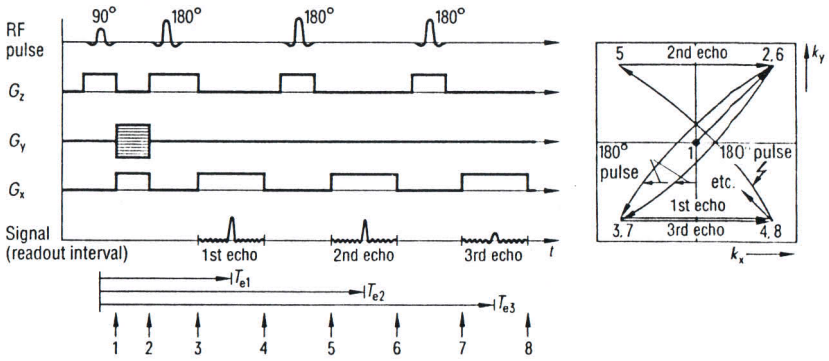

a) Pulse sequence b) Sampling in k space

Fig. 10.43
Multiecho sequence. Even and odd echos belong to the corresponding Fourier projection

of T_1 relaxation – vanishes into M_z; the magnetization "remembers" the phase angle. The third RF pulse then folds the magnetization again, at least partially, into the xy plane, where it is refocussed and forms the stimulated echo. For the purposes of imaging technology, this can be summarized in the form a rule of thumb:

The stimulated echo generated by three RF pulses does not "see" the effect of the static fields over the time between the second and third RF pulses.

Stimulated echos are generated from any three non-180° RF pulse series; through further pulses, they can form new ordinary echos and spurious echos. In view of this, it appears questionable whether it is possible at all to obtain meaningful multiecho images from this utter confusion of echos, spurious echos and stimulated echos, together with the residual FID.

Fortunately, for the greatest part of the undesirable echos, for even the simplest multiecho sequence, as shown in Figure 10.43, no phase encoding of the spatial dimension y takes place, nor is the refocussing condition in the slice (z) direction or the readout (x) direction satisfied. All signal components not subject to the phase encoding give rise to a streak artifact, corresponding to object extension in the x direction. As for the single-echo sequence, this can be displaced to the edge of the image through alternating the signs of the 90° pulse.

The occurrence of mirror images is explained most easily with the aid of the rule developed above: this says that the stimulated echo signal (STE) does not take part in the mirror imaging of a point, caused by the (second) 180° pulse. In [10.23], without introducing the concept of an STE, the intensity of the mirror image for the second echo is given quantitatively as a function of the pulse angle error. It can be largely eliminated through addition (even echos) or subtraction (odd echos) of the signals from every two measurements for each Fourier projection, which differ only by a 90° phase shift of the 180° pulse (PHAPS sequence). However, this requires – among other things – that the normal spin echo appear at the same time as the STE. Otherwise, through the superposition of images arising from the partial signals, wave patterns will result in accordance with the known rules of Fourier transformations [10.20]. Their occurrence at the same moment in time is guaranteed by satisfying a symmetry rule, which – its meaning extended to the STE and the second echo – can be derived from the rule given for the creation of single-echo sequences: the difference of the time integrals of the readout gradients (G_x) before the first and after the second 180° pulse up to the echo must be equal to their sum minus the G_x integral between the two pulses. Such a pulse sequence can be programmed easily, as long as the G_x pulses are in the ideal trapezoid shape. Nevertheless, the smallest deviations – such as due to insufficient eddy current compensation – are already problematic.

One possibility, related to the PHAPS sequence, should be mentioned without further explanation: the suppression of the mirror image-generating STE at least for the echos of order not equal to $4n+2 (n=0, 1, 2, \ldots)$. This makes the

twofold measurement of each Fourier projection unnecessary. Each two 180° refocussing pulses following each other in this sequence are rotated by 90° in their phase. The method is also sensitive to minute inaccuracies of the refocussing and defocussing gradients.

Owing to these difficulties, other variations of the multiecho sequence have also been developed. One of these makes a virtue of violating the symmetry rule mentioned earlier. The duration of the readout gradient is set so that the interfering signals occur outside the readout interval. Alternatively, or in addition, the slice selection gradient is extended by the third and further 180° pulses in such a way that the undesired echos are defocussed and no longer contribute to the image [10.25]. Figure 10.44 shows such a pulse sequence. Since the number of interfering echos for which the refocussing condition must be violated increases with the number of RF pulses, the required time integrals of the gradients around the 180° pulse become increasingly large with increasing echo number. This means that the application of this strategy is practically limited to sequences of no more than about four echos.

It must be mentioned that a completely exact T_2 determination is not possible with any of the methods described. Either, according to the distribution of the flip angle for nuclear magnetization over the slice, a more or less definite admixture of T_1 values, i.e. the time constants describing the STE relaxation, is always present in the image signal or the signal is reduced due to incomplete refocussing.

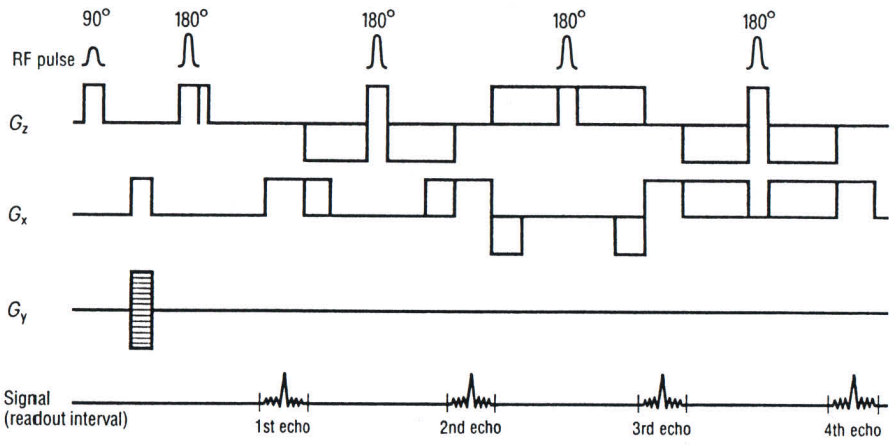

Figure 10.44
Multiecho sequence with dephasing and displacement of undesirable spurious echos (gray areas of the gradient pulse)

10.3.3 Fast MR imaging methods

The production of an MR image of sufficient spatial resolution and with an acceptable field of view with the spin-echo sequences described requires a few minutes; that is, at least the repetition time, T_r, times the number of Fourier projections, N.

Particularly for examinations of the thorax and abdomen, with their unavoidable involuntary movements, it is essential that the time of measurement be shortened. Two main methods are known today for achieving this goal. One of these is to reduce T_r as far as possible and so – through appropriate structuring of the sequence – to optimize the measurable transverse magnetization and thus the signal. The other possibility is, within the T_r interval; that is, beginning with a 90° excitation pulse, to acquire as many measurement points from the k matrix as possible at once.

Sequences with extremely short T_r times

Through a reduction of the pulse repetition time to below 0.3 s, the necessary conditions cited for using Eq. (10.50) are no longer satisfied sufficiently. Beginning with the formula of Ernst and Anderson [10.26] for equilibrium magnetization induced by periodic excitation with RF pulses of nutation angle α, for $T_2 \ll T_r$ the relation

$$M_L = M_0 \frac{(1-e^{-T_r/T_1}) \sin \alpha}{1-\cos \alpha e^{-T_r/T_1}} e^{-T_e/T_2} \text{ results.} \qquad (10.52)$$

As a result of the inadequacies described in Section 10.3.2, the refocussing of the magnetization with a 180° pulse leads to unpredictable complications

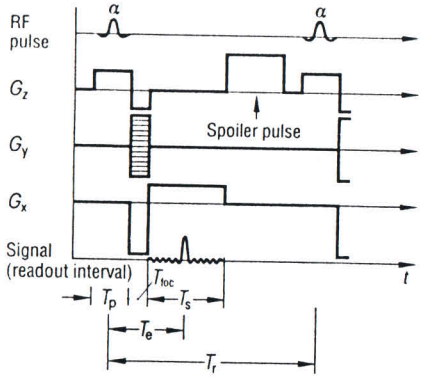

Fig. 10.45
FLASH sequence

with the method. The generation of the echo signal therefore follows without a 180° pulse through gradient polarity reversal in the slice and readout directions. The resulting MR signal is therefore known as the gradient echo. Figure 10.45 illustrates such a pulse sequence. Because of the missing 180° pulse, the minimum possible echo time is considerably shorter than for the spin-echo sequence. However, a dephasing of the spins due to B_0 field inhomogeneities and the chemical shift is not compensated. The signal intensity is then really dependent on T_2^* (see Section 5.1.5) and not on T_2. Since the transverse magnetization at the end of the readout interval, especially with extremely short T_r times ($T_e \leq 2T_r < T_2$), is generally still of a significant magnitude, a so-called spoiler pulse; that is, a gradient pulse having a large $t \cdot G_z$ product, is appended to the sequence in order to disperse the magnetization in the direction of the slice as completely as possible. This is done to at least satisfy the condition $T_2^* \ll T_r$.

As follows from Eq. (10.52), the signal intensity for this pulse sequence depends, in addition to its time data in relation to the relaxation times, on the nutation angle of the excitation pulse as well. One therefore has an additional parameter available, with which the signal-to-noise ratio or the image contrast can be optimally adjusted. The relation between the magnetization in equilibrium, determining the signal strength, and the ratio T_r/T_1 is shown in Fig. 10.46 for a few pulse angles. The pulse angle for the maximum signal is:

$$\alpha = \arccos(e^{-T_r/T_1}). \qquad (10.53)$$

This means that, for long spin-lattice relaxation times (compared with the time T_r) weak RF pulses yield the largest – relative – signal. Following a suggestion

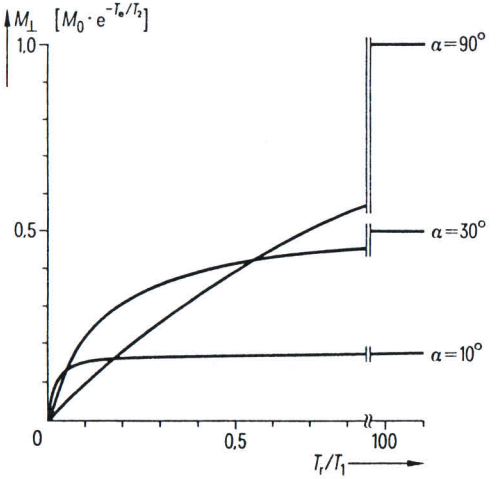

Fig. 10.46
MR signal for the FLASH sequence as a function of T_r/T_1 for different pulse angles, α (note that for relatively short repetition times, T_r, small pulse angles, α, yield a greater signal than large angles)

in [10.27], this sequence is given the name FLASH (Fast Low Angle SHot), because, for the short T_r times, the T_1 times of body tissue needed for an optimal signal-to-noise ratio require a pulse angle much smaller than 90° (usually 20–60°). The minimum total time of measurement is about 10 s for 256 Fourier projections.

Another possibility to obtain a relatively high equilibrium level transverse magnetization, in spite of very short pulse repetition times, is to bring about a complete rephasing of the spin in the RF pulses. Instead of the spoiler pulse of the gradient-echo sequence, refocussing gradient pulses occur in both the readout and also the phase encoding and selection directions, as can be seen in Fig. 10.47. The RF pulses alternate in sign. For signal behavior, the following equation [10.28], taken from Ernst and Anderson [10.26] and making use of the approximation $e^{-T_r/T_1} = 1 - T_r/T_1$ with $T_1 \gg T_r$ (and similarly for T_2) is generally given. This is the equation of Steady State Free Precession (SSFP):

$$M_\perp = M_0 \frac{\sin \alpha}{1 + T_1/T_2 + (1 - T_1/T_2) \cos \alpha}. \qquad (10.54)$$

In practice, though, it is found that for a non-homogeneous field the dynamic equilibrium described is not distributed uniformly over the object of measurement; this can lead to very disturbing image artifacts. A better result is achieved when the pulse sequence shown in Fig. 10.47 is modified by removing the gradient pulses marked in gray. Such a sequence is known by the name FISP (Fast Imaging with Steady Precession). Here, only the phase encoding is compensated. Otherwise, this sequence differs from the FLASH sequence only through the missing spoiler pulse. The image signal, which is a function of T_1, T_2 and α, behaves qualitatively in a way similar to that described by Eq. (10.54): object regions with $T_1 = T_2$, such as aqueous body fluids, are imaged bright, in particular when $\alpha = 90°$. The exact signal behavior can be derived from the equations given in [10.26] through averaging of the magnetization as a function of the angle of precession, α, over a volume element [10.29].

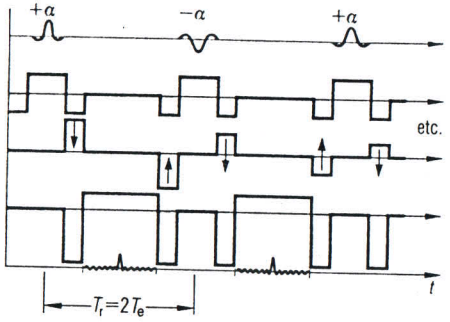

Fig. 10.47
SSFP pulse sequence.
The FISP sequence is obtained by omitting the gradient pulses (shown in gray)

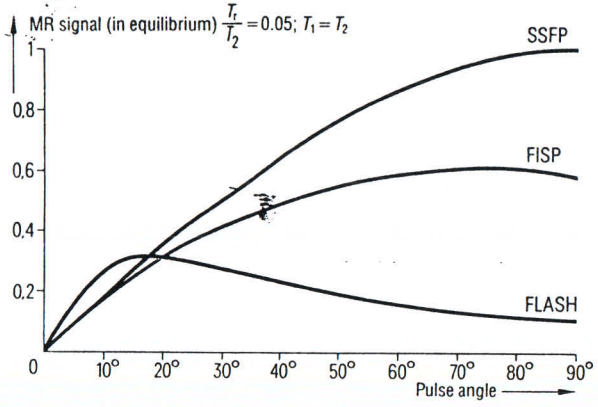

Fig. 10.48
FISP signal as a function of the pulse angle, α, compared with FLASH and SSFP signals
(Source: Dr. Oppelt)

Figure 10.48 gives the FISP signal as a function of α, calculated in this way, in comparison with FLASH and SSFP.

Thanks to their fast repetition rates, both methods permit the use of three-dimensional sampling with a high spatial resolution over an acceptable time of measurement: for example, 128 × 256 × 256 data acquisitions in about 13 min. For this, the slice gradient, G_z, is switched in stepwise – for each Fourier plane acquired – for phase encoding of the third dimension. Figure 10.49 shows sagittal head scans from three-dimensional data files measured with FLASH and with FISP sequences. In the FISP image (a) the "low viscosity" regions (edema about the solid tumor and liquor) are clearly brighter, whereas the FLASH image (b) shows approximately the contrast behavior of a T_1-weighted spin-echo image, with its typical demarcation between gray and white brain matter. Impressive is the outstanding signal-to-noise ratio, in spite of very small volume elements.

Echoplanar methods

The basic idea, which accounts for designating those methods described below "echoplanar imaging" [10.30], consists of the following: after a single selective RF excitation to produce a series of spin echos or gradient echos in the readout gradient (G_x), the different lines in the k plane are ordered with the help of a suitable modulation of the phase encoding gradient (G_y). The readout of the echo sequence must be completed within a time, the order of magnitude of which does not exceed T_2 or T_2^*: the decay of the transverse magnetization causes, in addition to a signal loss, a weighting of the Fourier projections in accordance with the order of their acquisition, so that an undesirable anisotropic change in the modulation transfer function would then result in the phase encoding direction. Figure 10.50a shows the echoplanar pulse

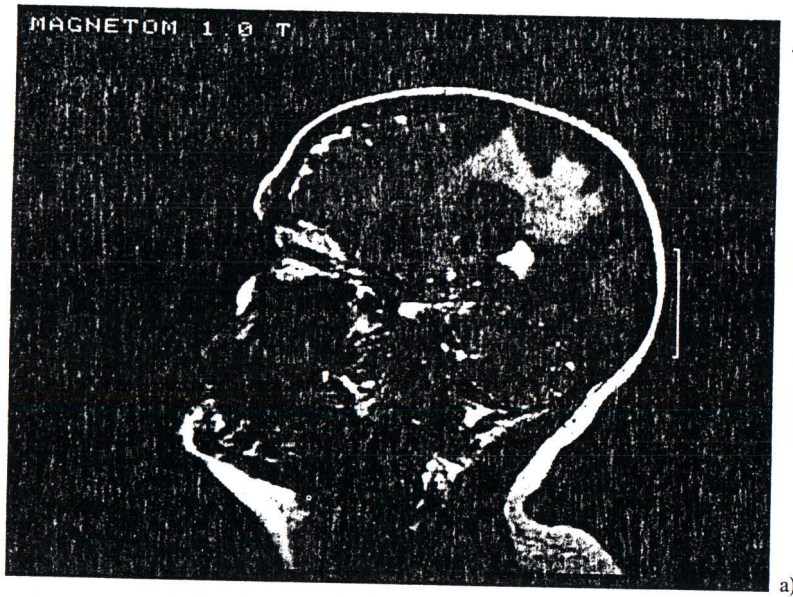

a)

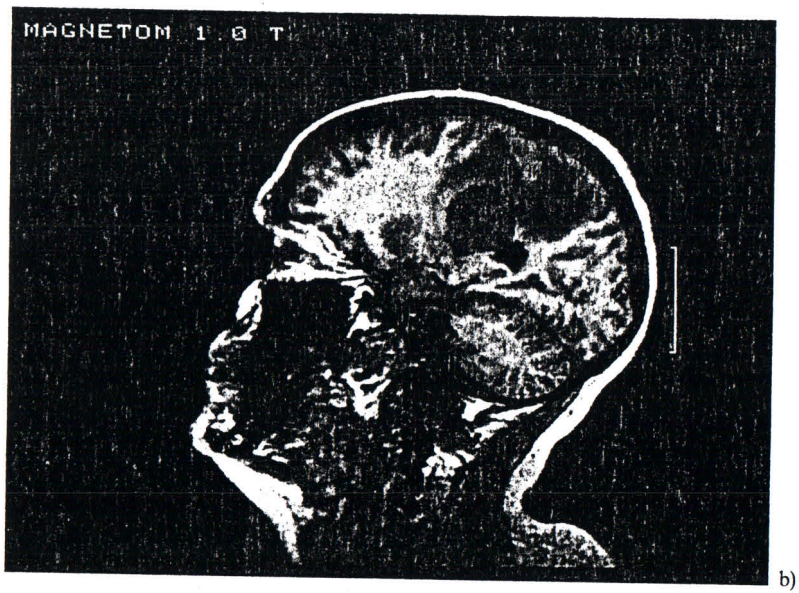

b)

Fig. 10.49
Sagittal head scan from a FISP image (a), showing bright low-viscosity regions, and from a FLASH image (b), with typical delineation of gray and white brain matter

sequence described in [10.30] in a slightly modified form. The needle-shaped G_y pulses in the switching intervals give rise to the meandering passes through the spatial frequency matrix (Fig. 10.30b), so that the sampling points are made to occur equidistantly. Every other time function of the x or y gradient (among others, a sine-shaped G_x modulation and/or a constant G_y have been proposed) fundamentally leads to a non-uniform occupation of the k plane for sampling equidistantly in time. For the image reconstruction a Fourier transformation is then no longer sufficient, and it becomes necessary to make use of either interpolative matrix regeneration or more general integral transformations. If the requirements placed on the field of view or the spatial resolution are not too demanding, it is possible to sample the spatial frequency half-space with one "shot". In accordance with Eq. (10.26), for a pixel size of 5 mm and a pulse flat top length of 1 ms, a gradient strength of 4.7 mT/m is necessary. For a gradient polarity reversal time of 1 ms, about 70 ms would be necessary for the acquisition of measurement data for an image of 64×64 pixels. If one wishes, however, to obtain the level of resolution and pixel number known from spin-echo sequences, the demands on the gradient system rapidly overstep the limits imposed by technological feasibility. This is particularly true for the switching times, which act parasitically. This is the main reason why the echo-planar method has, in practice, not become established in MRI, even though for the optimum choice of T_e or T_s relative to T_2 it is the equal of the spin-echo method in terms of the signal-to-noise ratio per square root of the total data acquisition time ($N \cdot T_s$).

The technical problems just described can be avoided if, for each excitation pulse, only a few Fourier projections are acquired at the same time. These

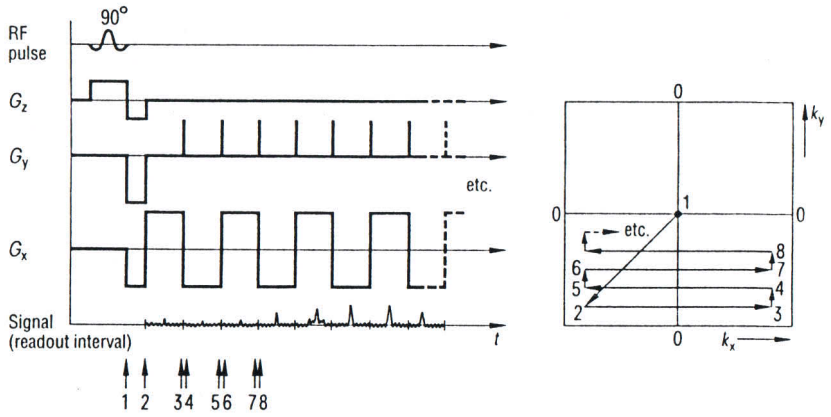

a) Pulse sequence

b) Sampling path in k space

Fig. 10.50 Echoplanar pulse sequence

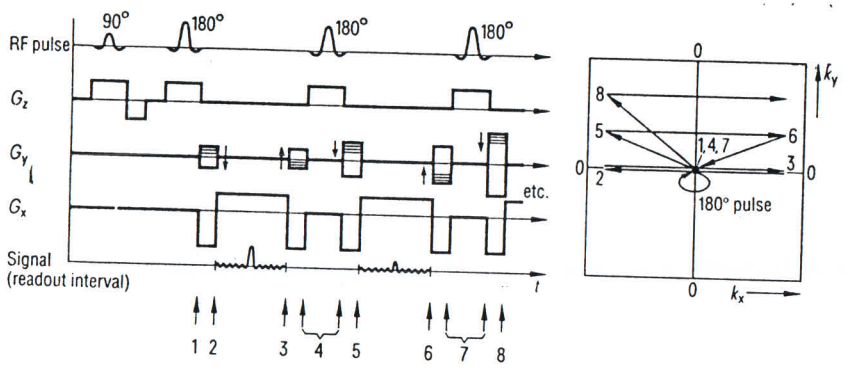

a) Pulse sequence b) Sampling path

Fig. 10.51
Modified echoplanar pulse sequence for a small number of Fourier projections with 180° pulses

so-called hybrid methods reduce the minimum time of measurement and the number of echo signals acquired over each T_r interval. Under certain conditions, 180° pulses can again be introduced to generate echos [10.31], so that a refocussing of the constant field inhomogeneities takes place. Figure 10.51 shows such a pulse sequence and its sampling path in the k plane. A phase encoding performed periodically at the echo position would not be suitable, because this would cause a repeating amplitude modulation of the form e^{-nT_e/T_2}, corresponding to each Fourier line, for each excitation pulse. The reconstructed image would then show a multiply imaged object. The phase encoding of each echo must be performed in such a way as to define a monotonic relationship between the T_2 weighting and the spatial frequency.

In addition to the examples of echoplanar methods described here, there are also other variations [10.32]; however, their description would go beyond the framework of our present discussion.

10.3.4 MR angiography

Apart from T_1, T_2 and the spin density, ϱ, magnetic resonance tomography also offers the possibility of using the velocity of the excited spins as an imaging parameter (see section 5.2.5). This opens the way to a fully new and medically significant field, namely the non-invasive presentation of vascular structures, known as MR angiography. This method, which has already proven itself through a series of clinical studies, will now be presented in detail.

Principle

Equation (10.50) characterizes the signal from a normal spin-echo sequence. We assume that the excited spins do not undergo motion relative to the magnetic field gradient. If this is not the case, then the MR signal will deviate more or less from that given by Eq. (10.50). Motion artifacts or flow artifacts will also occur [10.33], which complicate the interpretation of the MR image or – especially for high flow velocities – prevent evaluation altogether. In order to understand the change in signal intensity with nonstationary spins, it is necessary to examine the development of the phase for the transverse magnetization over time within a volume element. In its general form, this is given by:

$$\varphi(t)=\gamma\int_0^t \vec{G}(t')\,\vec{r}(t')\,\mathrm{d}t'. \tag{10.55}$$

Here, $\vec{G}$ is the magnetic field gradient vector and $\vec{r}$ the – usually – time-dependent position vector. For motion in the direction of a gradient, it then follows that:

$$\varphi(t)=\gamma\int_0^t G_x(t')\,x(t')\,\mathrm{d}t'. \tag{10.56}$$

Expanding $x(t)$ in a Taylor series,

$$x(t)=x_0+\frac{\mathrm{d}x}{\mathrm{d}t}(t-t_0)+\tfrac{1}{2}\frac{\mathrm{d}^2x}{\mathrm{d}t^2}(t-t_0)^2+\ \ldots, \tag{10.57}$$

it is then possible to represent Eq. (10.56) in the following form:

$$\varphi(t)=\varphi_0(t)+\varphi_v(t)+\varphi_b(t), \tag{10.58}$$

where

$$\varphi_0(t)=\gamma x_0\int_0^t G_x(t')\,\mathrm{d}t',$$

$$\varphi_v(t)=\gamma v\int_0^t G(t')\,t'\,\mathrm{d}t$$

and

$$\varphi_a(t)=\tfrac{1}{2}\gamma_a\int_0^t G(t')\,t^2\,\mathrm{d}t',$$

in which the point t_0 can be set to zero without any limitations and the first and second spatial derivatives correspond to the velocity, v, and the acceleration, a, respectively. The first term, $\varphi_0(t)$, in Eq. (10.58), describes the dependence

of the phase on the spin position x_0. The maximum phase coherence occurs at a zero of the time integral over G_x. This is the case at the time at which the spin echo appears. The other terms give rise, through motion at constant velocity and accelerated motion of the spin during the measurement, to additional phase contributions.

As an example, if we examine a uniform motion (that is, with $a=0$) in the direction of the readout gradient, G_x, the dashed line drawn in Fig. 10.52 represents the time dependence of the phase, $\varphi_v(t)$. This behavior describes a typical spin-echo sequence, such as shown in Fig. 10.40. At the time of appearance of the spin echo, T_e, the magnitude of φ_v is proportional to the velocity, v. For a material all parts of which move with the same velocity through the volume of measurement, this simply means that an additional phase factor occurs in the reconstructed image; the modulus image therefore remains unaffected by any motion. In general, however, other imaging conditions apply: the slice thickness is larger than the blood vessel diameter, and the velocity vector is parallel to the slice. The assumed laminar flow profile then gives different phase angles for the transverse magnetization at the time of the spin echo's occurrence. The MR signal for a pixel within the volume element arises through the superposition of all magnetization vectors. For a sufficiently large velocity, all phase angles between 0 and 2π would be present, and the resulting MR signal would then vanish due to destructive interference. The vessel, with blood flowing through it, is then seen with a lower intensity than the surrounding stationary tissue. These conditions can be described formally through the inclusion of an additional factor, $f(\Delta v)$, in Eq. (10.50):

$$S=\varrho f(\Delta v)\,e^{-T_e/T_2}(1-e^{-T_r/T_1}), \tag{10.59}$$

where $f(\Delta v)$ is a function of the velocity distribution within the volume element from which the pixel is taken. In a specific case, $f(\Delta v)$ must be determined from the particular velocity distribution and the sequence employed.

A simple method shows us how to keep the magnitude of the additional phase term, φ_v, in Eq. (10.58) small. In accordance with Fig. 10.53 two negative gradients, arranged symmetrically about the 180° pulse, are added on to the sequence [10.34]. Due to their symmetrical positioning, the time dependence of the phase, $\varphi_0(t)$, remains unchanged during the readout interval; this means that the MR signal for stationary spins also remains unchanged. The time dependence of the phase for uniformly moving spins is indicated in Fig. 10.52 by the unbroken line. It can be seen that, for suitable dimensioning of the gradient pulses (in terms of duration and amplitude), the phase, φ_v, passes through zero at the time of the spin echo's occurrence – independently of the velocity.

For the case of laminar flow, all magnetization vectors then point in the same direction. This implies constructive interference and the maximum value for the resulting MR signal. This so-called flow-rephasing, or bipolar, sequence (Fig. 10.53) consequently represents the vessel as a bright structure. The normal

spin-echo sequence, by contrast, is a flow-dephasing sequence, since the moving spins are not rephased at the time of occurrence of the spin echo. A simple method for the production of a pure vessel image can be derived from the fact that the MR signal remains unchanged for stationary spins: two MR images are acquired, the first by means of a flow-rephasing, bipolar sequence, and the second by means of a normal, flow-dephasing sequence. The remaining parameters of measurement, T_e and T_r, are unchanged. Following this, a subtraction is performed between the two MR images in order to eliminate all stationary image parts: the resulting image is then composed only of spins undergoing uniform motion.

The inclusion of further gradient pulses permits compensating for higher-order phase terms of the motion, such as acceleration. As a rule, though, the echo time must be lengthened in order to provide room to accommodate additional gradient pulses. The dimensioning of flow-rephasing, bipolar sequences takes

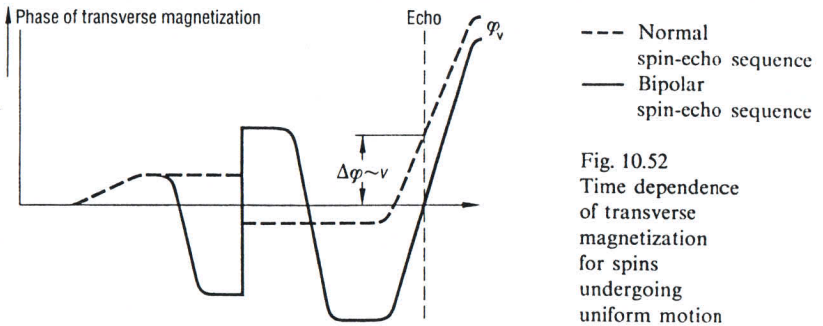

Fig. 10.52
Time dependence of transverse magnetization for spins undergoing uniform motion

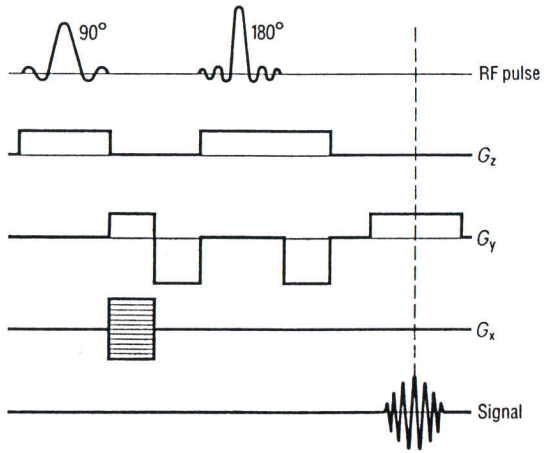

Fig. 10.53
Schematic representation of a bipolar spin-echo sequence

place as follows: beginning with a normal spin-echo sequence, the two additional gradient pulses are chosen to be of such duration and amplitude that the phase term, φ_v, present in Eq. (10.59) vanishes at the time of occurrence of the spin echo; that is,

$$\int_0^{T_e} G_x(t')\, t'\, \mathrm{d}t' = 0. \tag{10.60}$$

If one still wishes to compensate for acceleration effects, it is then necessary that the phase term φ_a vanish as well, so that

$$\int_0^{T_e} G_x(t')\, t'^2\, \mathrm{d}t' = 0. \tag{10.61}$$

For spin-echo sequences, the integration runs up to $T_e/2$ (the midpoint of the 180° pulse) with a positive integrand and, from this point to T_e (that is, from the midpoint of the 180° pulse to the echo), with a negative integrand, analogously to Eq. (10.10) in section 10.2.1.

Based on Eq. (10.60) and (10.61), it is possible to determine the gradient pulses needed for "motion refocussing". At the same time, these pulses must lie within the technical possibilities of the given gradient system (see section 10.2.2). In order to obtain short echo times in the range from 20 to 30 ms, it is necessary to choose short pulse lengths and correspondingly large amplitudes.

Clinical studies

In order to be able to follow vascular structures over a larger region, slice thicknesses between 30 and 60 mm are required. In general, this leads to low contrast between arteries and stationary tissue. In order to improve the recognizability of vascular structures, use of the subtraction procedure already mentioned – according to which a flow-rephased and a flow-dephased image are measured and the stationary part of the image subtracted out – is recommended. Nevertheless, the flow-rephasing technique only functions well under the assumption of uniform motion. Spins accelerated during the pulse sequence cannot be optimally rephased. It is known that this is the case for an arterial vascular system in which there is a large difference between the flow velocities between the diastole and the systole. The measurements are therefore ECG-triggered, so that the same velocity relationships apply for each Fourier projection. The position of the trigger in time is a further aid to controlling the contrast between vascular structures and stationary tissue. During the systole, the arterial velocities are so large that a dephasing results from acceleration, and the arteries then appear dark. In all, three measurements are performed (Figs. 10.54a to c):

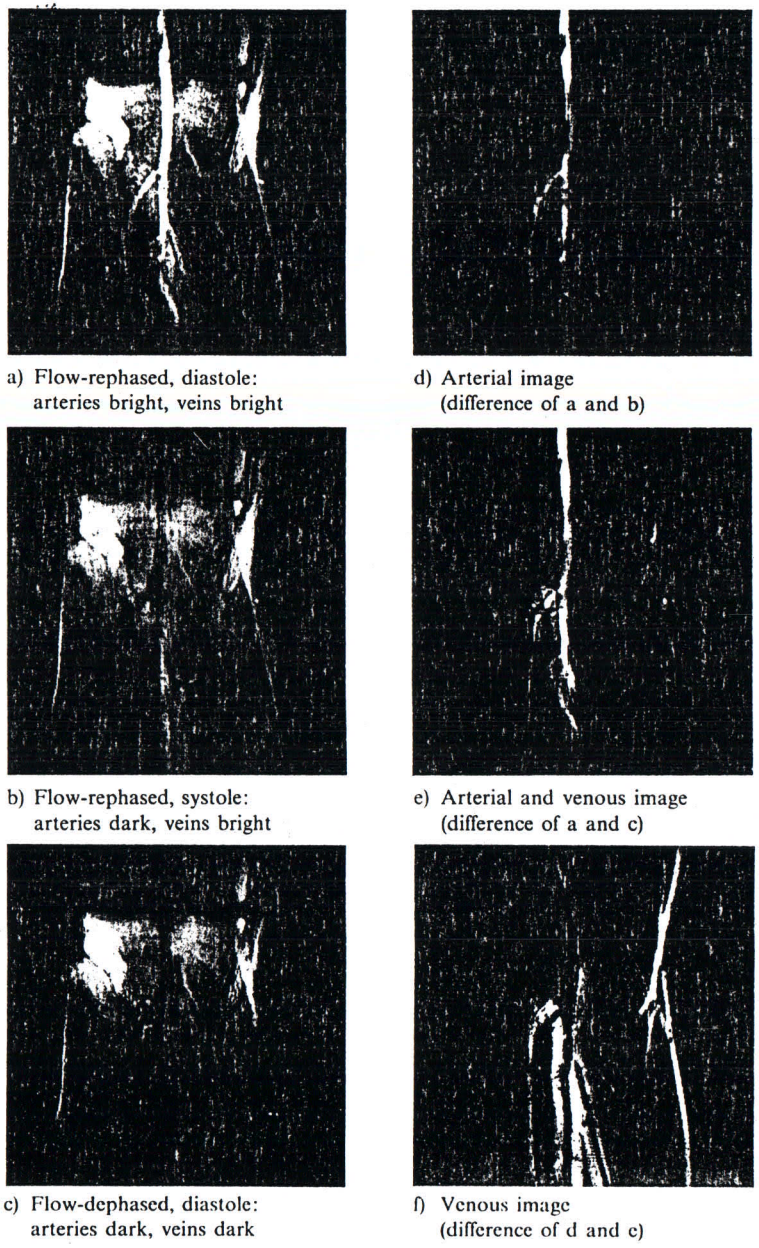

a) Flow-rephased, diastole: arteries bright, veins bright

b) Flow-rephased, systole: arteries dark, veins bright

c) Flow-dephased, diastole: arteries dark, veins dark

d) Arterial image (difference of a and b)

e) Arterial and venous image (difference of a and c)

f) Venous image (difference of d and e)

Fig. 10.54
ECG-triggered images (a to c) and subtraction images (d to f) of a part of the tibia for a healthy test subject: echo time 56 ms, slice thickness 34 mm, pixel size 0.8 mm, time measured approx. 4 min per image

a) flow-rephased, diastole (arteries: bright, veins: bright)
b) flow-rephased, systole (arteries: dark, veins: bright)
c) flow-dephased, diastole (arteries: dark, veins: dark)

The intensity of stationary tissue is the same for all three sequences. Figures 10.54a to c show for example these three images for a part of the tibia below the knee of a healthy test subject. The echo time was 56 ms, the slice thickness 34 mm and the pixel size 0.8 mm. The time of measurement for each image was 256 heart beats; that is, about four minutes. From these images, subtraction images were produced (Figures 10.54d to f), namely

d) the difference between a) and b): arterial image
e) the difference between a) and c): arterial and venous image
f) the difference between d) and e): venous image.

The individual images reproduce the anatomical details very faithfully. In particular, the bifurcation of the arteria poplitea into three tibial trunk arteries can be seen clearly.

The method of MR vascular presentation introduced here demonstrates that, in the field of angiography, MRI is capable of producing images very bit as good as those taken from conventional x-ray angiography or digital subtraction angiography (DSA).